Power Amplification for Piezoelectric Actuators in Controlled Structures

by

David J. Warkentin

S. B. Massachusetts Institute of Technology (1987)

S. M. Massachusetts Institute of Technology (1991)

Submitted to the Department of Aeronautics and Astronautics in Partial Fulfillment of the Requirements for the Degree of

Doctor of Philosophy

at the

Massachusetts Institute of Technology

June 1995

Signature of Author_____

Department of Aeronautics and Astronautics

May 31, 1995

Certified by_____

Professor Edward F. Crawley

Thesis Committee Chairman, Department of Aeronautics and Astronautics

Certified by_____

Professor John J. Deyst, Department of Aeronautics and Astronautics

Certified by_____

Professor Nesbitt W. Hagood, Department of Aeronautics and Astronautics

Certified by_____

Professor Hugh L. McManus, Department of Aeronautics and Astronautics

Accepted by_____

Professor Harold Y. Wachman

Chairman, Department of Aeronautics and Astronautics

Graduate Committee

Power Amplification for Piezoelectric Actuators in Controlled Structures

by

David J. Warkentin

Submitted to the Department of Aeronautics and Astronautics on May 31, 1995 in Partial Fulfillment of the Requirements for the Degree of Doctor of Philosophy

Abstract

This work addresses power issues in the application of piezoelectric actuators and embedded electronic components of interest in the development of a fully integrated intelligent structures technology. The power flow characteristics of piezoelectric actuators are examined in closed-loop control applications. An analysis is presented of the power flow and voltage and current requirements of a piezoelectric actuator in a simple system, along with implications for the design of linear amplifiers. The contributions of various elements to average and peak power flow levels are identified, as is the effect of loop closure on the impedance which the actuator presents to the amplifier. A package integrating four piezoelectric ceramic actuators with a monolithic high-voltage operational amplifier in an assembly with a total thickness of less than one millimeter is described. Two of these packages are used to actuate a cantilever beam with an external disturbance source. The voltage and current responses of the actuators to the disturbance are measured in the closed loop system, demonstrating the validity of the load impedance effects predicted by the model. The previously unaddressed effects of a nonlinearity in the current response of the piezoelectric ceramics are discussed. The component temperature elevation resulting from the computed dissipation is modeled with thermal finite element analysis. A series of hardware simulators is used to investigate the roles played by various heat loss mechanisms and to develop an appropriate thermal management configuration. Finally, results of optimal control theory are used to derive a possible pattern for a heat spreader which would yield adequate thermal performance at a minimal cost in mass and stiffness.

Thesis Committee: Professor Edward F. Crawley, Chairman
Professor John J. Deyst
Professor Nesbitt W. Hagood
Professor Hugh L. McManus

Acknowledgments

The author would like to express his deep appreciation for the guidance and advice of the members of his thesis committee, and particularly for the patience of Professor Edward Crawley, without whose unflagging support and encouragement the completion of this work would have been impossible. Thanks are also due to my fellow graduate students in SERC, both to previous students for their assistance and inspirational examples, and to current students for their friendship and tolerance of idiosyncratic behavior during difficult periods. I am grateful as ever to my family for their steadfast confidence, and to the technical and administrative staff of the Department of Aeronautics and Astronautics for their invaluable assistance in guiding me over the hurdles and around the obstacles on my way to the completion of my academic journey at MIT.

This work was supported by NASA Grant NAGW-2014.

Table of Contents

Table of Figures

CHAPTER 1: INTRODUCTION

1.1 Motivation

Intelligent structures are those which incorporate actuators and sensors that are highly integrated into the structures and have structural functionality, as well as highly integrated control logic, signal conditioning, and power amplification electronics [Crawley, Bent, Warkentin, and Hagood, 1994]. Such actuating, sensing, and signal processing elements are incorporated into a structure for the purpose of influencing its states or characteristics, be they mechanical, thermal, optical, chemical, electrical, or magnetic. For example, a mechanically intelligent structure is capable of altering both its mechanical states (its position or velocity) or its mechanical characteristics (its stiffness or damping). In one proposed application of this technology, the extreme weight and volume restrictions of numerous small spacecraft would be met by combining sensors, electronics, and structural materials into what the authors call multifunctional materials for the purposes of performance enhancement and health monitoring [Obal and Sater, 1994].

The eventual goal of this particular research effort at the MIT Space Engineering Research Center was the construction of an intelligent structure which has fully integrated sensors, actuators, and processing electronics. Such structures may benefit from simplified component interconnections and natural implementations of hierarchic control architectures, as suggested in [Warkentin and Crawley, 1991.] In pursuit of this eventual goal, research at SERC has focused on the issues raised in implementing embedded electronics. Previous work has demonstrated the feasibility of physically embedding integrated circuit components within

graphite/epoxy composite structures [Warkentin, Crawley, and Sodini, 1992.] For aerospace applications, particularly those involving spacecraft, the management of the power and thermal loads associated with the driving electronics may be important [Henderson and Stover, 1991; Wertz and Larson, 1991].

1.2 Background

In the following pages, a brief sketch will be presented of some of the research developments from various which have contributed to and motivated the present work. A few of the many contributions to piezoelectric actuator development are mentioned, along with some large-scale aerospace applications. Pertinent advances in electronics technology over the last decade are described, along with some notes on the nature of power amplifiers, both proposed and in practice. Finally, recent work in the modeling of power transfer and dissipation is examined.

1.2.1 Piezoelectric actuators and applications

Piezoelectric materials, characterized by their ability to deform under the application of an electric field, have in recent years been widely studied in the laboratory for application in the field of structural control [Bailey and Hubbard, 1985; Crawley and de Luis, 1987; Fanson and Chen, 1986; Lee, O'Sullivan, and Chiang, 1989; Hanagud, Obal, and Calise, 1987; Spangler, 1994]. In works such as the last two cited, the direct effect (the production of charge in response to mechanical deformation) is used as well as the indirect or actuation effect.

Applications of piezoelectric actuators to real-world problems have included both space and aeronautical examples. In work reported by [Bronowicki, Innis, Betros, and Kuritz, 1993] and [Schubert, 1993], the early achievements of [Crawley and de Luis, 1987] in embedding piezoelectric actuator components in graphite/epoxy structural members have been further developed in the construction of ground and flight test hardware for proposed space structures requiring structural control. These studies have demonstrated performance benefits in reduced disturbance levels and

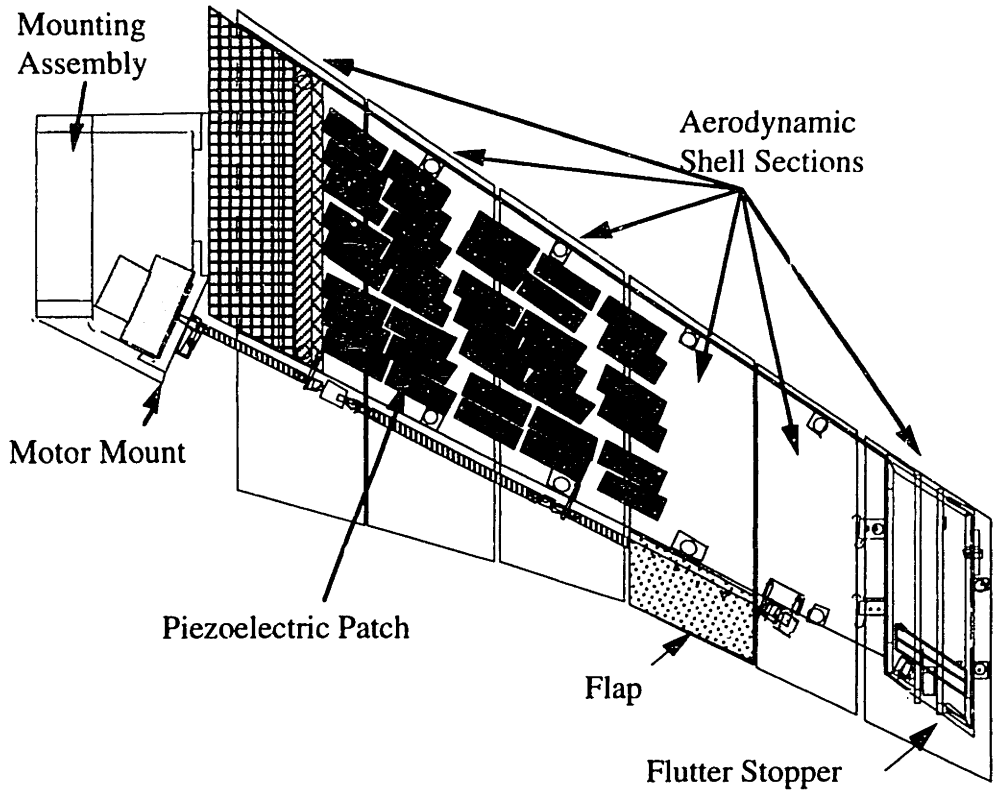

Fig. 1.1. Plan view of four foot wing model used in aeroservoelastic wind tunnel experiments. 36 actuator packages on top surface are shown. (Figure courtesy G. Reich and C. Lin.)

faster settling times through the use of active damping.

Among the possible aeronautical applications cited by [Agnes, Whitehouse, and Mackaman. 1993] are vibration control for airborne optics, the alleviation of sonic or buffet fatigue, and active aeroelastic control. In [Ehlers and Weisshaar, 1990] and [Paige, Scott, and Weisshaar, 1993], the use of piezoelectric actuators for static wing deformation and panel flutter control is analyzed. A more advanced state of the technology is demonstrated in [Lin, Crawley, and Heeg, 1995], in which a four foot scale model of a piezoelectrically actuated active wing was tested in open and closed loop configurations in a transonic wind tunnel, demonstrating both gust alleviation and flight envelope expansion by flutter suppression. Figure 1.1 shows a schematic of the test article used.

1.2.2 Electronics

Further progress towards the ultimate development of truly integrated

intelligent structures depends on the development of appropriate electronic components. Of particular interest here are technological developments which allow the combination of many functions on the fewest discrete silicon chips. Work such as that described in [Ohno, Inabe, and Koinuma, 1984; Meyer, Dick, Olson, Lee, and Shimer, 1987; and Beasom, 1987] has demonstrated the use of such techniques as junction and dielectric isolation to allow the integration of both low and high voltage devices on a single chip. This has opened the way for the development of electronic components known generically as "smart power ICs." Such components, which marry low-voltage analog and digital control and processing with high-voltage (as high as 450 V) high-power output functions, have been used for solenoid control, flat panel displays, telecommunication switches, and automotive applications [Sugawara and Shimura, 1987; Wong, Kim, Young, and Mukherjee, 1991]. In an overview of the state of the field, [Baliga, 1991] makes comparison of the combination of signal processing and output functions in smart power ICs with the integration of control and actuation in the human body, much like the biological analogy drawn by the developers of intelligent structures.

In addition to the development of smart power ICs, other electronic advances conducive to the development of intelligent structures have been made. Progress made in integrated sensing technology is represented by the work of [Barth *et al*, 1988], in which one of many monolithic silicon accelerometers is described. These devices integrate sensing elements with signal conditioning and processing functions on a single chip. Reduction in part count through integration is further enhanced by the developments of single-chip microcomputers of the type described in [Lister, 1984]. These increasingly capable products integrate not only the conventional functions of processing, digital input/output, and memory, but also control functions such as analog to digital and digital to analog signal conversion. Given the above mentioned developments in smart power ICs, the possibility of a completely integrated electronic component combining signal conditioning, processing, and power output functions appears within reach of present technology; the ability to build systems for various commercial applications from modular components, however, may diminish the attractiveness of such a product to large manufacturers. The growth of options in the form of custom or semi-custom design of integrated circuits [Hurst, 1985] may

eventually circumvent this difficulty.

For the present work, it was deemed sufficient to examine the implications of integrating the power amplifier and actuator elements alone, leaving sensor signal conditioning and processing to future efforts. The particular amplifier device used in this work, the PA-41 high-voltage operational amplifier (manufactured by Apex Microtechnology Corp., Tucson, Arizona), was chosen for its large voltage range and the fact that is now commercially available in monolithic die form. As a linear amplifier with a push-pull output stage, it shares important circuit topology characteristics common to many conventional amplifiers, ranging from those designed to drive comparatively small capacitive loads to small voltages at high frequencies [Wong and Salama, 1986; Brehmer and Wieser, 1983; and Naumann and Schmidt, 1989] to those designed for large capacitive, high-voltage (hundreds to thousands of volts) applications [Theofanous, Tsitomeneas, Alexakis, and Arapoyianni, 1987; Krasnov and Fomin, 1988; and Reynolds, 1992]. It will be shown in the subsequent chapters that the output stage topology of amplifiers of this class has important implications for the amount of power dissipated in the amplifier.

Another possible amplifier technology for driving piezoelectric loads is that of switching amplifiers. The use of semiconductor switch technology has certain advantages over linear systems because of the potential to achieve extremely high efficiency; i.e., low power losses in the amplifiers [Ohno, 1988; Kassakian, Schlecht, and Verghese, 1991]. Such amplifiers have been applied to piezoelectric transducers in the field of sonar [Dixon and Leyland, 1990] and structural control [Chiarappa and Claysmith, 1981] with the explicit objective of minimizing power loss within the amplifier. In the first application, however, the desired wave forms are limited to a narrow band of sinusoidal pulses, and the desired efficiency is obtained by inductive tuning elements in series with the transducer. The structural control application cited was a quasi-static problem of mirror deformation, in which the question of dynamic structural control was not addressed. The use of switching technology for distributing power and amplifying voltages in a dynamic structural control problem could result in benefits from decentralization and improved reliability and thermal management [Lindner, Kirby, and Sable, 1994], but to date the application to integrated

intelligent structures appears to be limited by the need for space-consuming inductive elements.

1.2.3 Power transfer and dissipation

In attempting to distribute the signal and power amplifying functions along with the actuators, it becomes necessary to address the issue of amplifier power dissipation, both in terms of the source and magnitude of the power and in terms of the appropriate means of waste heat disposal. The modeling of such piezoelectric actuators for dynamic control of structures is well established; [Hagood, Chung, and von Flotow, 1990] present a general formulation of the use of a variational principle to derive equations of motion relating actuator voltages and charges to structural displacements and disturbance forces. The results were applied to the problem of shunting actuators with passive electrical networks in [Hagood and von Flotow, 1991]. As power duals, the voltage and current determine the flow of power between the electronic control system and the actuator/structure combination. An interesting result from sonar array studies is noted in [Richards, Blottman, and McTaggart, 1990], in which the power emitted by one transducer element may be absorbed by a neighboring element, presenting the driving amplifier with a load which is effectively a negative resistance. [Liang, Sun, and Rogers, 1993] use impedance modeling to compute various components of both the electrical and mechanical power flow and dissipation for a structure actuated in an open loop condition; the derivation of the various impedances, however, is not always straightforward, and the question of power dissipation within the amplifier itself is neglected. Further work along this lines includes that of [Niezrecki and Cudney, 1994], in which a series inductive element is used (as in sonar applications such as [Dixon and Leyland, 1990]) to present the driving amplifier with a more manageable load than that of the actuator alone. The fixed inductor, however, can only provide a beneficial effect over a narrow frequency range, severely limiting the use of the actuator is general closed loop control schemes.

1.3 Thesis objectives and approach

The objective of this thesis is to examine piezoelectric actuators in intelligent structures from the perspective of power flow, to determine the characteristics governing power dissipation in amplifiers used to drive them in closed loop systems, and to study the problem of the management of waste heat in order to maintain component temperatures within required limits.

The approach adopted was a combination of theoretical, numerical, and experimental efforts. The electromechanical modeling techniques of [Hagood, Chung, and von Flotow, 1990] were applied to a simple controlled structure with the aim of illuminating basic physical relations and developing intuitive explanations for behavior in more complex systems. This was extended numerically to a more realistic system, which was then implemented in hardware. In the course of this implementation, a low-profile actuator package was developed which integrates the electronic components for power amplification with the piezoceramic actuator elements themselves. Experimental measurements of closed loop voltage and current responses were then made to verify the numerical model and the analytical interpretation of the power flow. Thermal experiments, guided by finite element analyses, were used to design package elements to maintain the amplifier temperature below its operational maximum.

1.4 Outline

In Chapter 2, power issues are examined by applying the modeling techniques of [Hagood, Chung, and von Flotow, 1990] to a simple dynamic system: a cantilever beam modeled with a single mode. Although the flow of mechanical energy between actuator and structure is not explicit as in [Liang, Sun, and Rogers, 1993], the use of energy principles allows the derivation of electromechanical models based on Rayleigh-Ritz or finite element methods, which are readily extended to problems of complex geometry and large numbers of modes, sensors, and actuators. The simplicity of the single-mode Rayleigh-Ritz model presented here allows the derivation of interesting relations and parameter groupings which ma

shed further light on power flow and dissipation in piezoelectrically actuated structures. Furthermore, the behavior of a single mode often dominates in systems in which disturbance rejection is the performance objective [Campbell and Crawley, 1994].

The single-mode cantilever beam model is derived along with various nondimensionalizations. Rate feedback is assumed, and the voltage and current responses to an external disturbance are then examined, illustrating the impedance which the actuator appears to present to the driving amplifier. A simplified model of a typical linear amplifier output stage is used to compute the power dissipation in the amplifier for various levels of piezoelectric effectiveness and active damping. Amplifier power dissipation results are presented for both sinusoidal and random excitations, and are compared with the amplifier dissipation that would result from the same control voltage applied to a capacitor of equivalent size.

In Chapter 3, a description is presented of the construction a simple controlled structure to verify and explore the limitations of power modeling concepts developed in Chapter 2. This chapter details the development and implementation of an actuator package in which piezoelectric ceramics are integrated along with the electronic components which power them. The packaging design must satisfy requirements for mechanical, electrical, and chemical isolation of the integrated circuit and at the same time provide for the disposal of the heat dissipated in the electrical components, so that their temperatures do not exceed operational limits. The feasibility of fabricating such packages is established, although manufacturing difficulties prevented the construction of fully functioning packages for the present work. For the purposes of model verification and power measurement, a cantilever beam experiment was designed using two of the actuator packages with external electronic components. The electro-mechanical modeling approach of [Hagood, Chung, and von Flotow, 1990] is again applied, this time to a nonuniform, multi-mode beam. The experimental open loop response is compared to that of the model, noting limitations imposed by nonlinearities. Under external disturbance with approximate rate feedback, the negative resistive apparent load impedance derived in Chapter 2 is observed. Finally, measurements of power flow and

amplifier dissipation are presented, illustrating the importance of amplifier nonidealities and piezoelectric nonlinearities.

In Chapter 4, the mechanisms for heat transfer in the actuator package described in Chapter 3 are investigated, with an emphasis on design elements which maintain low chip temperature. Given the previous description of the sources and magnitude of the amplifier power dissipation to be expected, it must be shown how this waste heat may be disposed of without violating operational temperature limits. Hardware simulators and finite element models were constructed to evaluate the importance of conduction within the package and ambient loss mechanisms in determining heat flow and temperature patterns. The use of a heat spreader in thermal management is considered, and an analytical basis is established for the optimum design of such elements.

Taken as a whole, the work presented here in the areas of power flow and dissipation modeling, embeddable actuator package design and fabrication techniques, and thermal management of waste heat represents an attempt to materially advance and facilitate the development of a new structures technology. The results achieved may help to shed light on some of the fundamental power issues which will be encountered in the development of true intelligent structures.

CHAPTER 2: MODELING OF POWER FLOW AND DISSIPATION

The objective of this chapter is to examine power issues by applying the modeling techniques of [Hagood, Chung, and von Flotow, 1990] to a simple dynamic system: a cantilever beam modeled with a single mode. Although the flow of mechanical energy between actuator and structure is not explicit as in [Liang, Sun, and Rogers, 1993], the use of energy principles allows the derivation of electromechanical models based on Rayleigh-Ritz or finite element methods, which are readily extended to problems of complex geometry and large numbers of modes, sensors, and actuators. The simplicity of the single-mode Rayleigh-Ritz model presented here allows the derivation of interesting relations and parameter groupings which may shed further light on power flow and dissipation in piezoelectrically actuated structures. Furthermore, the behavior of a single mode often dominates in systems in which disturbance rejection is the performance objective [Campbell and Crawley, 1994].

In the following section, the single-mode cantilever beam model is derived along with various nondimensionalizations. Rate feedback is assumed, and the voltage and current responses to an external disturbance are then examined, illustrating the impedance which the actuator appears to present to the driving amplifier. A simplified model of a typical linear amplifier output stage is used to compute the power dissipation in the amplifier for various levels of piezoelectric effectiveness and active damping. Amplifier power dissipation results are presented for both sinusoidal and random excitations, and are compared with the amplifier dissipation that would result from the same control voltage applied to a capacitor of equivalent size.

2.1 1-DOF Modeling and Nondimensionalization

The voltage and current relations will now be derived for a single mode system in which rate feedback is used to increase damping.

2.1.1 Electromechanical model

The cantilever beam configuration chosen for purposes of illustration is shown in Figure 2.1; piezoelectric actuator elements (subscript a) are bonded to the top and bottom faces of a substructure (subscript s). The piezoelectric poling directions and electrode connections are such that an applied voltage V_a produces equal and opposite induced strains in the two actuator layers, yielding a bending effect. For a single degree of freedom illustration, the displacement at the beam tip q may be used to characterize the modal displacement, and a tip force F_d is assumed to provide an external disturbance source.

The constitutive relations for a piezoelectric material may be written [IEEE, 1978] as

$$\begin{aligned} S &= s^E T + dE \\ D &= d_t T + \varepsilon^T E \end{aligned} \tag{2.1}$$

where S, T, D, and E are the strain, stress, electric displacement, and electric field tensors, and s^E, ε^T, and d, are the short-circuit compliance, the free dielectric constant, and the piezoelectric constant, respectively. The subscript t denotes a transpose. A procedure such as that presented in [Hagood, Chung, von Flotow 1990] may be followed; assuming field shape functions and applying a coupled electromechanical variational principle [Crandall, *et al*, 1968], equations of motion may be derived by means of a finite element, Rayleigh-Ritz, or other assumed shape method. For problems such as the present one in which the independent inputs to the system are force and voltage, it is more convenient to write the constitutive relations as

$$\begin{aligned} c^E S &= T + c^E dE \\ D &= d_t c^E S + \varepsilon^S E \end{aligned} \tag{2.2}$$

where the transformed set of material properties now includes the short-circuit stiffness c^E and the clamped dielectric constant ε^S. In this work, it is assumed that material constants are real and linear, and that the electric

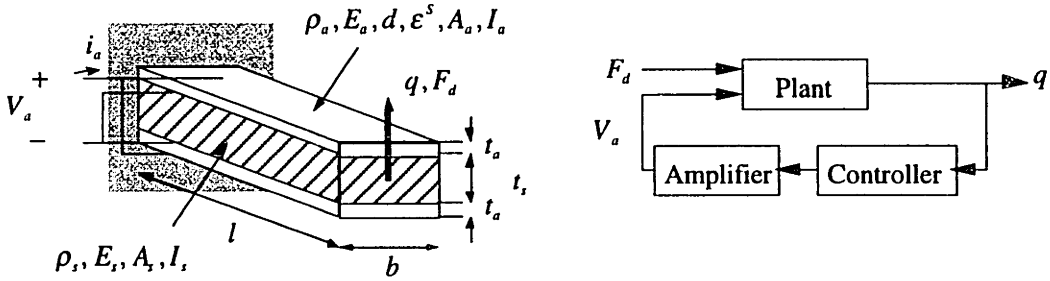

Fig. 2.1. Configuration of single degree of freedom controlled cantilever beam.

field is uniform through the actuator elements.

It can be shown that under Bernoulli-Euler beam assumptions a constant applied voltage will produce a constant curvature and hence a quadratic deflection of the beam [Crawley and Anderson, 1990]. The resulting parabolic shape may be used as an approximation to the exact shape of the first mode of a cantilever beam, with the tip deflection as the modal displacement. Evaluating the appropriate Raleigh integrals for modal mass, stiffness, and forcing yields the following governing equations:

$$\frac{1}{5}(\rho_s A_s + \rho_a A_a) l \frac{d^2 q}{dt^2} + (E_s I_s + E_a I_a)\frac{4}{l^3} q = \frac{2}{l} b d E_a (t_s + t_a) V_a + F_d \tag{2.3}$$

$$Q_a = \frac{2}{l} b d E_a (t_s + t_a) q + 2\varepsilon^S \frac{bl}{t_a} V_a \tag{2.4}$$

Eq. 2.3 expresses the modal behavior of the system with the forcing due to applied voltage and tip disturbance. Eq. 2.4 expresses the total charge Q_a developed on the two piezoelectric elements as the sum of two components: the first due to mechanical displacement q and the second due to the applied voltage V_a. Note that the second component has the form of flat plate capacitors connected in parallel; this reflects the inherent capacitance of the actuators under clamped conditions ($q = 0$).

In order to highlight the most important relations and make the results appear less problem-specific, it is useful to make some further simplifying assumptions, introduce normalizations, and recognize common parameter groupings. The exact steps taken in this case are specific to the cantilever beam problem; analyses of other configurations would lead to analogous results. If the piezoelectric layers are thin compared to the structure, the following approximations result:

$$t_a << t_s \quad I_a \cong \frac{bt_a t_s^2}{2} \quad t_s + t_a \cong t_s \tag{2.5}$$

Length, mass, and time may be normalized by the beam length, the modal mass, and the inverse of the modal frequency, respectively:

$$L = l \quad M = \frac{1}{5}(\rho_s A_s + \rho_a A_a) l \quad T = \frac{1}{\omega_1} = \frac{1}{\sqrt{\frac{20(E_s I_s + E_a I_a)}{l^4(\rho_s A_s + \rho_a A_a)}}} \tag{2.6}$$

Modal displacement, time, and temporal derivatives are related to their nondimensional counterparts by

$$q = l\tilde{q} \quad t = \frac{\tilde{t}}{\omega_1} \quad \frac{d(.)}{dt} = \omega_1 \frac{d(.)}{d\tilde{t}} \tag{2.7}$$

From the nondimensionalizations of Eq. 2.6 the consistent grouping for nondimensionalizing force may be found:

$$F_d = \left(\frac{ML}{T^2}\right)\tilde{F}_d \tag{2.8}$$

The remaining fundamental quantity to be normalized is charge, but the physical limitation on voltage set by the value of the coercive electric field strength makes a normalization of voltage seem more useful:

$$V_a = (E_c t_a)\tilde{V}_a \tag{2.9}$$

Since a consistent set of units equates a unit of charge to a unit of energy divided by a unit of electric potential, the consistent normalization for charge is

$$Q_a = \frac{\left(\frac{ML^2}{T^2}\right)}{(E_c t_a)}\tilde{Q}_a \tag{2.10}$$

Substituting the approximations of Eq. 2.5 and the normalizations of Eq. 2.6-2.10 into Eq. 2.3, 2.4 yields

$$\frac{d^2\tilde{q}}{d\tilde{t}^2} + \tilde{q} = 4\left(\frac{T^2}{ML}\right)E_a I_a \frac{dE_c}{lt_s}\tilde{V}_a + \tilde{F}_d \tag{2.11}$$

$$\tilde{Q}_a = 4\left(\frac{T^2}{ML}\right)E_a I_a \frac{dE_c}{lt_s}\tilde{q} + 4\left(\frac{T^2}{ML^2}\right)I_a \varepsilon^S \frac{l}{t_s^2} E_c^2 \tilde{V}_a \tag{2.12}$$

At this point it is convenient to note that

$$\frac{ML}{T^2} = \frac{4(E_s I_s + E_a I_a)}{l^2} \tag{2.13}$$

so that Eq. 2.11, 2.12 may be written

Table 2.1. Nondimensionalizations for single degree of freedom system

	Quantity	Specific value	Nondim.
Fundamental	length, $L = l$	l	$q = l\tilde{q}$
	mass, $M = M_1$	$\frac{1}{5}(\rho_s A_s + \rho_a A_a)l$	$M = M_1\tilde{m}$
	time, $T = \frac{1}{\omega_1}$	$\frac{1}{\sqrt{\frac{20(E_s I_s + E_a I_a)}{l^4(\rho_s A_s + \rho_a A_a)}}}$	$t = \frac{\tilde{t}}{\omega_1}$
	voltage, $V = V_c$	$E_c t_a$	$V_a = V_c \tilde{V}_a$
Derived	force, $F = \left(\frac{ML}{T^2}\right)$	$\frac{4(E_s I_s + E_a I_a)}{l^2}$	$F_d = F\tilde{F}_d$
	charge, $Q = \frac{\left(\frac{ML^2}{T^2}\right)}{V}$	$\frac{4(E_s I_s + E_a I_a)}{E_c t_a l}$	$Q_a = Q\tilde{Q}_a$
	frequency, $\Omega = \frac{1}{T}$	$\sqrt{\frac{20(E_s I_s + E_a I_a)}{l^4(\rho_s A_s + \rho_a A_a)}}$	$\omega = \Omega\tilde{\omega}$ $p = \Omega s$

$$\frac{d^2\tilde{q}}{d\tilde{t}^2} + \tilde{q} = \left(\frac{E_a I_a}{E_s I_s + E_a I_a}\right)\left(\frac{l}{t_s}\right)(dE_c)\tilde{V}_a + \tilde{F}_d \tag{2.14}$$

$$\tilde{Q}_a = \left(\frac{E_a I_a}{E_s I_s + E_a I_a}\right)\left(\frac{l}{t_s}\right)(dE_c)\tilde{q} + \left(\frac{E_a I_a}{E_s I_s + E_a I_a}\right)\left(\frac{\varepsilon^S}{d^2 E_a}\right)\left(\frac{l}{t_s}\right)^2 (dE_c)^2 \tilde{V}_a \tag{2.15}$$

The nondimensionalizations used are summarized in Table 2.1; nondimensionalized variables are denoted by (~).

Note that the appearance of I_a in the numerators of the right-hand sides of Eq. 2.14, 2.15 is a consequence of the assumption in Eq. 2.5 that the piezoelectric layers are thin: if this were not the case, a geometric correction factor would be required to account for the difference between the uniformity of the electric field in the actuator and the Bernoulli-Euler assumption of linear variation of strain with distance from beam mid-line.

The significance of introducing certain groupings is now apparent. One can identify the bending stiffness ratio, an electromechanical coupling factor of the piezoelectric, an electromechanical coupling factor of the structure as a whole, and the maximum achievable free piezoelectric strain:

$$\psi = \frac{E_s I_s}{E_a I_a} \quad K^2 = \frac{E_a d^2}{\varepsilon^S} \quad \tilde{K}^2 = \frac{K^2}{\psi + 1} \quad \Lambda_c = dE_c \tag{2.16}$$

In [Crawley and de Luis, 1987], a somewhat different expression

$$\psi = \frac{E_s t_s}{E_a t_a} \tag{2.17}$$

was used in the formulation for a structure with rectangular cross-section and actuator layers used for extension or bending, but an additional parameter α was introduced to distinguish between the two cases. The present definition more clearly reflects the true significance of the term, which may be generally interpreted as the ratio of modal strain energy in the actuator to that in the structure. The electromechanical coupling coefficient K^2 used here is simply related to the more commonly used coefficient k^2:

$$K^2 = \frac{k^2}{1-k^2} \quad k^2 = \frac{E_a d^2}{\varepsilon^T} \tag{2.18}$$

In the converse piezoelectric effect, k^2 is the fraction of energy input through the leads of the piezoelectric which is mechanically deliverable; its complement, $1-k^2$, is the fraction stored as electrical energy. K^2 is the ratio of the former to the latter; a larger value means more of the energy input through the leads is mechanically deliverable and less is stored as essentially useless electrical energy. This form of coupling coefficient is convenient in expressing the impedance of a thin plate vibrating in a radial mode [IEEE, 1978]. The de-rated value $\tilde{K}^2$ has been previously identified [Hagood and von Flotow, 1992] as a useful variation which reflects the participation of the actuator in the strain energy of the entire system. For a typical piezoceramic (G-1195 or PZT5-A), k^2 can range from 0.118 to 0.497 (K^2 from 0.134 to .988) [Vernitron, undated].

The resulting equations are now

$$\frac{d^2\tilde{q}}{d\tilde{t}^2} + 2\zeta_a \frac{d\tilde{q}}{d\tilde{t}} + \tilde{q} = \tilde{e}\tilde{V}_a + \tilde{F}_d \tag{2.19}$$

$$\tilde{Q}_a = \tilde{e}\tilde{q} + \frac{\tilde{e}^2}{\tilde{K}^2}\tilde{V}_a \tag{2.20}$$

where an intrinsic structural damping ratio ζ_a has been assumed, and the direct and converse piezoelectric effect are now reflected in one grouping:

$$\tilde{e} = \frac{\Lambda_c}{\tilde{t}_s(\psi+1)} \tag{2.21}$$

This effective piezoelectric constant reflects the combined influence of the inherent piezoelectric nature of the actuator and the actuator saturation limit (through d and E_c in Λ_c), the ratio of modal strain energy in actuator

and substructure (through ψ), and a geometric shape factor (through $\tilde{I}_1$). The actual values for these parameters will, of course, depend upon the specific problem; for the purposes of producing illustrative plots below, it is assumed that $\psi = 9$ and that Λ_c and $\tilde{I}_1$ are such that $\tilde{e} = 1$. In addition, it is assumed in the plots that all the damping is due to the active control, that is, $\zeta_m = 0$.

Before proceeding with the examination of behavior of the closed-loop system, it should be noted again that equations of the form of Eq. 2.21 can be derived for arbitrary systems using energy principles via (e.g.) finite element methods. In the following sections, the analytical simplicity of the present system allows the identification of significant parameter groupings which would be obscured for more complex systems, but even in such cases the responses of the system to sinusoidal or random excitation could be computed to yield information about the power flow and dissipation.

2.1.2 Amplifier model

If a conventional linear amplifier with a two transistor, push-pull output stage is assumed as in Figure 2.2, and base-emitter voltage drops, base currents, and dissipation in earlier stages are all neglected, the power dissipated in each transistor can be written as approximately the product of the collector-emitter voltage and the output current:

$$\tilde{P}_{Q_1}(t) = \begin{cases} (\tilde{V}_S - \tilde{V}(t))\tilde{i}_a(t), & \tilde{i}_a(t) > 0 \\ 0, & \tilde{i}_a(t) < 0 \end{cases}$$
$$\tilde{P}_{Q_2}(t) = \begin{cases} 0, & \tilde{i}_a(t) > 0 \\ (-\tilde{V}_S - \tilde{V}(t))\tilde{i}_a(t), & \tilde{i}_a(t) < 0 \end{cases} \qquad (2.22)$$

The dependence on the sign of the load current is due to the fact that Q1 can only source current to the load, and Q2 can only sink current. This is typical of efficient output stages, though the exact implementation may use field effect rather than bipolar transistors, and ladders rather than single devices [Naumann and Schmidt, 1989, Krasnov and Fomin, 1988, Reynolds, 1992, and Brehmer and Wieser, 1983].

Note that the rail voltages have been nondimensionalized, and that these expressions hold only as long as the amplifiers are not saturated. Combining the expressions in Eq. 2.22, the total power dissipated in the amplifier is given by

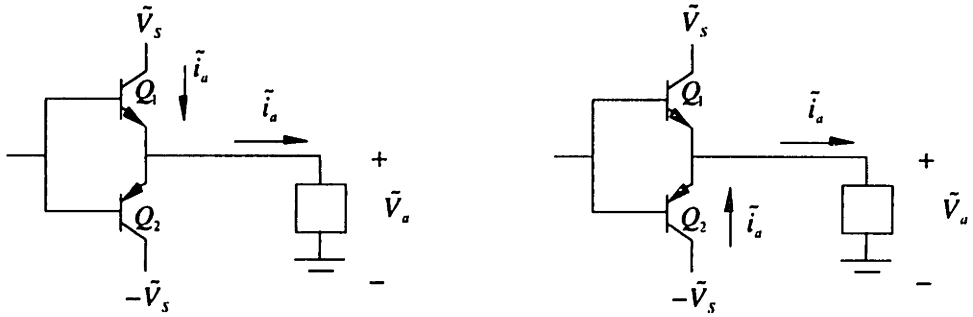

Fig. 2.2. Typical amplifier push-pull output stage. Q1 is on and Q2 is off when load current is positive (left); Q2 is on and Q1 is off when load current is negative (right).

$$\tilde{P}_{amp}(t) = -\tilde{i}_a(t)\tilde{V}_a(t) + \left|\tilde{i}_a(t)\right|\tilde{V}_S \tag{2.23}$$

in which the first term is the power flow to the actuator, and the second is the power drawn from the rails. It is now possible to use the electromechanical and amplifier models to derive useful analytical expressions for the current, voltage, and power responses of the system to an external disturbance.

2.2 Closed Loop Behavior

Reducing the response to disturbances by actively increasing damping through feedback is a common control objective; if the applied actuator voltage is made proportional to the modal displacement rate, the intrinsic damping ratio ζ_o can be augmented:

$$\tilde{V}_a = -\frac{2\zeta_a}{\tilde{e}}\dot{\tilde{q}} \quad \ddot{\tilde{q}} + 2\zeta\dot{\tilde{q}} + \tilde{q} = \tilde{F}_d \quad \zeta = \zeta_o + \zeta_a \tag{2.24}$$

where ζ_a is the desired additional damping to be achieved. Alternately, if position is fed back, Eq. 2.24 becomes

$$\tilde{V}_a = -\frac{\kappa}{\tilde{e}}\tilde{q} \quad \ddot{\tilde{q}} + 2\zeta_o\dot{\tilde{q}} + (1+\kappa)\tilde{q} = \tilde{F}_d \tag{2.25}$$

and acceleration feedback yields

$$\tilde{V}_a = -\frac{\mu}{\tilde{e}}\ddot{\tilde{q}} \quad (1+\mu)\ddot{\tilde{q}} + 2\zeta_o\dot{\tilde{q}} + \tilde{q} = \tilde{F}_d \tag{2.26}$$

It is the rate feedback, though, which is of principle interest in this work.

Certain relations of potential interest may now be investigated. The

results for sinusoidal force excitation will be presented first, in the form of the transfer functions from force to voltage and current and the relation between current and voltage. This will be compared with the current results which would be obtained if the voltage were applied to a pure capacitance with a value equal to that of the actuator when constrained not to bend.

2.2.1 Response to sinusoidal excitation

In designing or selecting the amplifier for implementing structural control, the expected voltage and current levels must be known. Taking the Laplace transforms of Eq. 2.24 and the derivative of Eq. 2.20, the transfer functions from an applied disturbance to the voltage and current are found to be

$$\frac{\bar{V}_a(p)}{\bar{F}_d(p)} = -\frac{2\zeta_a}{\tilde{e}} \frac{p}{p^2+2\zeta p+1} \tag{2.27}$$

$$\frac{\bar{i}_a(p)}{\bar{F}_d(p)} = \frac{2\zeta_a \tilde{e}}{\tilde{K}^2} \frac{p\left(\frac{\tilde{K}^2}{2\zeta_a} - p\right)}{p^2+2\zeta p+1} \tag{2.28}$$

where p is the nondimensional Laplace variable. The nature of the load which appears at the output of the amplifier may be obtained by taking the ratio of these two responses; when the independent variable, the disturbance force, is thus eliminated, the apparent admittance is found to be

$$\frac{\bar{i}_a(p)}{\bar{V}_a(p)} = p\frac{\tilde{e}^2}{\tilde{K}^2} - \frac{\tilde{e}^2}{2\zeta_a} \tag{2.29}$$

From this admittance, it is apparent that at high frequencies, the load is capacitive, but at low frequencies the actuator behaves like a negative resistance. This is understandable when the intended direction of power flow is considered. Since the control being implemented is designed to provide active damping by means of the actuator, the phase of the current should be such that the average power flow is from the actuator to the amplifier, rather than from amplifier to actuator. Taken together, the real and reactive parts of the actuator load could be represented by a capacitor in parallel with a negative resistor, as shown in Figure 2.3.

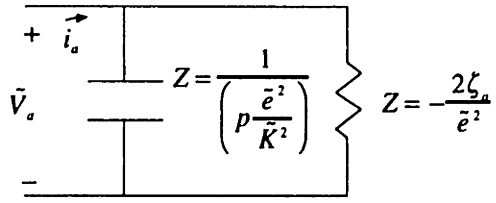

Fig. 2.3. Equivalent load appearing at amplifier output when active damping loop is closed.

It is clear from Eq. 2.29 and the magnitude and phase plots of the apparent admittance in Figure 2.4 that the frequency of the transition from negative resistive to capacitive behavior depends on the de-rated electromechanical coupling factor and the amount of active damping desired. It is interesting to note that if the active damping implemented is small compared to the de-rated coupling, the admittance is that of a negative resistor for a large band of frequencies, but for large amounts of active damping or small coupling factors, the admittance appears more nearly that of a pure capacitance.

Turning aside for the moment to consider the position feedback case, Eq. 2.25 can be combined with the sensor equation Eq. 2.20 to yield the voltage and current responses to the external force:

$$\frac{\tilde{V}_a(p)}{\tilde{F}_d(p)} = -\frac{\kappa}{\tilde{e}} \frac{1}{p^2 + 2\zeta_o p + (1+\kappa)} \tag{2.30}$$

$$\frac{\tilde{i}_a(p)}{\tilde{F}_d(p)} = \frac{\tilde{e}}{\tilde{K}^2} \frac{p\left(\tilde{K}^2 - \kappa\right)}{p^2 + 2\zeta_o p + (1+\kappa)} \tag{2.31}$$

As before, the apparent load admittance is obtained by taking the ratio of these two responses:

$$\frac{\tilde{i}_a(p)}{\tilde{V}_a(p)} = p\frac{\tilde{e}^2}{\tilde{K}^2} - p\frac{\tilde{e}^2}{\kappa} \tag{2.32}$$

Thus if the feedback is stiffening ($\kappa > 0$) the negative resistor of Figure 2.3 becomes a negative capacitor of magnitude $-\frac{\tilde{e}^2}{\kappa}$, which, in parallel with the inherent capacitance of the piezoelectric, will act to reduce the total size of the capacitive load. Similarly, if acceleration is fed back as in Eq. 2.26, the voltage and current responses are

$$\frac{\tilde{V}_a(p)}{\tilde{F}_d(p)} = -\frac{\mu}{\tilde{e}} \frac{p^2}{(1+\mu)p^2 + 2\zeta_o p + 1} \tag{2.33}$$

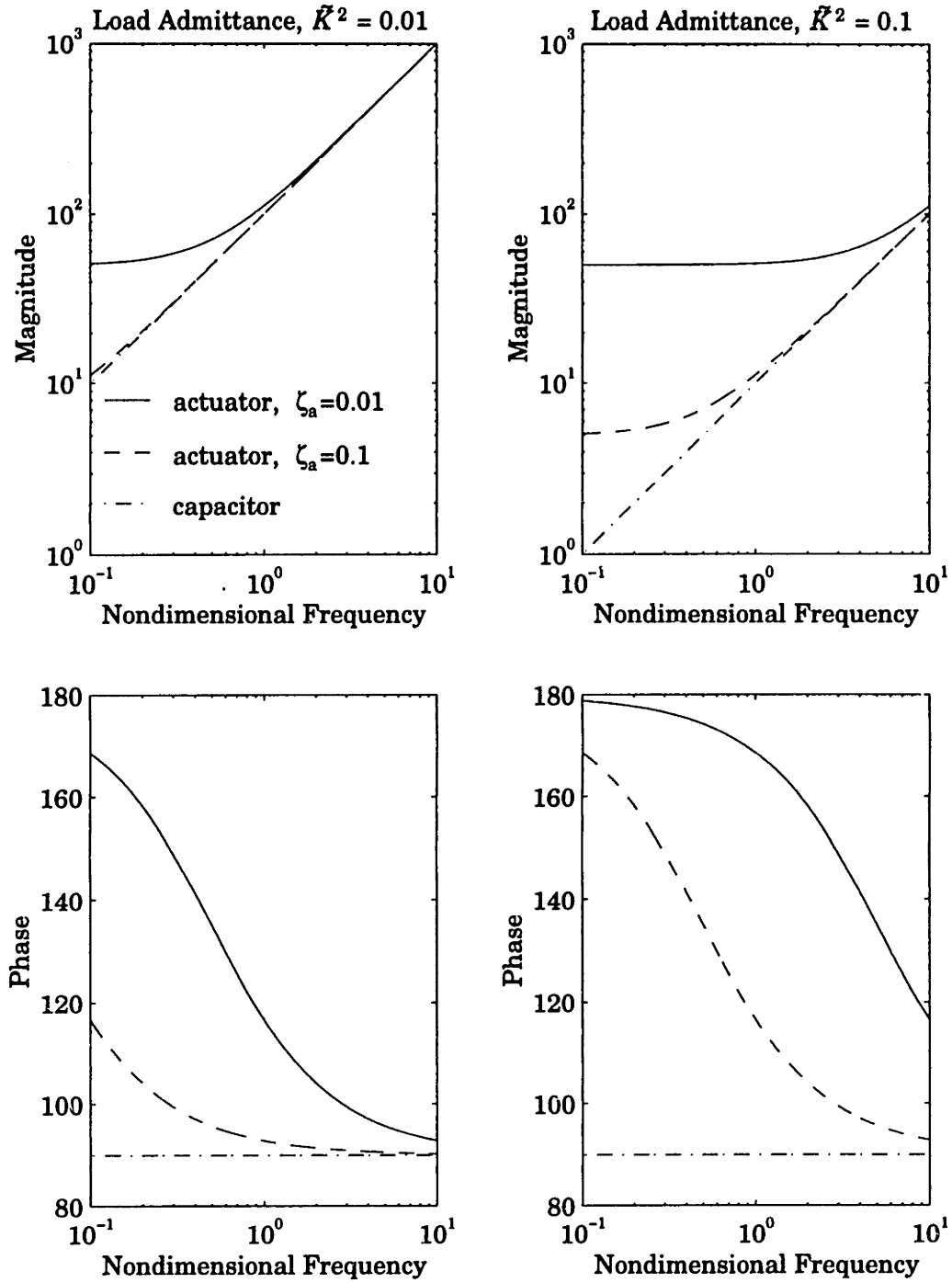

Fig. 2.4. Magnitude and phase of admittance of apparent load of Fig. 2.3 for various values of electromechanical coupling and active damping. Equivalent capacitor included for comparison.

$$\frac{\tilde{i}_a(p)}{\tilde{F}_d(p)} = \frac{\tilde{e}}{\tilde{K}^2} \frac{p\left(\tilde{K}^2 - \mu\right)}{(1+\mu)p^2 + 2\zeta_o p + 1} \tag{2.34}$$

and their ratio gives the apparent admittance

$$\frac{\tilde{i}_a(p)}{\tilde{V}_a(p)} = p\frac{\tilde{e}^2}{\tilde{K}^2} - \frac{\tilde{e}^2}{p\mu} \tag{2.35}$$

Again, the inherent piezoelectric capacitance appears in parallel with an additional term; this time, an inductor whose magnitude $-\frac{\mu}{\tilde{e}^2}$ is negative if the acceleration is fed back in such a way as to increase the apparent mass of the system ($\mu > 0$).

Before turning to the main question of power flow and dissipation in the rate feedback case, the voltage response to the external disturbance deserves closer examination. From Eq. 2.27 it is seen that for a sinusoidal disturbance the peak voltage response will occur at the natural frequency of the system, here normalized to $\tilde{\omega} = 1$; at this frequency, the magnitude of the response is given by

$$\left|\frac{\tilde{V}_a}{\tilde{F}_d}\right| = \frac{1}{\tilde{e}}\frac{\zeta_a}{\zeta_a + \zeta_n} \approx \frac{1}{\tilde{e}}, \quad \zeta_a >> \zeta_n \tag{2.36}$$

Since the $\tilde{V}_a$ reflects the normalization of the voltage by the coercive field, Eq. 2.36 demonstrates the relationship between the size of the disturbance force and the corresponding commanded voltage. The damping ratio drops out, because although for higher active damping ratios (higher control gains, Eq. 2.24) the same displacement would call for higher voltages, the increased damping reduces the actual displacement response to the disturbance. Thus the disturbance response can be damped as desired, provided the actuator effectiveness $\tilde{e}$ is sufficiently large so that the voltage $\tilde{V}_a$ does not exceed 1 for the given disturbance magnitude. Given this material limit on the range of $\tilde{V}_a$, one could also set the limits of the driving amplifier (nondimensional) voltage supply rails to ± 1; the implications of this will become apparent when power dissipation in the amplifier is considered.

Having determined the frequency dependence of the voltage and current, it is now possible to derive expressions for both the instantaneous and average power flow from the amplifier to the actuator. In the time domain, the voltage and current responses to a sinusoidal disturbance force of magnitude $\tilde{F}_{dm}$ and frequency $\tilde{\omega}$ are multiplied to give the instantaneous power from the amplifier to the actuator:

$$\tilde{P}(t) = \frac{2\zeta_a \tilde{\omega}^2 \tilde{F}_{dm}^2}{(1-\tilde{\omega}^2)^2 + (2\zeta\tilde{\omega})^2} \sqrt{1 + \left(\frac{2\zeta_a \tilde{\omega}}{\tilde{K}^2}\right)^2} \cos(\tilde{\omega}\tilde{t} - \theta)\cos(\tilde{\omega}\tilde{t} - \theta + \theta_e)$$

$$\tan\theta = \frac{2\zeta\tilde{\omega}}{1-\tilde{\omega}^2} \tag{2.37}$$

$$\tan\theta_e = -\frac{2\zeta_a\tilde{\omega}}{\tilde{K}^2}$$

where θ, θ_e are the relative phase of displacement to force and current to voltage, respectively. Integrating over one cycle, the average power flow is found to be

$$\tilde{P}_{ave} = -\frac{\zeta_a \tilde{\omega}^2 \tilde{F}_{dm}^2}{(1-\tilde{\omega}^2)^2 + (2\zeta\tilde{\omega})^2} \tag{2.38}$$

which is simply the loss due to the active component of the total damping. The instantaneous minimum and maximum are

$$\tilde{P}_{min,max} = -\frac{\zeta_a \tilde{\omega}^2 \tilde{F}_{dm}^2}{(1-\tilde{\omega}^2)^2 + (2\zeta\tilde{\omega})^2}\left(1 \pm \sqrt{1 + \left(\frac{2\zeta_a\tilde{\omega}}{\tilde{K}^2}\right)^2}\right) \tag{2.39}$$

The effect of the reactive component of the load can now be seen; as the frequency increases, the capacitance of the piezoelectric actuator requires greater extremes of instantaneous power flow both to and from the amplifier, without affecting the average flow. Comparison with the results of applying the drive signal to a pure capacitance is clearer when the extrema of Eq. 2.39 are rewritten as:

$$\tilde{P}_{min,max} = -\frac{2\zeta_a^2 \tilde{\omega}^2 \tilde{F}_{dm}^2}{\tilde{K}^2\left((1-\tilde{\omega}^2)^2 + (2\zeta\tilde{\omega})^2\right)}\left(\frac{\tilde{K}^2}{2\zeta_a} \pm \sqrt{\left(\frac{\tilde{K}^2}{2\zeta_a}\right)^2 + \tilde{\omega}^2}\right) \tag{2.40}$$

Driving a pure capacitance with the control signal would produce no average power flow (cf. Eq. 2.38 for the actuator) and extreme power flows like

$$\tilde{P}_{min,max,cap} = \mp\frac{2\zeta_a^2 \tilde{\omega}^3 \tilde{F}_{dm}^2}{\tilde{K}^2\left((1-\tilde{\omega}^2)^2 + (2\zeta\tilde{\omega})^2\right)} \tag{2.41}$$

The reactive component of the load is significant for both the average and instantaneous power dissipation in the driving amplifier. Using previously derived expressions for voltage and current (Eq. 2.27, 2.28) and substituting into Eq. 2.23 the corresponding time domain responses to a sinusoidal disturbance, the instantaneous amplifier dissipation becomes

$$\tilde{P}_{amp}(t) = \sqrt{\frac{\left(\frac{2\zeta_a\tilde{\omega}}{\tilde{K}^2}\right)^2 + 1}{(1-\tilde{\omega}^2)^2 + (2\zeta\tilde{\omega})^2}}\tilde{\omega}\tilde{F}_{dm} \times \left(-\frac{2\zeta_a\tilde{\omega}\tilde{F}_{dm}}{\sqrt{(1-\tilde{\omega}^2)^2 + (2\zeta\tilde{\omega})^2}}\cos(\tilde{\omega}\tilde{t} - \theta + \theta_e)\cos(\tilde{\omega}\tilde{t} - \theta) + \tilde{e}\left|\cos(\tilde{\omega}\tilde{t} - \theta)\right|\tilde{V}_S \right) \tag{2.42}$$

This can be integrated over one cycle to find the average power dissipated; after some manipulation, the result is

$$\tilde{P}_{amp,ave} = \frac{\zeta_a\tilde{\omega}^2\tilde{F}_{dm}^2}{(1-\tilde{\omega}^2)^2 + (2\zeta\tilde{\omega})^2} + \frac{4\zeta_a\tilde{e}\tilde{\omega}\tilde{F}_{dm}\tilde{V}_S}{\pi\tilde{K}^2}\sqrt{\frac{\left(\frac{\tilde{K}^2}{2\zeta_a}\right)^2 + \tilde{\omega}^2}{(1-\tilde{\omega}^2)^2 + (2\zeta\tilde{\omega})^2}} \tag{2.43}$$

The first term is the average power flow from the actuator to the amplifier (thus the negative of the value in Eq. 2.38), a direct result of the desired active damping effect. The second term is power drawn from the voltage rails. If the amplifier were viewed as a thermodynamic heat pump, an effectiveness could be defined as the ratio of power extracted from the structural system (the first term) to the power required from the voltage rails (the second term.) Note that in this interpretation, the amplifier would be more effective for larger disturbance levels, as the second term varies directly with the magnitude of the disturbance $\tilde{F}_{dm}$ while the first is proportional to its square. The corresponding term for amplifier power dissipation in a pure capacitor with the same commanded voltage can also be found:

$$\tilde{P}_{amp,ave,cap} = \frac{4\zeta_a\tilde{e}\tilde{\omega}^2\tilde{F}_{dm}\tilde{V}_S}{\pi\tilde{K}^2\sqrt{(1-\tilde{\omega}^2)^2 + (2\zeta\tilde{\omega})^2}} \tag{2.44}$$

This is clearly a modification of the second term of the RHS of Eq. 2.43, and reflects only average power drawn from the supply rails, as the net flow from the capacitor would be zero.

In numerical evaluations of this and later expressions, some definite assumption must be made regarding the relative sizes of the tip force amplitude and the rail voltage. Since the coercive field represents a physical limit on the voltage which can be safely applied to the actuators, it is reasonable to assume that $\tilde{V}_S = 1$. If the actuators are to be used effectively, one would expect that the design disturbance level would cause the applied voltage to approach this limit. For the purposes of plotting average and extreme power flow rates as a function of frequency, it may be assumed that

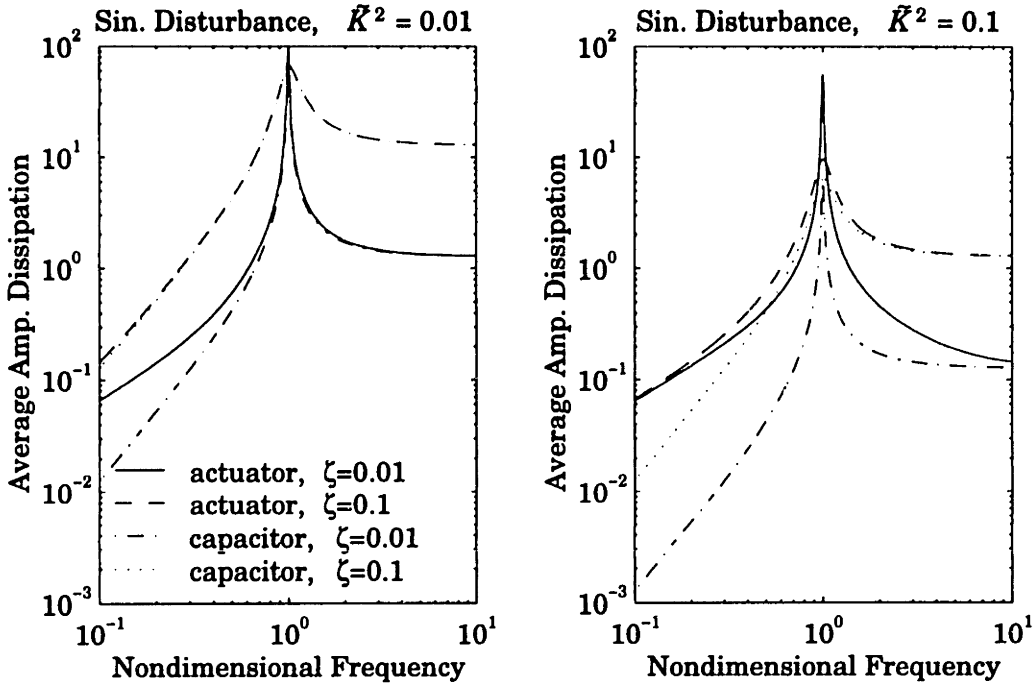

Fig. 2.5. Average amplifier power dissipation as a function of disturbance frequency for two values of electromechanical coupling and active damping, and for equivalent capacitor.

the disturbance force amplitude is fixed at the value which produces the maximum voltage amplitude at the resonance frequency. In Figures 2.5, 2.6 the external force level has been chosen according to Eq. 2.36 to be that which produces the maximum allowable voltage swings at resonance.

Figure 2.5 shows the average power dissipation in the amplifier when the closed-loop system is driven by a sinusoidal disturbance force across a range of frequencies. Results are plotted for two values each of ζ_a and $\tilde{K}^2$. Included for comparison is the power dissipation which would occur in the amplifier were it to drive equivalent ideal capacitors with the same control voltage. It can be seen that for high frequency disturbances, the behavior of the controlled system approaches that of a capacitor, while at low frequencies, the negative resistance component of the controlled system is apparent, especially for low values of active damping and large electromechanical coupling factors.

Figure 2.6 examines more closely the behavior of the system at resonance, where the amplifier dissipation is at a maximum. In the plots on the left, the variation with ζ_a of average amplifier dissipation at resonance is plotted for two values of $\tilde{K}^2$; on the right, $\tilde{K}^2$ is varied for two

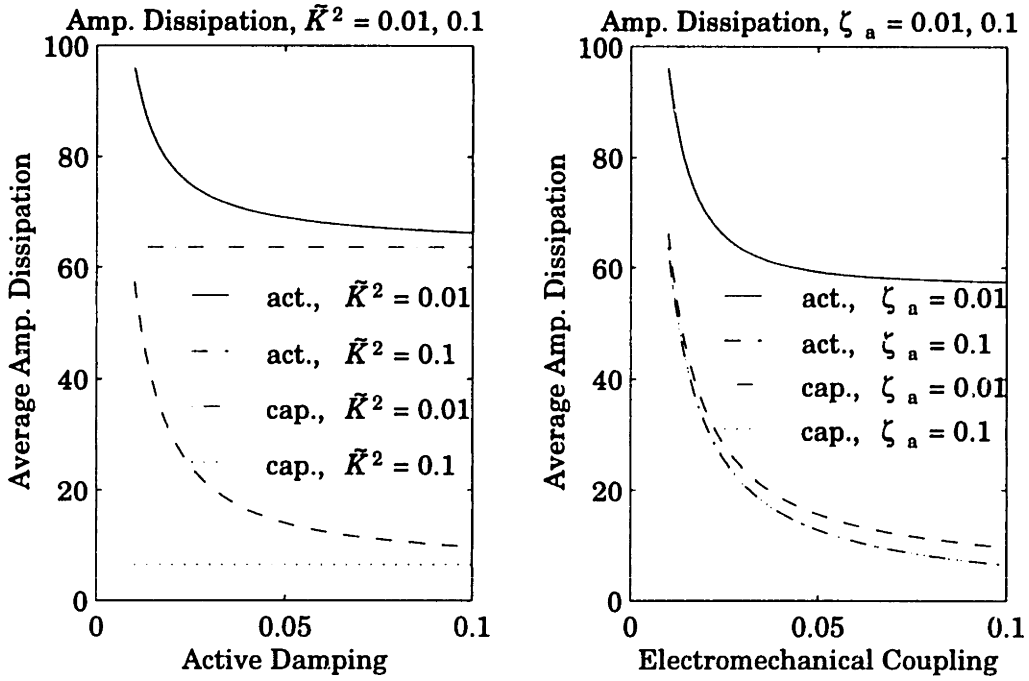

Fig. 2.6. Amplifier power dissipation at resonance as a function of electromechanical coupling and active damping.

values of ζ_a. The dissipation with an equivalent capacitor is included for reference. Again, the behavior of the controlled structure is more like that of a capacitor for combinations of the parameters (large ζ_a and small $\tilde{K}^2$) for which the admittances of Figure 2.4 indicate capacitive behavior.

The reason for the variation with $\tilde{K}^2$ is obvious: for a fixed actuation strength $\bar{e}$, a smaller value of $\tilde{K}^2$ means the inherent capacitance is larger and more power must be dissipated in charging and discharging it. The variation with ζ_a at first seems counterintuitive, but can also be explained physically. At higher damping ratios, the tip motion will be smaller for the same magnitude of disturbance, and thus the power entering the system will be smaller; this is naturally reflected in a lower amplifier dissipation. If the goal of the control is to provide disturbance rejection, a system which maximized the amount of power removed from the system might well be counterproductive, as it could simply be facilitating the entry of energy from the disturbance and increasing structural motion.

Finally, it should be noted again that the curves of Figures 2.5 and 2.6 assume no passive damping. If passive damping is present, Eq. 2.36 indicates that the applied voltage will not be constant with active damping level, but will start at zero, increase with increasing active damping, and

approach a constant as the active damping comes to dominate the total damping. The effect on the amplifier dissipation may be determined from Eq. 2.43; when evaluated at resonance ($\tilde{\omega}=1$), the amplifier dissipation will be lower if there is some passive damping than if there is none. Note, however, that while the amplifier dissipation which would occur with a pure capacitor with the same commanded voltage (Eq. 2.44) goes to zero with zero active damping and non-zero passive damping, this is not true for the actuator case. This is because even if the amplifier is commanding a zero voltage, the disturbance-induced motion causes current to flow through the piezoelectric effect; when this current is drawn from the positive supply or sunk to the negative supply, power is dissipated in the amplifier.

2.2.2 Stochastic response to random excitation

Since disturbances can be broadband rather than sinusoidal, it is also of interest to find root mean square responses for the case in which the tip disturbance is driven by white noise. From the non-zero high frequency asymptote of the current response in Eq. 2.28 it is apparent that excitation by unfiltered white noise will lead to currents with infinite RMS levels. This unrealizable situation may be avoided by modifying the white noise by a single-pole filter to generate the tip force. If ξ is a unit intensity white noise process and $\sigma_{\tilde{F}}$ and $\tilde{\omega}_{\tilde{F}}$ the disturbance RMS level and bandwidth, respectively, the filter is

$$\dot{\tilde{F}}_d = -\tilde{\omega}_{\tilde{F}}\tilde{F}_d + \sqrt{2\tilde{\omega}_{\tilde{F}}}\sigma_{\tilde{F}}\xi \tag{2.45}$$

Note that the second, driving term of the RHS has a frequency scaling to maintain a constant $\sigma_{\tilde{F}}$ as $\tilde{\omega}_{\tilde{F}}$ is varied. Appending this to the equation of motion in Eq. 2.24 (written in matrix form) and writing expressions for currents and the voltage, the system is

$$\begin{bmatrix} \dot{\tilde{q}} \\ \ddot{\tilde{q}} \\ \dot{\tilde{F}}_d \end{bmatrix} = \begin{bmatrix} 0 & 1 & 0 \\ -1 & -2\zeta & 1 \\ 0 & 0 & -\tilde{\omega}_{\tilde{F}} \end{bmatrix} \begin{bmatrix} \tilde{q} \\ \dot{\tilde{q}} \\ \tilde{F}_d \end{bmatrix} + \begin{bmatrix} 0 \\ 0 \\ \sqrt{2\tilde{\omega}_{\tilde{F}}}\sigma_{\tilde{F}} \end{bmatrix} \xi$$

$$\begin{bmatrix} \tilde{i}_a \\ \tilde{i}_c \\ \tilde{V}_a \end{bmatrix} = \begin{bmatrix} \frac{2\tilde{e}\zeta_a}{\tilde{K}^2} & \frac{\tilde{e}\left(\tilde{K}^2 + 4\zeta\zeta_a\right)}{\tilde{K}^2} & -\frac{2\tilde{e}\zeta_a}{\tilde{K}^2} \\ \frac{2\tilde{e}\zeta_a}{\tilde{K}^2} & \frac{4\tilde{e}\zeta\zeta_a}{\tilde{K}^2} & -\frac{2\tilde{e}\zeta_a}{\tilde{K}^2} \\ 0 & -\frac{2\zeta_a}{\tilde{e}} & 0 \end{bmatrix} \begin{bmatrix} \tilde{q} \\ \dot{\tilde{q}} \\ \tilde{F}_d \end{bmatrix} \tag{2.46}$$

where the terms for computing the capacitor current have been included. The Lyapunov equation for the first equation may now be solved to obtain the state covariance matrix, to which the observation matrix in the second equation may be applied to obtain analytic expressions for the RMS levels of current and voltage:

$$\frac{\sigma_{\tilde{V}_a}}{\sigma_{\tilde{F}}} = \frac{\sqrt{2}\zeta_a}{\tilde{e}\sqrt{\zeta}} \sqrt{\frac{\tilde{\omega}_{\tilde{F}}}{1 + 2\zeta\tilde{\omega}_{\tilde{F}} + \tilde{\omega}_{\tilde{F}}^2}}$$

$$\frac{\sigma_{\tilde{i}_a}}{\sigma_{\tilde{F}}} = \frac{\sqrt{2}\tilde{e}\zeta_a}{\tilde{K}^2\sqrt{\zeta}} \sqrt{\frac{\tilde{\omega}_{\tilde{F}}\left(\left(\frac{\tilde{K}^2}{2\zeta_a}\right)^2 + 1 + 2\zeta\tilde{\omega}_{\tilde{F}}\right)}{1 + 2\zeta\tilde{\omega}_{\tilde{F}} + \tilde{\omega}_{\tilde{F}}^2}} \qquad \frac{\sigma_{\tilde{i}_c}}{\sigma_{\tilde{F}}} = \frac{\sqrt{2}\tilde{e}\zeta_a}{\tilde{K}^2\sqrt{\zeta}} \sqrt{\frac{\tilde{\omega}_{\tilde{F}}\left(1 + 2\zeta\tilde{\omega}_{\tilde{F}}\right)}{1 + 2\zeta\tilde{\omega}_{\tilde{F}} + \tilde{\omega}_{\tilde{F}}^2}} \tag{2.47}$$

The ratios of actual current and pure capacitive current to the voltage level are then

$$\frac{\sigma_{\tilde{i}_a}}{\sigma_{\tilde{V}}} = \sqrt{\left(\frac{\tilde{e}^2}{2\zeta_a}\right)^2 + \left(\frac{\tilde{e}^2}{\tilde{K}^2}\right)^2 (1 + 2\zeta_a\tilde{\omega}_{\tilde{F}})} \qquad \frac{\sigma_{\tilde{i}_c}}{\sigma_{\tilde{V}}} = \frac{\tilde{e}^2}{\tilde{K}^2}\sqrt{1 + 2\zeta_a\tilde{\omega}_{\tilde{F}}} \tag{2.48}$$

Again, the combination of the de-rated coupling factor and active damping ratio appears. In Eq. 2.47, 2.48 the current response of the actuator is the square root of the sum of the squares of the response to a capacitor alone and the response to a resistor alone. This can be explained by considering the actuator load to be equivalent to a capacitance in parallel with a negative resistor, as suggested in the previous section. The same control voltage is applied to both components and the current in the negative resistance will thus be proportional to the derivative of the current in the capacitance. Since a random signal with a constant RMS is uncorrelated with its derivative, the variance of the total current is the sum of the variances of the two components.

For the average electrical power flow into the actuator in the presence of

a random excitation, the expectation of the instantaneous product of actuator voltage and current is required; this is just the correlation of voltage and current. If both variables are zero mean (true for a zero mean F_d) this is equal to the covariance of voltage and current. The off-diagonal terms of the covariance matrix for the system of Eq. 2.46 yield the covariances of the outputs; the appropriate element in this case is

$$\tilde{P}_{ave} = \mathrm{cov}(\tilde{i}_a \tilde{V}_a) = -\frac{\zeta_a}{\zeta}\sigma_{\tilde{F}}^2 \frac{\tilde{\omega}_{\tilde{F}}}{1 + 2\zeta\tilde{\omega}_{\tilde{F}} + \tilde{\omega}_{\tilde{F}}^2} \tag{2.49}$$

As in the sinusoidal excitation case, the negative sign represents power flow from the actuator to the amplifier, and the fraction of damping power due to the active control can be identified.

A higher order statistic is needed to provide a measure of the magnitude of the expected excursions of instantaneous power. For random variables with a Gaussian distribution, the standard deviation serves this purpose well. The instantaneous power, however, is a product of two Gaussians; in general, its distribution will not be Gaussian. A momentary consideration of power flow into two loads can illustrate this point. For a resistive load, the voltage and current are linearly related so that the instantaneous power is always non-negative with a single-ended distribution that is clearly non-Gaussian, while for a capacitive load, voltage and current are uncorrelated and the distribution of the instantaneous power will be a Gaussian squared. In general the simple and useful Gaussian relation between standard deviation and probability of exceedance will not hold for the instantaneous power.

Nevertheless, the standard deviation does give some notion of the size of the excursions. First, the variance may be expanded:

$$\sigma_{\tilde{P}}^2 = \mathrm{E}\left(\tilde{P}^2\right) - \tilde{P}_{ave}^2 \tag{2.50}$$

The second term is already known from Eq. 2.49; to find the first term, the definition of the characteristic function of a random vector with normally distributed elements [Jazwinski, 1970] is applied; after some manipulation it becomes

$$\mathrm{E}\left(\tilde{P}^2\right) = 2\,\mathrm{cov}^2(\tilde{i}_a \tilde{V}) + \sigma_{\tilde{i}_a}^2 \sigma_{\tilde{V}}^2 = 2\tilde{P}_{ave}^2 + \sigma_{\tilde{i}_a}^2 \sigma_{\tilde{V}}^2 \tag{2.51}$$

so that the variance of the power is

$$\sigma_{\tilde{P}}^2 = \tilde{P}_{ave}^2 + \sigma_{\tilde{i}_a}^2 \sigma_{\tilde{V}}^2 = \frac{\zeta_a^2 \tilde{\omega}_{\tilde{F}}^2 \sigma_{\tilde{F}}^4}{\zeta^2 \left(1 + 2\zeta\tilde{\omega}_{\tilde{F}} + \tilde{\omega}_{\tilde{F}}^2\right)^2} \left(\left(\frac{2\zeta_a}{\tilde{K}^2} \right)^2 \left(1 + 2\zeta_a \tilde{\omega}_{\tilde{F}}\right) + 2 \right) \tag{2.52}$$

and the standard deviation is

$$\sigma_{\tilde{P}} = \left(\frac{2\zeta_a}{\tilde{K}^2} \right) \left(\frac{\zeta_a}{\zeta} \right) \frac{\tilde{\omega}_{\tilde{F}}}{1 + 2\zeta\tilde{\omega}_{\tilde{F}} + \tilde{\omega}_{\tilde{F}}^2} \sigma_{\tilde{F}}^2 \sqrt{1 + 2\zeta_a \tilde{\omega}_{\tilde{F}} + 2\left(\frac{\tilde{K}^2}{2\zeta_a} \right)} \tag{2.53}$$

The corresponding value for a pure capacitive load would be

$$\sigma_{\tilde{P},cap} = \left(\frac{2\zeta_a}{\tilde{K}^2} \right) \left(\frac{\zeta_a}{\zeta} \right) \frac{\tilde{\omega}_{\tilde{F}}}{1 + 2\zeta\tilde{\omega}_{\tilde{F}} + \tilde{\omega}_{\tilde{F}}^2} \sigma_{\tilde{F}}^2 \sqrt{1 + 2\zeta_a \tilde{\omega}_{\tilde{F}}} \tag{2.54}$$

Comparing these two results, it appears that the non-capacitive load not only produces a non-zero average power flow but also increases the extreme values of the instantaneous power flow. This effect diminishes for disturbances with broader bandwidths as the capacitive component dominates at higher frequencies.

In considering the dissipation in the amplifier, it should be noted that the actuator voltage cannot have a true Gaussian distribution, since the amplifier has distinct saturation limits. The error associated with the Gaussian distribution assumption is small for situations in which $\tilde{V}_a$ is twice the standard deviation of the Gaussian distribution; in such a case the saturated RMS voltage differs from the unsaturated value by less than 5%. With this caveat in mind, the average dissipation in the amplifier may be computed. The expectation of the first term of Eq. 2.23 will just give the average power removed from the structure by the active damping; the second term is obtained by computing the mean of the absolute value of a Gaussian distribution:

$$\mathrm{E}\left(\left|\tilde{i}_a\right|\right) = \int_{-\infty}^{\infty} \left|\tilde{i}_a\right| \frac{1}{\sqrt{2\pi}\sigma_{\tilde{i}_a}} \exp\left(-\frac{\tilde{i}_a^2}{2\sigma_{\tilde{i}_a}^2} \right) d\tilde{i}_a = \sqrt{\frac{2}{\pi}} \sigma_{\tilde{i}_a} \tag{2.55}$$

When this is done, the average power dissipated is found to be

$$\tilde{P}_{amp,ave} = -\mathrm{cov}(\tilde{i}_a, \tilde{V}_s) + \sqrt{\frac{2}{\pi}} \sigma_{\tilde{i}_a} \tilde{V}_s = \frac{\zeta_a}{\zeta} \sigma_{\tilde{F}}^2 \frac{\tilde{\omega}_{\tilde{F}}}{1 + 2\zeta\tilde{\omega}_{\tilde{F}} + \tilde{\omega}_{\tilde{F}}^2} + \frac{2\tilde{e}\zeta_a}{\sqrt{\pi}\tilde{K}^2\sqrt{\zeta}} \sqrt{\frac{\tilde{\omega}_{\tilde{F}} \left(\left(\frac{\tilde{K}^2}{2\zeta_a} \right)^2 + 1 + 2\zeta\tilde{\omega}_{\tilde{F}} \right)}{1 + 2\zeta\tilde{\omega}_{\tilde{F}} + \tilde{\omega}_{\tilde{F}}^2}} \sigma_{\tilde{F}} \tilde{V}_s \tag{2.56}$$

If the pure capacitor were driven with the control signal, the average dissipation would be

$$\tilde{P}_{amp,ave,cap} = -\mathrm{cov}(\tilde{i}_c \tilde{V}) + \sqrt{\frac{2}{\pi}}\sigma_{\tilde{i}_c}\tilde{V}_S = \frac{2\tilde{e}\zeta_a}{\sqrt{\pi}\tilde{K}^2\sqrt{\zeta}}\sqrt{\frac{\tilde{\omega}_{\tilde{F}}\left(1+2\zeta\tilde{\omega}_{\tilde{F}}\right)}{1+2\zeta\tilde{\omega}_{\tilde{F}}+\tilde{\omega}_{\tilde{F}}^2}}\sigma_{\tilde{F}}\tilde{V}_S \qquad (2.57)$$

As with the sinusoidal results of the previous section, the RMS amplifier power dissipation could be shown as a function of frequency (now the bandwidth of a broad disturbance rather than a sharp sinusoid) for different values of active damping and electromechanical coupling. Such a plots are omitted here, as they substantially reflects the information found in Figure 2.5, though broadband nature of the disturbance naturally tends to result in much broader curves of power dissipation vs. disturbance bandwidth.

2.3 Conclusions

Power dissipation is an important consideration in the design of increasingly integrated controlled structures with increasingly miniaturized support electronics. The state-space formulation employed in this work allows straightforward calculation of power flow and dissipation quantities. For a closed-loop system whose response is dominated by a single mode, interesting and useful parameters for power flow in a closed-loop system have been derived. The significance of generalized piezoelectric constants, electromechanical coupling coefficients, and controller parameters has been demonstrated, along with expressions for the current, voltage, and power dissipation requirements for different levels of active damping, actuator strength, and disturbance spectral content.

CHAPTER 3: EXPERIMENTAL MEASUREMENT OF POWER FLOW AND DISSIPATION

The objective of the work described in this chapter is to construct a simple controlled structure to verify and explore the limitations of power modeling concepts developed in Chapter 2. This chapter will detail the development and implementation of an actuator package in which piezoelectric ceramics are integrated along with the electronic components which power them. The packaging design must satisfy requirements for mechanical, electrical, and chemical isolation of the integrated circuit and at the same time provide for the disposal of the heat dissipated in the electrical components, so that their temperatures do not exceed operational limits. A cantilever beam experiment was designed using two of the actuator packages. The electromechanical modeling approach of [Hagood, Chung, and von Flotow, 1990] is again applied, this time to a nonuniform, multi-mode beam. The experimental open loop response is compared to that of the model, noting limitations imposed by nonlinearities. Under external disturbance with approximate rate feedback, the negative resistive apparent load impedance derived in Chapter 2 is observed. Finally, measurements of power flow and amplifier dissipation are presented, illustrating the importance of amplifier nonidealities and piezoelectric nonlinearities.

In the following section, the composition and fabrication of the integrated package is described.

3.1 Actuator Package Design and Manufacture

3.1.1 Piezoelectric elements

Design criteria for the actuator package are derived from its eventual projected application in a fully integrated intelligent structure, in which the package may be physically embedded within a graphite-epoxy structure or bonded to the surface. Functional requirements included actuation authority similar to that of the actuator used with the active wing of [Lin, Crawley, and Heeg, 1995] illustrated in Figure 1.1 of Section 1.2.1, and the ability to amplify low voltage control signals to appropriately large voltage levels. Piezoelectric elements measuring 48 mm x 31 mm x 0.025 mm of type PSI-5A-S2 (nominal modulus 61 GPa, dielectric constant 1700, piezoelectric strain coefficient -171 pm/V) from Piezo Systems, Inc. (Cambridge, MA) were chosen to satisfy the first requirement.

The analytical development of the previous chapter assumed linear constitutive relations for the piezoelectric ceramic. For the purposes of model verification, material properties such as the piezoelectric coefficient d_{31} and the free dielectric constant ε_{33}^{S} must be measured and deviations from ideal behavior noted.

A 0.254 mm thick sample of piezoelectric ceramic measuring 15.4 mm by 38.1 mm was instrumented with a strain gage and driven with a amplifier circuit similar to that described in Section 3.1.2, modified to accommodate the difference in between the capacitance of the sample and that of the package. The sample was then excited with a random voltage from 0-200 Hz at high (17.8 Vrms) and low (3.56 Vrms) excitation levels, identical to the levels used in the open loop cantilever beam tests described below in Section 3.3.2. The resulting strain and current responses are plotted in Figures 3.1 and 3.2. The strain response (in units of strain per applied voltage) was multiplied by the sample thickness to yield strain per applied electric field; since the sample was unconstrained, the resulting value (according to the constitutive relations in Eq. 2.1) is the piezoelectric constant d_{31}, where the subscript 3 refers to the through-thickness applied field direction and the subscript 1 refers to the resulting in-plane deformation. The current response (in amps/volt) was first divided by $j\omega$ to produce the charge response

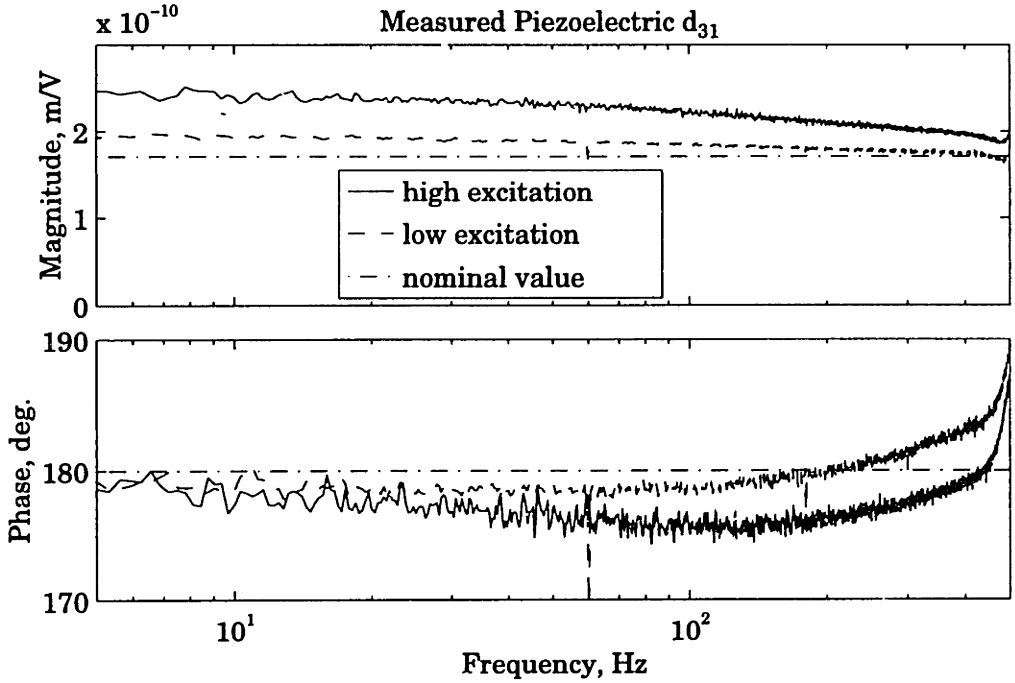

Fig. 3.1. Piezoelectric constant for sample of PSI-5A-S2. High and low excitation levels are compared with manufacturer's quoted value.

(capacitance, in farads), which was then divided by the sample area and multiplied by the thickness to obtain the dielectric constant. This in turn was normalized by the dielectric constant of free space, 8.854×10^{-12} F/m, for comparison with the manufacturer's quoted material properties.

The electric field strengths for the high and low excitation cases are 70.2 kV/m RMS and 14.0 kV/m RMS, respectively. These levels are 10% and 2% of the AC depoling field, taken to be 700 kV/m for this material. The increase in apparent d_{31} is consistent with the behavior described in [Crawley and Anderson, 1990], in which the strain nonlinearity of d_{31} was observed quasi-statically. The dynamic effects of the nonlinearity of the piezoelectric effect are illustrated here as an increased phase loss with excitation level. (The common rise in phase above 200 Hz is a test artifact rather than a true material property. The presence of a strain gage on only one side of the sample under test shifts the neutral axis slightly from the center plane of the sample; the resulting strain response to electric field excitation exhibits a complex zero preceding a resonant bending mode slightly above the frequency bandwidth shown.) Deviations from manufacturer's values are not altogether

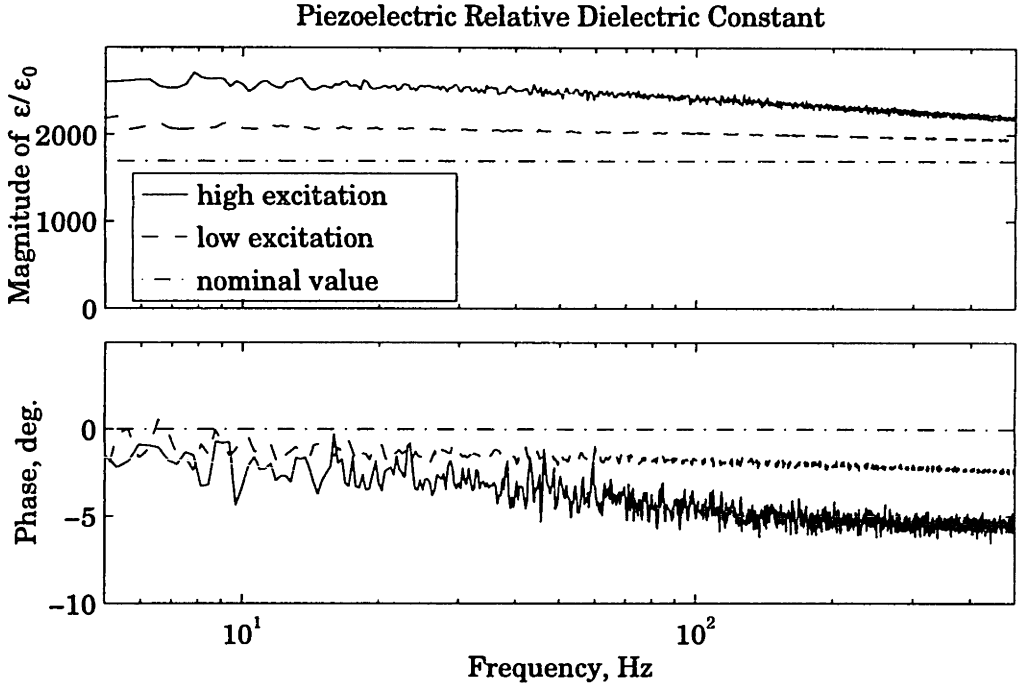

Fig. 3.2. Dielectric constant for sample of PSI-5A-S2. High and low excitation levels are compared with manufacturer's quoted value at 1 kHz.

unexpected, especially since standard piezoelectric characterization protocols often call for measuring properties at very low excitation levels [IEEE, 1978].

For the purposes of this work, the less well-known nonlinearity apparent in the charge response illustrated in Figure 3.2 is of greater significance. The increase in magnitude and in phase loss is of great significance to power computations, since both the power transferred between the amplifier and the actuator and that dissipated in the amplifier itself depend on both the magnitudes and relative phase of the current and voltage. To further investigate this phenomenon, the time domain behavior is key, since the presence of a nonlinearity invalidates the strict transfer function interpretation of broadband responses such as those shown above. Time responses for the actuator patch as a whole are discusses in Section 3.5 below.

3.1.2 Electronic components

The functional requirement for power amplification was satisfied by a PA41 operational amplifier manufactured by APEX, Inc. (Tucson, AZ) was

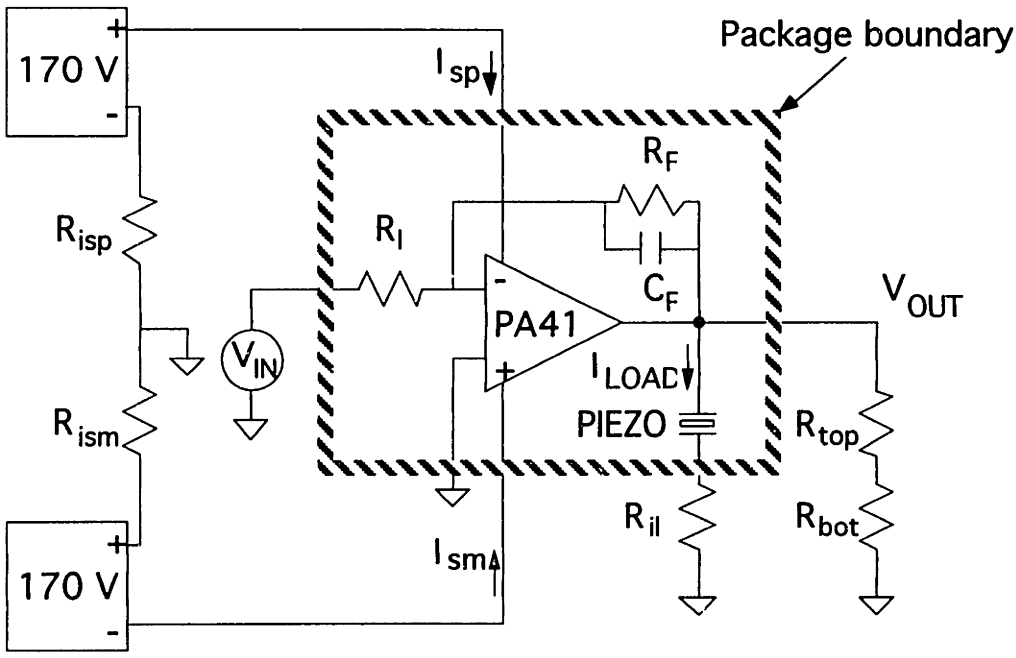

Fig. 3.3. Schematic showing actuator, PA41 operational amplifier, and passive components within package and external power supplies, signal source, and resistors for measuring current and voltage.

chosen for power amplification. When supplied with line voltages of +170 V and -170 V, this device is capable of an output voltage swing from -160 V to +160 V, and can source or sink up to 80 mA of current instantaneously (60 mA continuously). While larger voltage and current ranges available with other devices would have allowed a range of operation over larger voltages and frequencies, the PA41 is unusual in that it is a monolithic device (manufactured on a single piece of silicon measuring 3.78 mm x 5.16 mm x 0.51 mm) and is available in die form. This absence of conventional packaging allows the construction of a very thin actuator package suitable for embedding in composites, while at the same time making necessary a careful consideration of the immediate die environment, as described later in this section. Figure 3.3 shows a schematic of the circuit used to achieve the voltage and power amplification.

Within the package, the input and feedback resistors R_I and R_F are 5 KΩ and 200 KΩ, respectively. The ratio of values was chosen to provide the desired gain of 40, and the large value of the feedback resistor reduces the current required from the operational amplifier. Like most operational amplifiers, the PA41 has a high DC gain and a low frequency pole; the pole

added by the combination of a capacitive load and the amplifier's output resistance can result in closed loop instabilities. This is prevented by compensating the feedback gain with the 47 pF feedback capacitor C_F. The small resistors R_{il} , R_{isp} , and R_{ism} yield voltages which measure the load current and the positive and negative supply currents, respectively, while the high-impedance voltage divider formed by R_{top} and R_{bot} allows measurement of the output voltage. These measurements provide the capability for computing the power flows between the amplifier and the load, and from two 170 V power supplies to the amplifier. Combining these components, the total power dissipated in the amplifier is

$$P_{amp}(t) = -I_{LOAD}(t)V_{OUT}(t) + I_{sp}170\,\mathrm{V} + I_{sm}(-170\,\mathrm{V}) \qquad (3.1)$$

where the first term on the right hand side is power delivered to the load and the remaining two terms are power delivered from the positive voltage rail and the negative voltage rail, respectively. Note that component values have been chosen so that the voltage drops across current measuring resistors and the current drawn by the voltage divider and the feedback resistor are essentially negligible.

3.1.3 Packaging materials and assembly

Given the basic components of the actuator package, major areas of concern in manufacturing are electrical, mechanical, chemical, and thermal. Electrical connections must be established between the piezoelectric elements and the amplifier, and among the electronic components themselves. Non-actuating constituents of the package should provide as little mechanical constraint as possible to the piezoelectric elements while facilitating good strain transfer from the actuator to the structure to be controlled [Crawley and de Luis, 1987]. The operational amplifier must be incorporated in such a way that electrical connections are maintained in the presence of operational stresses and the chip is isolated from ionic contaminants which could hasten failure of the electronics. At the same time, a thermal path between the chip and the environment must be provided for disposal of heat generated in the operational amplifier so that chip temperatures do not exceed the 150 C operational limit.

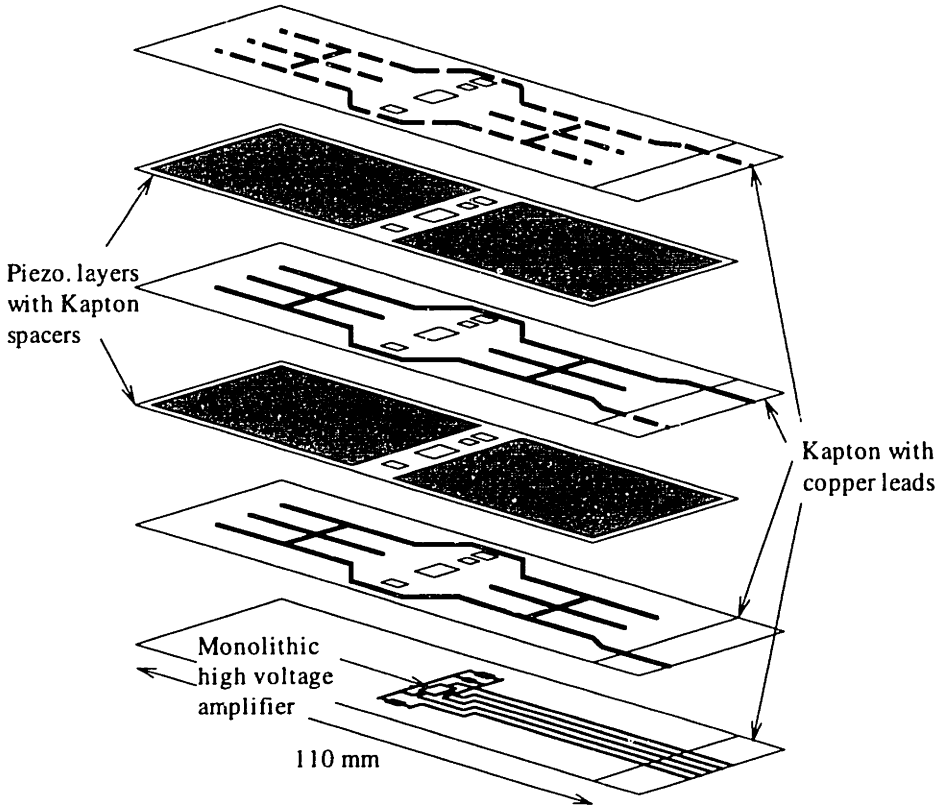

Fig. 3.4. Exploded view of piezoelectric actuator package incorporating power amplification circuitry.

An exploded view of the actuator package as currently manufactured is shown in Figure 3.4. Overall dimensions are 110 mm x 35 mm x 0.085 mm. The piezoelectric elements themselves are electrically insulated from the surroundings by layers of 0.025 mm thick Kapton polyimide film, chosen for its high dielectric strength, and electrical connection between the elements and external connections is provided by copper leads formed by etching patterns in a layer of 0.025 mm thick copper bonded to the Kapton. The edges of the piezoelectric elements are protected by Kapton spacers with combined thickness equal to that of the elements. The copper/Kapton layers, the piezoelectric elements, and the Kapton spacers are assembled as a unit with a coating of Hysol Epoxy-Patch 0151 from Dexter (Seabrook, NH) between each layer. The assembly is cured between two aluminum plates within a vacuum bag at 60 C for two hours. The PA41 operational amplifier die is affixed to its flexible circuit with a small amount of HIPEC 3-6550, an electronics-grade room-temperature vulcanizing (RTV) silicone from Dow Corning (Midland, MI), and wire bonds are made between bond pads on the die and the copper patterns on the Kapton film. This flexible circuit is then

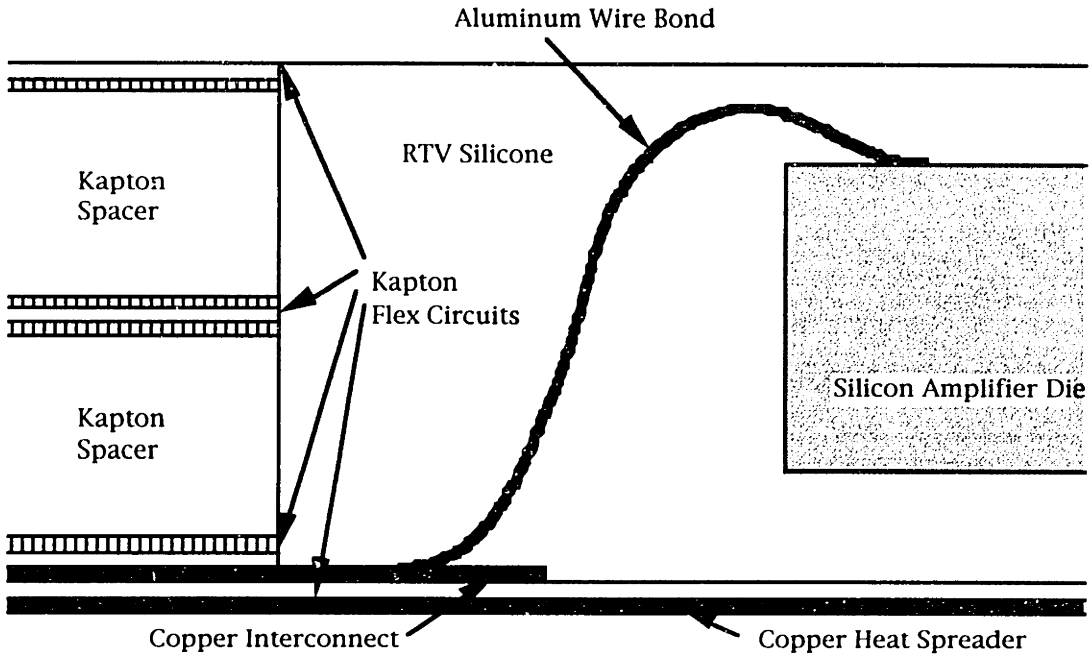

Fig. 3.5. Cross section detail of operational amplifier chip wire-bonded to flex circuit and surrounded by RTV silicone.

bonded to the previously assembled components, and the wells around the electronic components are filled with more RTV. Figure 3.5 shows a cut-away detail of the amplifier die surrounded by RTV with wire bonds to the copper leads on the Kapton flex circuit.

To date, the packages have been successfully constructed as far as the final assembly step; post-cure examination and tests suggest that insufficient clearance between the well walls and the amplifier die has resulted in damage to the wire bonds. Prior work [Warkentin, Crawley, and Senturia, 1992] has shown that embedding electronic components is possible using a different interconnection method; instead of aluminum wire bonds, extensions of the copper leads themselves were thermosonically bonded to the chip. As the problem of electrical connection could thus be regarded as essentially solved, the rectification of the difficulties encountered in this instance was not pursued. The flawed packages still perform properly as actuators, and have been converted to thermal simulators by replacing the non-functioning die with a piece of brass with a 1000 Ω strain gage and a very fine thermocouple. The application of voltage to the strain gage allows for simulation of amplifier power dissipation, and the resulting "die"

temperature elevation can be measured with the thermocouple as described in a later section.

3.2 Beam Experimental Apparatus

Figure 3.6 shows the beam experimental apparatus used in this work. Two of the actuator packages described above were bonded to a graphite/epoxy beam and driven with voltages oriented to produce bending. The load current from both packages is sunk through a common measuring resistor, yielding a combined current measurement. Current commanded in the coil bonded to the beam reacts against the field of a permanent magnet, providing an external disturbance force proportional to the commanded current. Displacement is measured at the coil location to allow the computation of disturbance power input, and the tip displacement is measured for feedback through a compensator to the actuator amplifiers.

Note that whereas the analytical example of Chapter 2 had a uniform cross-section and a single mode, the experimental beam will be seen to have sharply varying sectional properties, and the presence of multiple modes makes precise identification of the nondimensionalized quantities of the 1 DOF model difficult at best. Nevertheless, some of the basic characteristics of the power flow phenomena may be observed, as shown in a later section.

3.2.1 Sectional properties of beam and package

The beam used for this work was a graphite/epoxy laminate with a $[0/90/0_2]_S$ layup of unidirectional plies of AS4/3501-6. The beam cross-section measured 35.18 mm x 1.05 mm and the overall length was 356 mm; installed in the aluminum clamp, the cantilever length was 270 mm. The overall mass was 0.01886 kg.

Using the nominal ply thickness of 0.134 mm and moduli established by measurements at TELAC, the effective bending stiffness EI may be calculated according to engineering beam theory from area weighted moduli to be 0.3711 Nm^2. A more sophisticated analysis from classical laminated plate theory (CLPT) yields a value of $EI=D_{11}b$ of 0.3757 Nm^2; if the

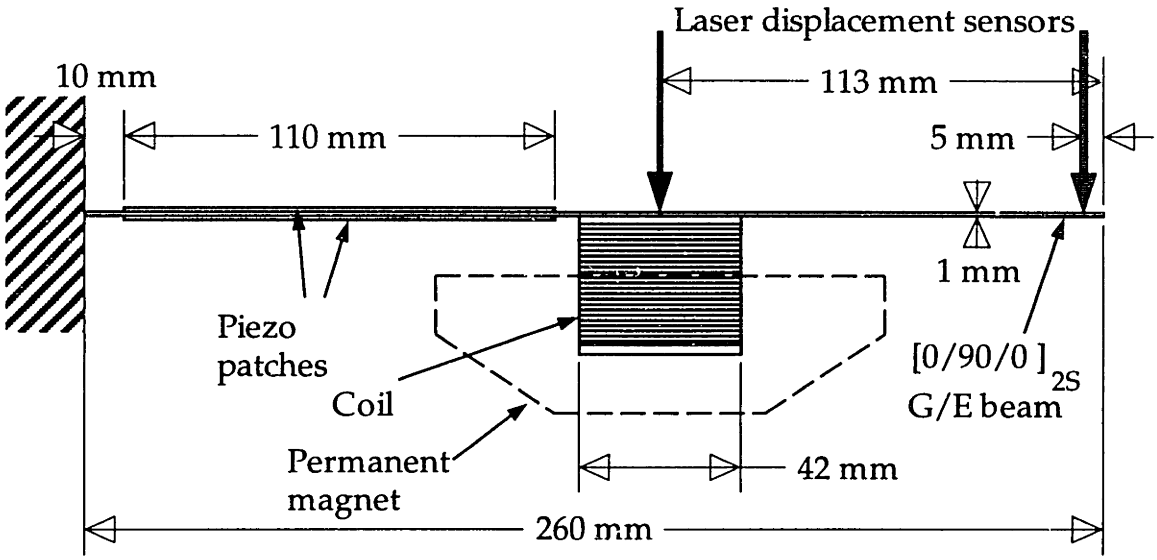

Fig. 3.6. Layout of cantilever beam experiment showing location of piezoelectric actuators, displacement sensors, and disturbance source.

transverse moment is assumed to be zero (allowing anticlastic curvature) the stiffness is 0.3744 Nm^2.

As a check on material properties, the frequency of the first bending mode was measured to be 18.3 Hz with a cantilever length of 254 mm. Given this frequency, the dimensions and mass of the beam, and the formula for the frequency of the first cantilever mode, the derived bending stiffness is found to be 0.2358 Nm^2. At least some of the discrepancy between this value and the predicted value of 0.3711 Nm^2 may be ascribed to two factors. In relatively thin laminates such as this one, the region near the outer surfaces tends to be resin-rich, resulting in a laminate which exhibits less bending stiffness than expected. In addition, this particular laminate was originally fabricated according to a cure cycle consisting of one hour at 250°F and four hours at 300°F, instead of the nominal one hour at 250°F and two hours at 350°F followed by eight hours of post-cure [Warkentin, Crawley, and Senturia, 1992]. The measured extensional stiffness of the specimens fabricated with this modified cure schedule was typically found to be some 5% below the expected value.

Table 3.1 Nominal Material Properties

Material	Modulus, GPa	Density, Kg/m^3	Thermal Cond., W/(mK)	Spec. Heat, J/(kgK)
Kapton	2.5	1420	0.12	1030
Piezoceramic	61	7750	1.8	420
Epoxy	2.5 (est.)	1290	0.20	2000 (est.)
Copper	117	8960	400	385
Graphite/Epoxy	142/9.81	1430	4.62/0.72	1000
Silicon	110	2330	124	702
Silicone RTV	0.001 (est.)	2000 (est.)	0.17	1000 (est.)

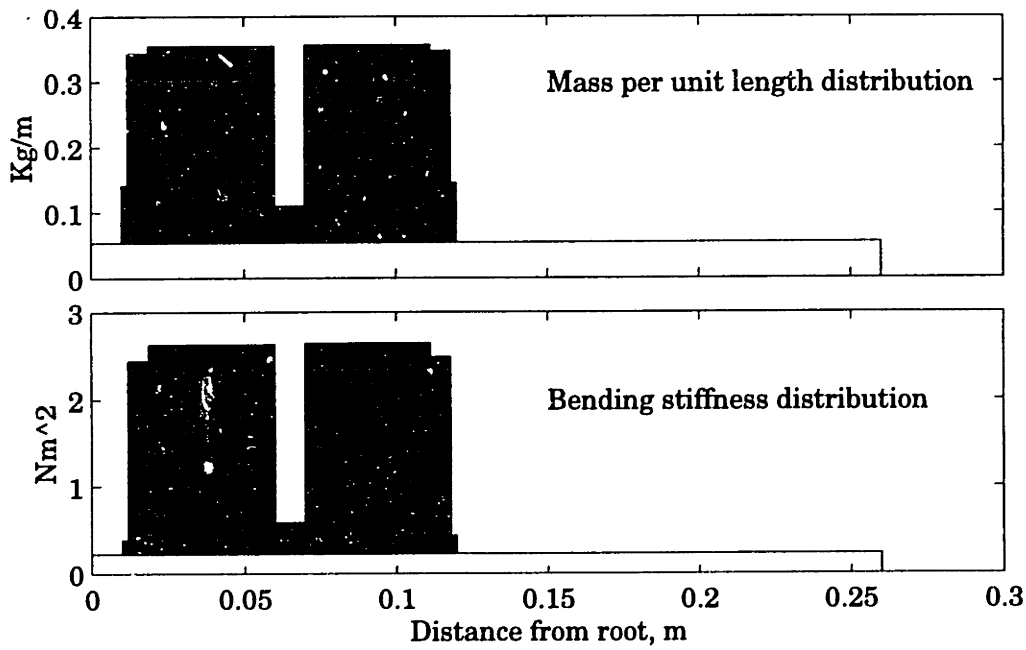

Fig. 3.7. Distribution of sectional properties (excluding coil): white, gray, and black represent contributions from the beam, the piezoceramics, and the remainder of the packaging, respectively.

The distribution of the sectional properties of bending stiffness and mass per unit length of the beam with the two patches is presented in Figure 3.7. The values used for the modulus and density of patch materials are those in Table 3.1; the graphite/epoxy beam values are those derived from the measurements described above. Note that the presence of the patches causes substantial discontinuities in the sectional properties; even the relatively

compliant epoxy and Kapton packaging materials contribute substantially to overall stiffness because of their off-axis locations, and the high modulus and density of the copper layers make their contributions to stiffness and mass significant, despite the small cross-sectional area. The mass of the coil used for the external disturbance force, described below, is not included in the distributed mass per unit length. The total beam mass was 14.1 g; the packages were each 13.5 g.

3.2.2 Displacement sensors

The deflection of the beam 5 mm from the tip and at the center of the coil were measured by laser displacement sensors (LB-11/70 from Keyence Corp., Fair Lawn NJ.) The tip measurement was used for control, while the other displacement formed an energy dual with the coil force, allowing calculation of power input from the disturbance source. At the 0.7 ms response setting ("the time needed to reach 90% of the final value for a quickly moving target"), the manufacturer specifies a -3 dB frequency of 700 Hz; the frequency response of the sensors was modeled with a real pole at this frequency and a first order Pade approximation of a time delay of 0.35 ms. The sensors were adjusted to yield a sensitivity of approximately 1 V for a displacement of 10 mm.

3.2.3 Disturbance source

In order to provide an independent disturbance source similar to the tip force in the 1-DOF example, a magnetic force actuator was constructed. This consisted of a large permanent magnet (obtained from a 30 cm speaker) and a 4 cm diameter coil of 90 turns of 27 gage copper wire wound on a thin hollow cylinder of Teflon. To eliminate the need for additional flexures, the coil was bonded directly to the beam 115 mm from the tip, near the end of the actuator patches. Placement at this point rather than at the tip reduced the required coil travel, ensuring that the number of coil turns within the effective field area of the magnet remained constant, thus maintaining the linear relationship of coil current to applied force. By comparing the deflection of the beam due to coil current to the deflection produced by the weight of test masses placed at the coil location, the ratio of disturbance force

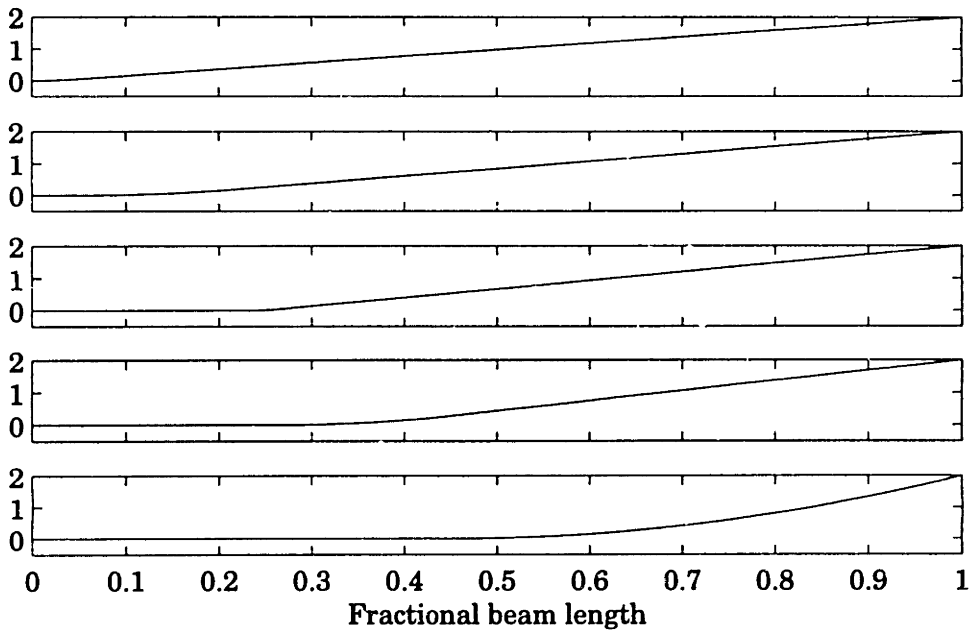

Fig. 3.8. Five trial functions used in Rayleigh-Ritz formulation in addition to uniform mode shapes. Second and fourth have uniform curvature at piezoceramic locations; first, third, and fifth have uniform curvature elsewhere.

to commanded current was found to be 2.54 N/A. The total mass of the coil was 12.6 g.

3.3 Electromechanical Model

3.3.1 Trial functions, static shapes, and mode shapes

As was the case for the 1-DOF model in Chapter 2, a Rayleigh-Ritz model of the beam was formulated. Basis functions included the first 10 exact uniform cantilever beam mode shapes, as well as five additional shapes selected to reflect the major discontinuities in sectional properties, and to more exactly capture static deflection shapes. These five shapes are shown in Figure 3.8; each consists of a region of constant, non-zero curvature in an area of approximately constant sectional properties. As with the exact cantilever shapes, the deflections were normalized to produce a nondimensional tip deflection of 2.

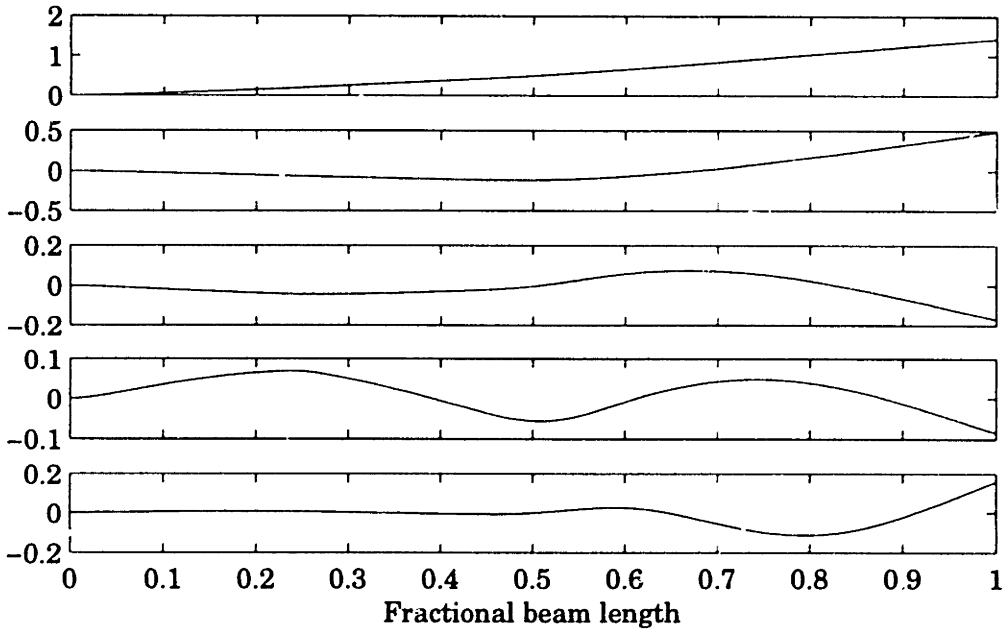

Fig. 3.9. First five displacement mode shapes computed from Rayleigh-Ritz model.

Using this set of 15 trial shape functions, the mass and stiffness matrices of the system are formed by integrating with the distributed sectional properties shown in Figure 3.7. The first three modal frequencies thus obtained are 27.5 Hz, 86.9 Hz, and 306.2 Hz, which compare well with the experimentally observed values of 26.1 Hz, 87.3 Hz, and 302 Hz. When the translational and rotational inertia of the coil of the disturbance force are included in the Rayleigh-Ritz beam model, modal frequencies of 22.4 Hz, 76.0 Hz, and 218 Hz are found, compared to the experimentally observed values of 21.3 Hz, 80.5 Hz, and 216.2 Hz. The first five mode shapes are shown in Figure 3.9. Having confirmed the essential accuracy of the modeling, the model was subsequently adjusted by transforming to modal form and fixing the first four modal frequencies and damping ratios to the measured values.

The column of the forcing matrix for the piezoelectric actuator is, of course, proportional to the value assumed for d_{31}. From the discussion of measured bare piezoceramic characteristics in Section 3.1.1, it is clear that the appropriate choice is dependent on the expected strain levels; for this work, an intermediate value of -200 pm/V results in good agreement with the measured open loop transfer functions shown in Section 3.3.2 below.

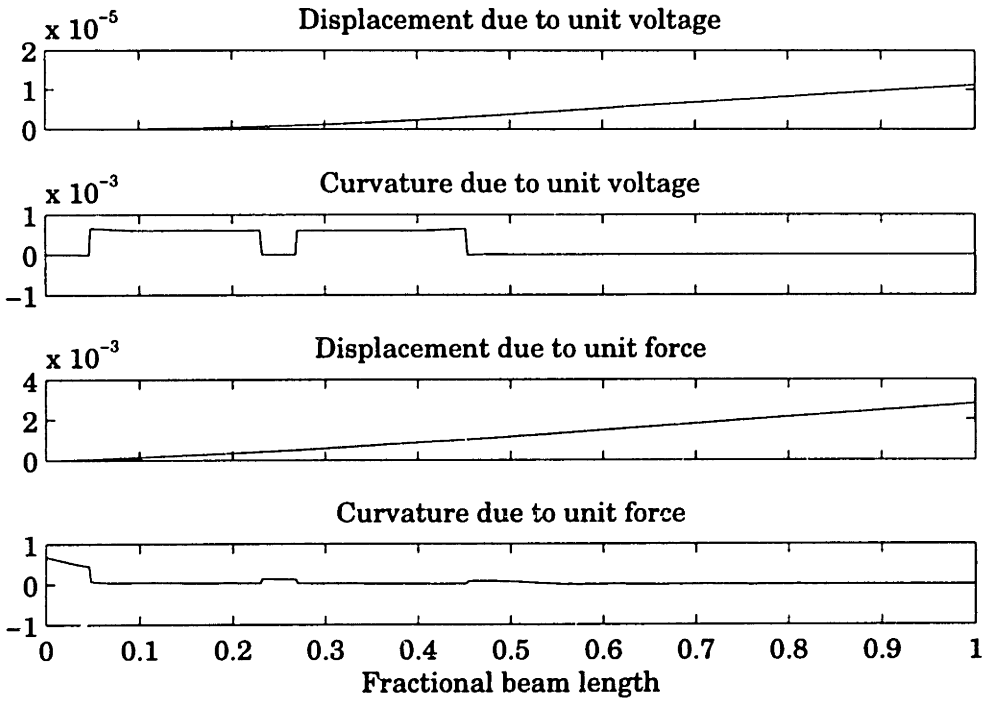

Fig. 3.10. Displacement and curvature shapes due to unit piezoelectric voltage and unit coil force.

The static displacements and curvatures for unit piezoelectric voltage and coil force inputs are shown in Figure 3.10. Comparing the curvature profiles suggests that relative share of strain energy in the beam and the package is very different in these two cases. At this point it is interesting to consider the value of the derated electromechanical coupling constant introduced in Chapter 2. Recall that $\tilde{K}^2$ is the material property K^2 (for electrical energy input, the ratio of the amount of that energy stored electrically to the amount transformed into mechanical energy) multiplied by that fraction of the total system strain energy which appears in the actuator. In the single mode system analysis, this quantity is unambiguous, since only one deformation pattern is permitted. For the real beam model, however, the fraction of strain energy in the actuator will depend on whether the shape assumed is that of a mode, the static response to an applied disturbance force, or the static response to an applied piezoelectric voltage. For these three deformation patterns, the fraction of the total strain energy which is stored in the piezoelectric elements is 16.4 %, 17.4 %, and 82.0 %, respectively. Since rate feedback is assumed, the quasistatic deformation will be dominated by the static response to the disturbance force, and around the first resonance, the

deformation pattern will be that of the first mode, so the piezoelectric elements share of strain energy will be approximately 17 %. Multiplying this by the electromechanical coupling constant for the piezoelectric material by itself (a K^2 value of 0.1345 based on the assumed values for modulus, piezoelectric constant, and dielectric constant) a value of $\tilde{K}^2$ of about 0.023 is obtained. This places the current system somewhere between the high and low values of derated electromechanical coupling constant used for plotting curves in Chapter 2; the effects of the non-capacitive load on amplifier dissipation should be noticeable, especially at low damping levels.

3.3.2 Open loop response: model and experiment

A comparison of the open loop transfer functions of the model (with frequencies and damping ratios corrected according to measurements) and the experimental setup is presented in Figures 3.11-3.16.

Having selected a suitable value of d_{31} and corrected the modal frequencies as described above, the model transfer functions show excellent agreement with the data. The most notable discrepancies are in the relative magnitudes of the first and second modes (which may be ascribed to mis-modeling of the details of package stiffness) and the magnitude of the coil force to piezoelectric charge

The other "sensor" quantity recorded was the current drawn (or supplied) by the piezoelectric ceramics in the actuator patches. Because the piezoelectric voltage/piezoelectric charge and coil force/beam displacement at coil location are energy duals, Maxwell's principle of reciprocal deflections requires that the cross transfer functions (piezoelectric voltage to beam displacement at coil location and coil force to piezoelectric charge) must be equal. This is an extension of the requirement that compliance matrices be symmetric as a consequence of the first law of thermodynamics. Comparing Figures 3.12 and 3.16, it is apparent that the measured transfer functions are quite close, aside from additional phase loss in the transfer function from piezoelectric voltage to beam displacement at coil location. Since both displacement responses to coil force excitation exhibit this same phase loss, it may be ascribed to the

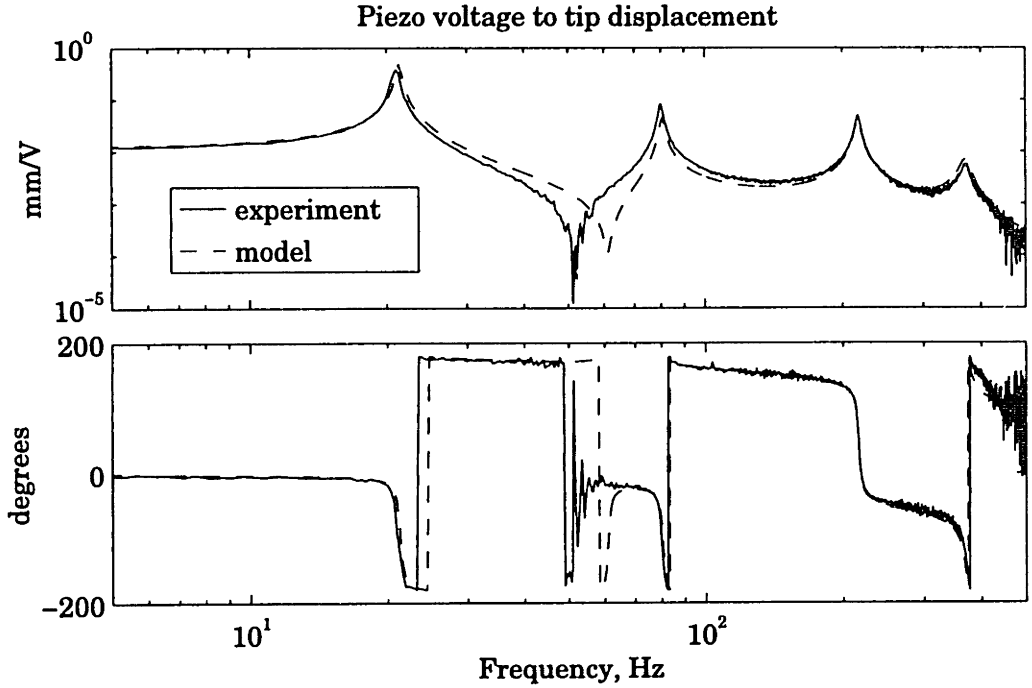

Fig. 3.11. Transfer function from piezoelectric voltage to tip displacement.

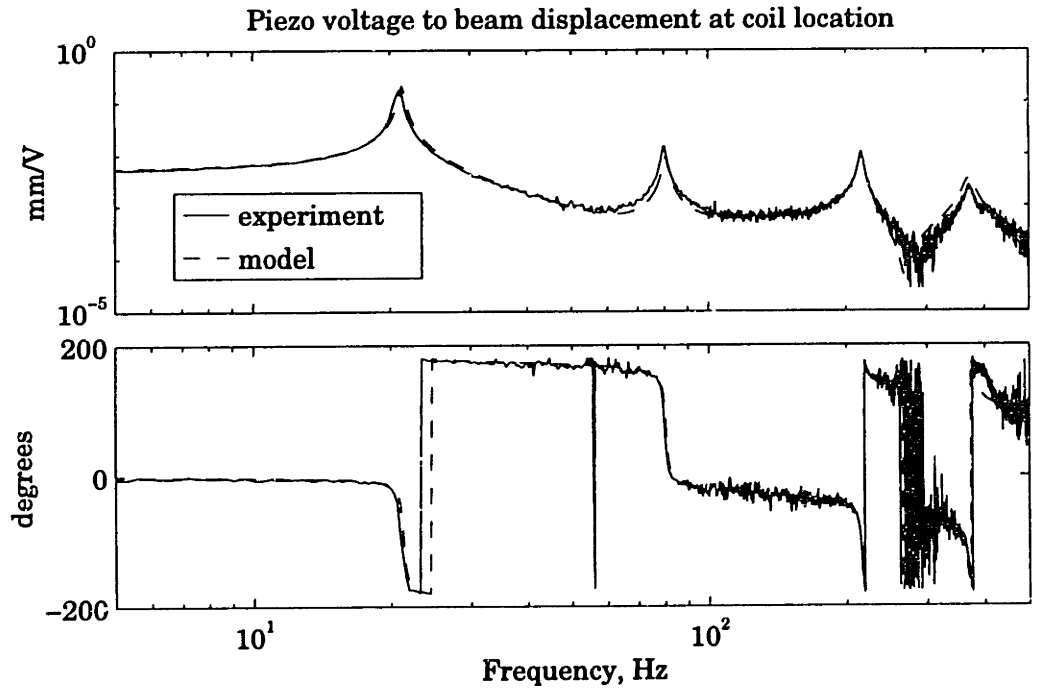

Fig. 3.12. Transfer function from piezoelectric voltage to beam displacement at coil location.

laser displacement sensors, justifying the modeling of the sensor dynamics just described.

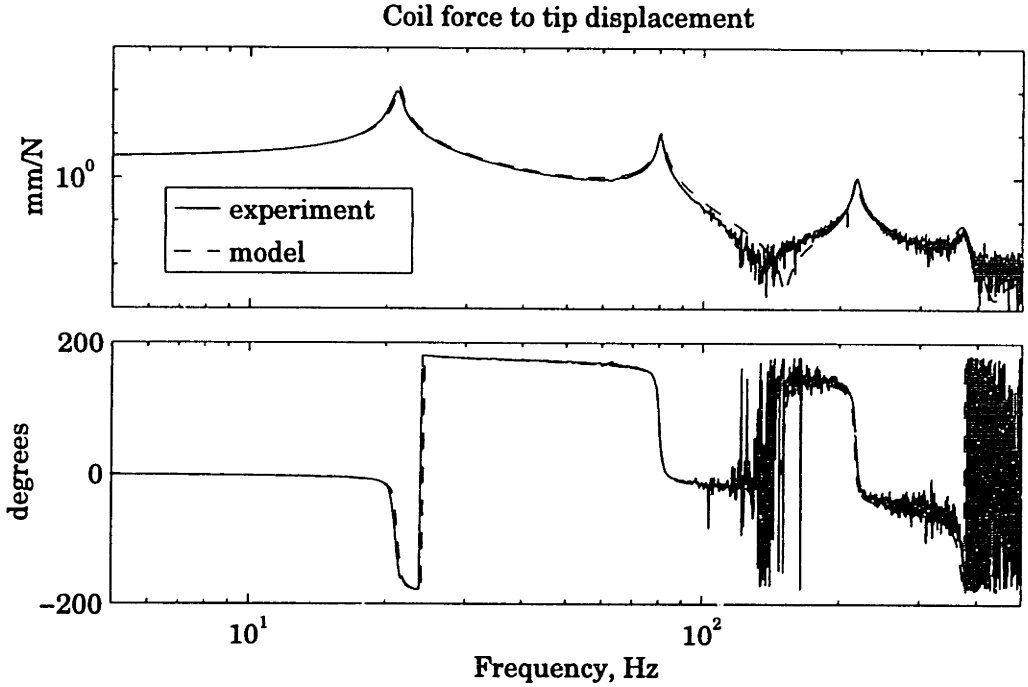

Fig. 3.13. Transfer function from coil force to tip displacement.

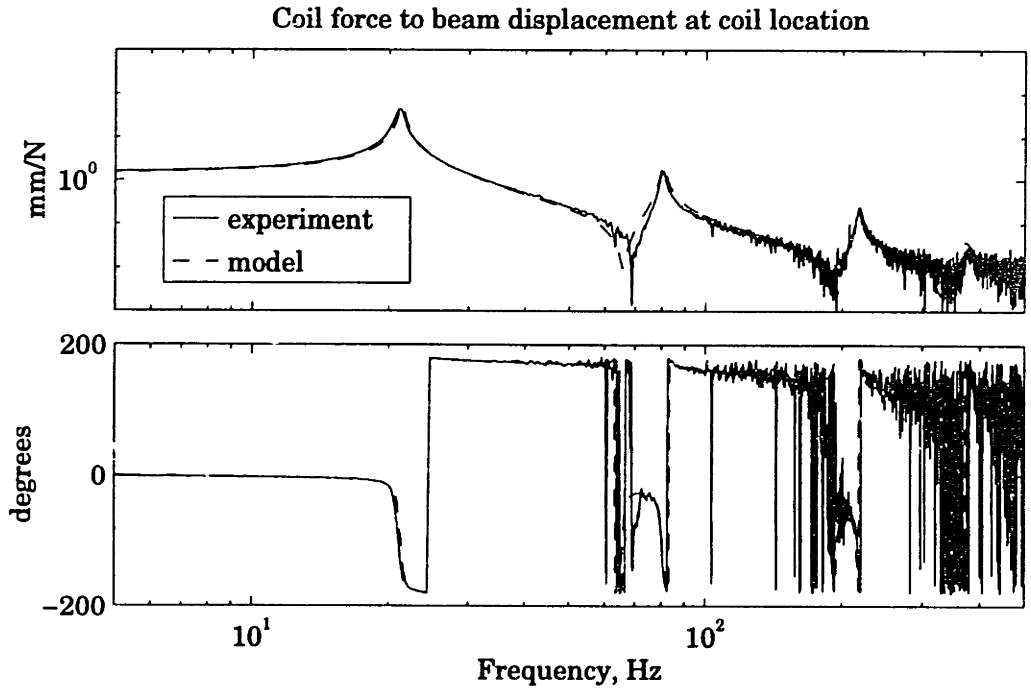

Fig. 3.14. Transfer function from coil force to beam displacement at coil location.

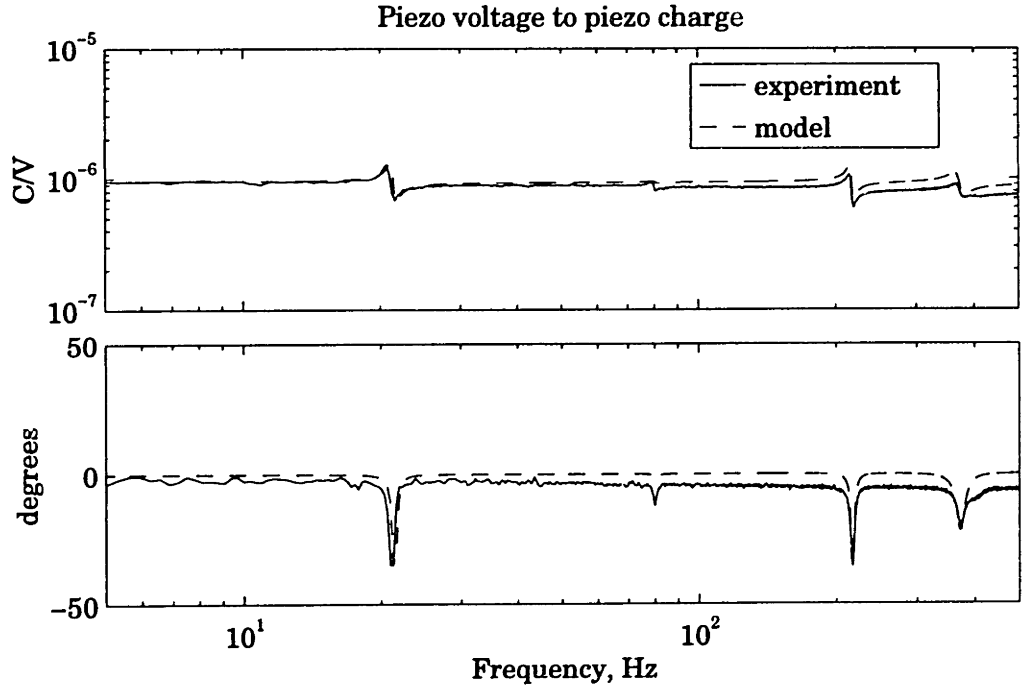

Fig. 3.15. Transfer function from piezoelectric voltage to piezoelectric charge.

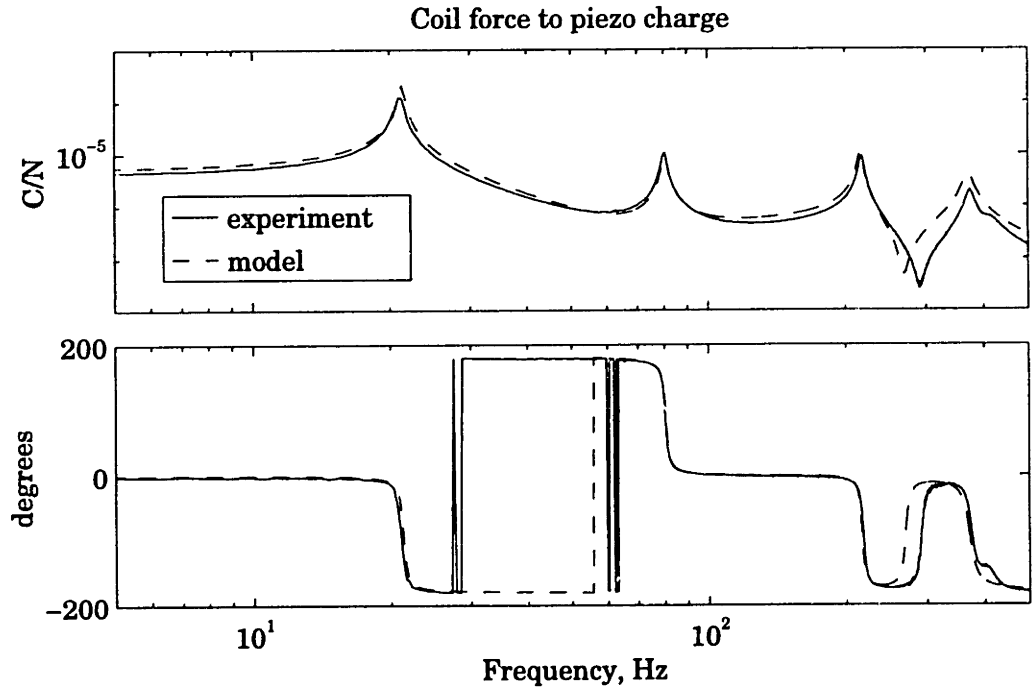

Fig. 3.16. Transfer function from coil force to piezoelectric charge.

3.3.3 Compensator

In order to demonstrate the closed-loop power characteristics described in the analysis of Chapter 2, a controller was designed to implement active

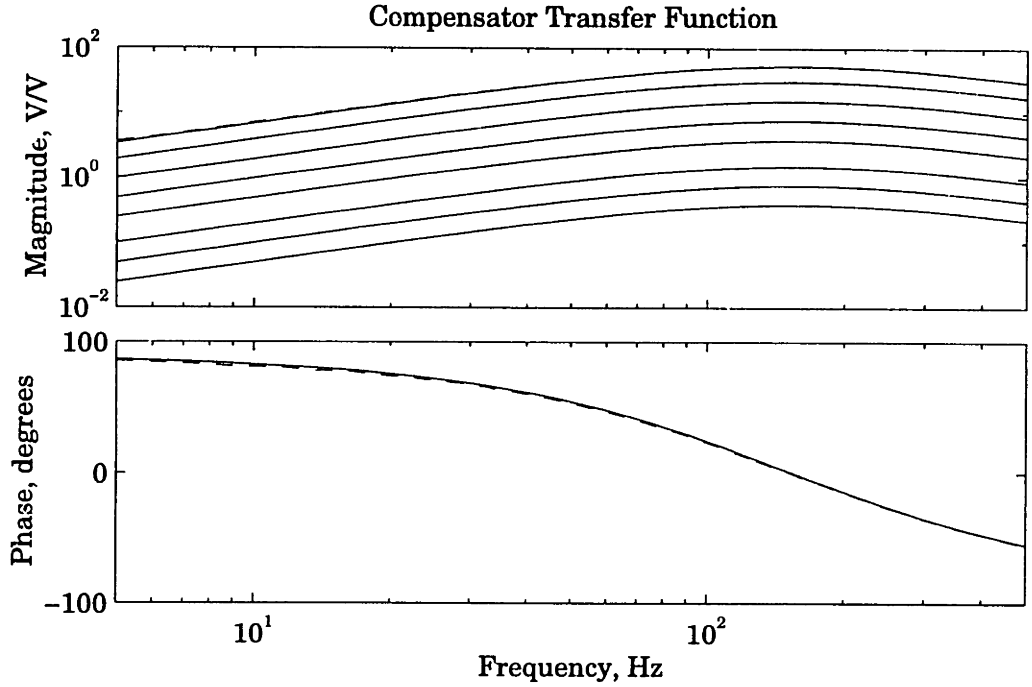

Fig. 3.17. Model compensator transfer function at the seven closed loop gains compared with measured compensator at maximum gain.

damping in the first mode. To achieve this, the signal from the tip displacement sensor was fed through an analog circuit with a transfer function consisting of a zero at the origin, two real poles at approximately 155 Hz, and a variable gain. The output of this circuit was then sent to the amplifiers driving the piezoelectric actuators. The compensator transfer function is plotted in Figure 3.17.

Referring to the transfer function in Figure 3.11, it is clear that pure negative rate feedback would damp the first and second modes, but would destabilize the third mode due to the lack of a zero between the second and third modes. The presence of the two real compensator poles in this frequency range, however, causes the phase to shift so that the effect of feedback on the third mode is stabilizing. The absence of a zero between the third and fourth modes as well would imply a destabilization of the latter mode, but roll-off in compensator magnitude will tend to gain stabilize this (and higher) modes. The effect of the compensator pole placement is illustrated by the loop transfer function of Figure 3.18. Substantial loop gain is achieved at the first three modes, but at this maximum compensator gain, instability is immanent at the gain and phase crossover points near 100 Hz and at the fourth mode.

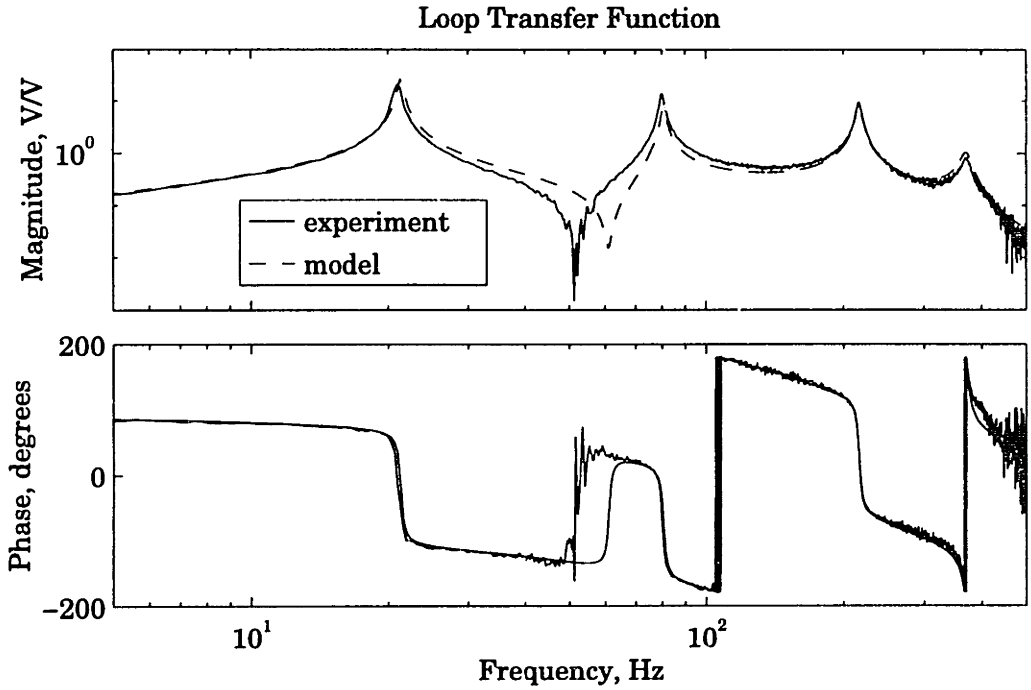

Fig. 3.18. Experimental and model loop transfer function at maximum compensator gain.

3.4 Closed Loop Frequency Domain Behavior

3.4.1 Disturbance rejection performance

Closing the loop with the plant and seven compensator gains described in the preceding sections yielded increased damping in the first three modes, as intended. Modal frequencies and damping ratios were measured by exciting the beam with a sinusoidal disturbance force near resonance, observing the resulting ring-down when the disturbance was removed, and fitting exponentially decaying sinusoid. The resulting values for the first mode are compared with predicted values in Table 3.2, in which the gain of the compensator is represented by the relative amplification of the final gain stage (actually the value of a resistor in kΩ.) No predicted values are given for the open loop, since the model was adjusted to agree with those measurements as described in Section 3.3.1. Ringdown tests were performed for the second and third modes up to the penultimate gain level; at the highest gain level, a combination of greatly amplified sensor noise, the proximity of the second mode to instability, and the low amplitude of the

Table 3.2 Measured first modal frequencies and damping ratios

	Measured		Predicted		Damping
Gain	Freq, Hz	ζ, %	Freq, Hz	ζ_p, %	overprediction, ζ_p/ζ
0.0	21.28	1.21	(21.28)	(1.21)	(1.00)
0.05	21.28	1.24	21.30	1.43	1.15
0.1	21.31	1.48	21.32	1.65	1.11
0.2	21.35	1.82	21.35	2.09	1.15
0.5	21.44	2.74	21.46	3.43	1.25
1.0	21.58	4.28	21.65	5.68	1.33
2.0	21.95	7.70	22.05	10.25	1.33
4.0	23.10	15.29	23.04	19.73	1.29
7.0	26.35	26.37	25.27	35.08	1.33

third mode made ringdown tests of the second and third mode impossible. Over the range of gain levels for which this data was gathered, the second mode frequency and damping increased from 80.54 Hz and 1.13 % to 87.89 Hz and 3.01%, while the third mode went from 216.22 Hz and 0.98% to 211.40 Hz and 5.94%.

The overprediction of damping may be explained by reference to the transfer function from piezoelectric voltage to tip displacement in Figure 3.11. The failure of the model to correctly represent the amplitude of the second mode has caused the frequency of the zero between the first and second modes to be overestimated. This means that, under rate feedback, the root locus trajectory of the first mode in the model will arc further into the left half plane before turning to meet the zero in the high gain limit; this translates into greater predicted damping for a given level of gain.

The transfer functions of disturbance force to displacement sensors for three gain levels 0.05 (nearly open loop), 2, and 7 are shown in Figures 3.19 and 3.20, along with model predictions from at the same compensator gains.

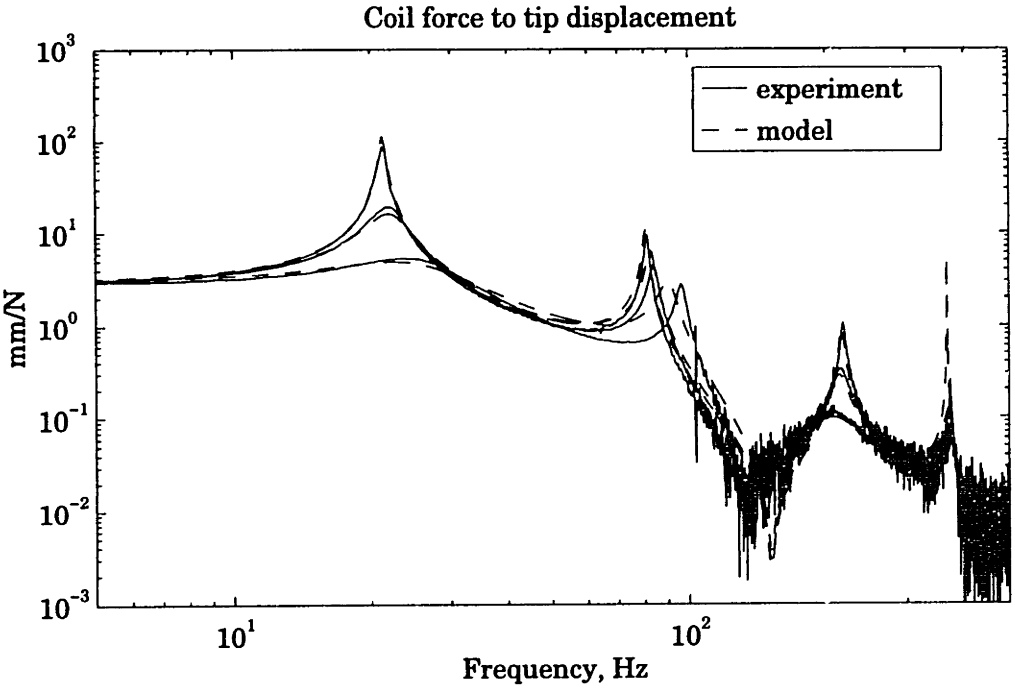

Fig. 3.19. Closed loop transfer function from coil force to tip displacement.

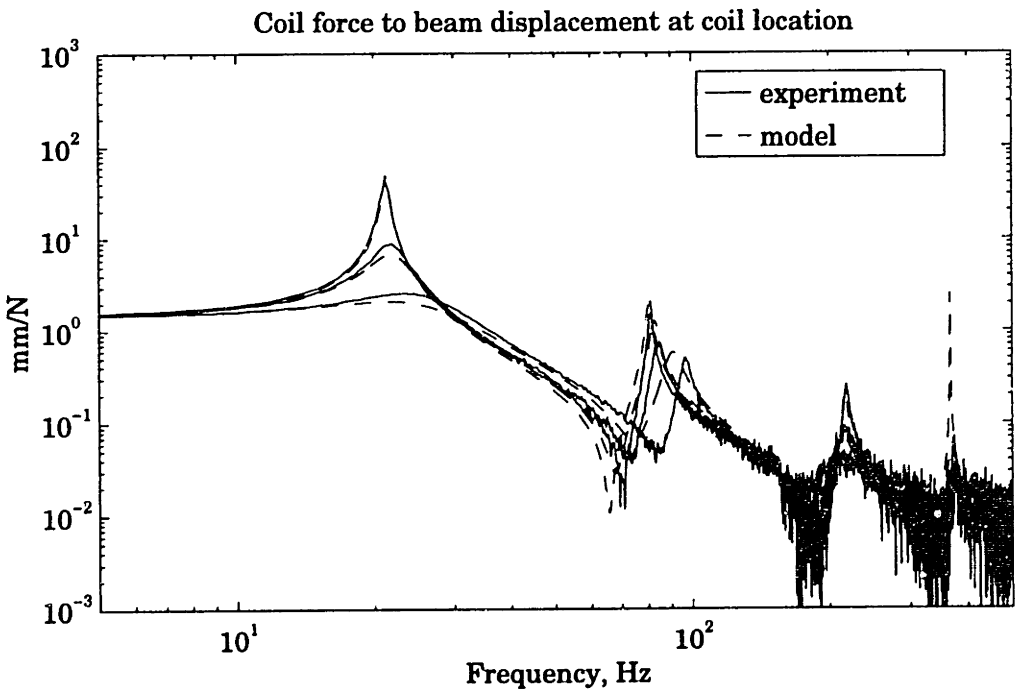

Fig. 3.20. Closed loop transfer function from coil force to beam displacement at coil location.

The comparison of model and experimental responses in these figures shows a general agreement in terms of trends. All modes are damped, and the frequency of the first and second modes increases with increasing gain while that of the third mode decreases. Quantitatively, however, the model and

data diverge with increasing gain. The reduction in tip response at the first mode is predicted to be 27.3 dB, while the measured value is 22.6 dB. Similarly, the predicted reduction in total RMS tip response is 12.7 dB over the frequency range shown, compared to a measured reduction of 11.8 dB. This discrepancy may be a consequence of the nonlinearity in the piezoelectric response: for a disturbance of fixed magnitude, increasing modal damping tends to decrease the strain levels in the actuators, which would result in a lower effective d_{31} constant than was assumed based on the open loop response. Another reason for the discrepancy between model and data is the mis-modeling of the frequency of the zero between the first and second modes in the transfer function from piezoelectric voltage to tip displacement; since the first pole and this zero are farther apart in the model than in the data, the closed loop pole trajectory will travel further into the left half plane when the loop is closed in the model, leading to the overprediction of damping noted in Table 3.2 and in the transfer functions of Figures 3.19 and 3.20.

3.4.2 Apparent load admittance

The apparent admittance of the load driven by the power amplifier was also measured. Note that this is not a transfer function in the ordinary sense of the term: neither the voltage nor the current can be considered an independent variable. In the model, the admittance is obtained as in the single DOF analysis in Section 2.2.1 by dividing the transfer function of disturbance to current by that of disturbance to voltage. (Experimentally, the relation between the current and voltage measurements is found like that between any two signal channels.) The results for gains of 0.05, 0.2, 2.0, and 7.0 (corresponding to experimentally measured damping ratios of 1.24 %, 1.82 %, 7.70 %, and 26.37 %, respectively)are shown in Figure 3.21.

This figure clearly shows the expected negative resistor behavior predicted for low frequencies and low values of active damping, as indicated by the constant magnitude and the 180° phase. As the gain is increased, the size of the apparent negative resistor increases (admittance drops) and the transition to capacitive behavior occurs at lower and lower frequencies. As was the case in the single degree of freedom results shown in Figure 2.4, no drastic change in the load admittance occurs the frequency of the first mode (21-25 Hz in the experiment); unlike the simple model, however, the presence

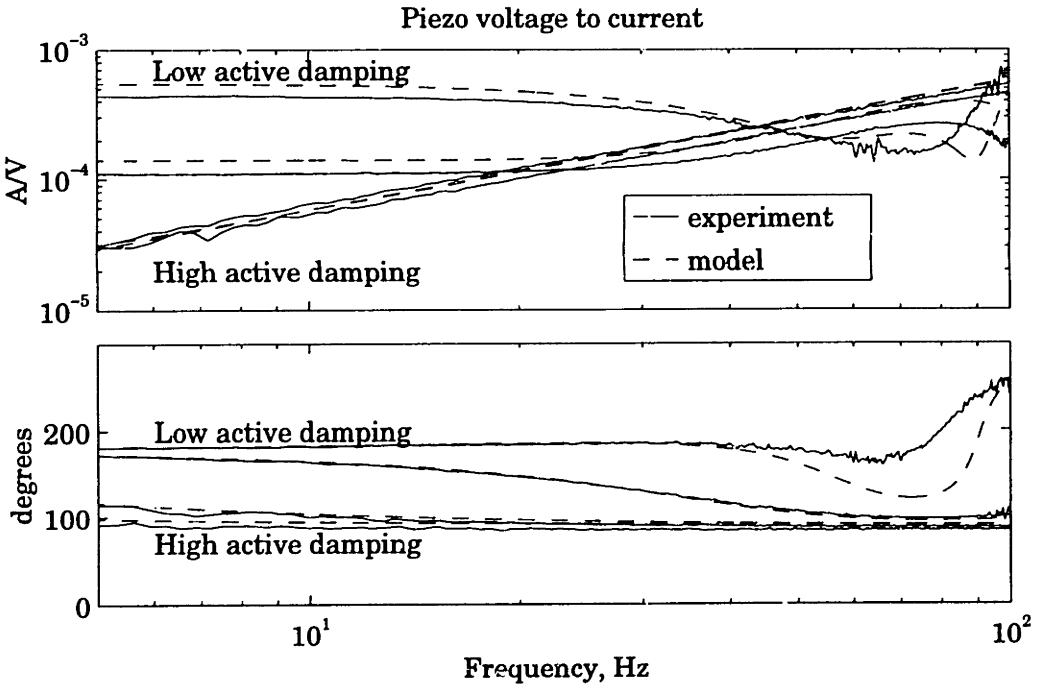

Fig. 3.21. Apparent closed loop load admittance for various gains.

of higher frequency dynamics makes more complicated the interpretation of the apparent load admittance above the first mode in terms of simple electrical components. In general, though, it may be stated that if increasing the gain of a controller reduces the motion of the structure, the contribution of the direct piezoelectric effect to the current flow will be reduced, and the load on the amplifier will increasingly resemble that of a capacitor alone.

3.5 Current Response and Dissipation with Sinusoidal Excitation

The successful experimental verification of the negative resistive behavior predicted by the analytical model of Chapter 2 suggests that predicted trends in power dissipation may also be validated by experiment. For problems in which system response is dominated by a single, lightly damped mode or a narrow-band disturbance, the response to sinusoidal excitation may provide useful power information, as well as allowing for a clear comparison of experimental and predicted results. The single degree of freedom model analyzed in Chapter 2 and the beam model presented above, however, both omit aspects of the problem which may be of significance. In particular, the

nonlinear dielectric constant indicated in Figure 3.2 shows that increasing the applied electric field causes both an increase in magnitude and a loss of phase. Since current is the derivative of charge, the increase in magnitude of the dielectric constant means that larger control voltages will result in load current amplitudes greater than would be expected from a linear system. Rewriting the modeled instantaneous amplifier dissipation of Eq. 2.23 in terms of the measured quantities (instead of nondimensional ones) gives

$$P_{amp}(t) = -I_{LOAD}(t)V_{OUT}(t) + |I_{LOAD}|170\,\mathrm{V} \qquad (3.2)$$

It is clear that a larger load current will increase the contribution of the second term to amplifier dissipation. The loss of phase of the dielectric constant at higher voltage levels, however, will be manifested as a reduction of the relative phase between current and voltage. This will tend to make the average value of the first term more negative, representing more power transfer from the amplifier to the actuators and resulting in lower amplifier dissipation. In addition, the derivation of the amplifier dissipation expression in Eq. 3.2 assumed that the power supply currents were due only to the load current; the effects of any quiescent amplifier currents will thus not be reflected in the model.

These issues will be examined by first evaluating the open loop power flow and dissipation in driving an unconstrained package and comparing this behavior with that of the actuators when bonded to the beam (again open loop) to investigate the dependence of the nonlinearity on strain state. Finally, measurements of closed loop power dissipation with the actuators bonded to the beam will be presented and evaluated in the light of the behavior expected from the analytical results of Chapter 2 and the nonidealities just mentioned.

3.5.1 Open loop response of the unconstrained package

Measurements of current and power were made on the unconstrained package under sinusoidal excitation with frequencies ranging from 0.5 Hz to 2 KHz and voltages ranging from 10 V to 160 V. Since applications such as the active wing mentioned previously [Lin, Crawley, and Heeg, 1995] will generally require a wide range of voltages but only a moderate frequency range, current and power responses to sinusoidal excitation at 20 Hz and two voltage levels are presented here as typical results. Figure 3.22 shows plots

of the excitation voltage and load and supply current responses. The top two plots show the applied voltage sine waves V_{OUT} as a function of time for one cycle; the plots on the left are for a 20 V excitation at 20 Hz, while those on the right are for a 160 V excitation. The bottom two plots of Figure 3.22 present the corresponding load current (I_{LOAD}) and positive and negative supply current (I_{sp}, I_{sm}) time histories for the two excitations. In the low voltage case the load current (measured by sensing resistor R_{il} of Figure 3.3) is a sinusoid (amplitude 1.1 mA) which leads the voltage by 87° (i.e., a cosine plus a lag of only 3°) as befits the largely capacitive nature of the free piezoelectric elements. The currents from the supplies, as measured by R_{isp} and R_{ism}, demonstrate the sinking and sourcing of current by the output transistors Q1 and Q2 as described in Section 2.1.2; i.e., the positive supply sources current through Q1 when the load current is positive, and the negative supply sinks current through Q2 when the load current is negative. An excess current of approximately 1 mA is apparent; this is the sum of the non-zero off-current of the transistors and the current from the amplification stages, and is not reflected in the model of amplifier dissipation represented by Eq. 2.23 or 3.2.

The load current response at 160 V reaches a maximum of 17 mA, nearly twice the 8.8 mA which would be expected from the eight-fold increase in voltage. Furthermore, the current wave form is distorted, with peaks occurring well after the voltage crossovers at t=0 and t=0.025. The deviation from a linear response may be due to domain boundary movement which can occur within piezoelectric crystallites at high field levels [Zhang and Rogers, 1993]; the energy required for this movement would be reflected in the electrical variables as an increase in the current flow.

Given the voltage and current time histories, the amplifier dissipation may be computed from Eq. 3.1. In Figure 3.23 the response of the modeled amplifier (represented by Eq. 3.2) with a linear piezoelectric load is presented in the top two plots for the two voltage levels, while the actual measured amplifier and piezoelectric power dissipation are shown in the bottom two plots. For the low voltage case, the difference between modeled and measured

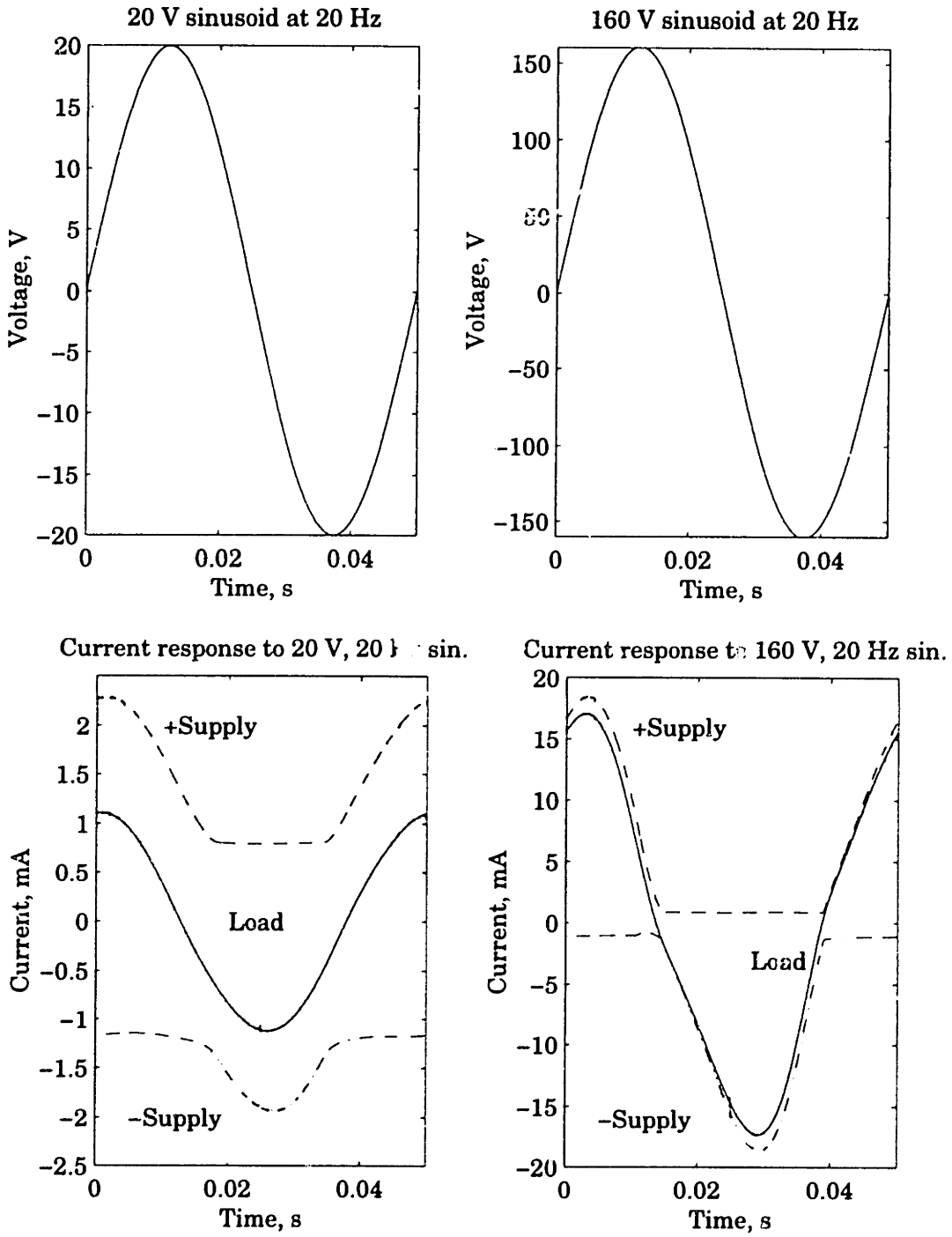

Fig. 3.22. Voltage (V_{OUT}), load current (I_{LOAD}), and positive and negative supply current (I_{sp}, I_{sn}) for small and large sinusoidal excitation of the free package.

piezoelectric power flow is quite small. For the amplifier dissipation, the quiescent current of slightly more than 1 mA, delivered across a total supply potential of 340 V, results in an additional 350 mW of measured amplifier

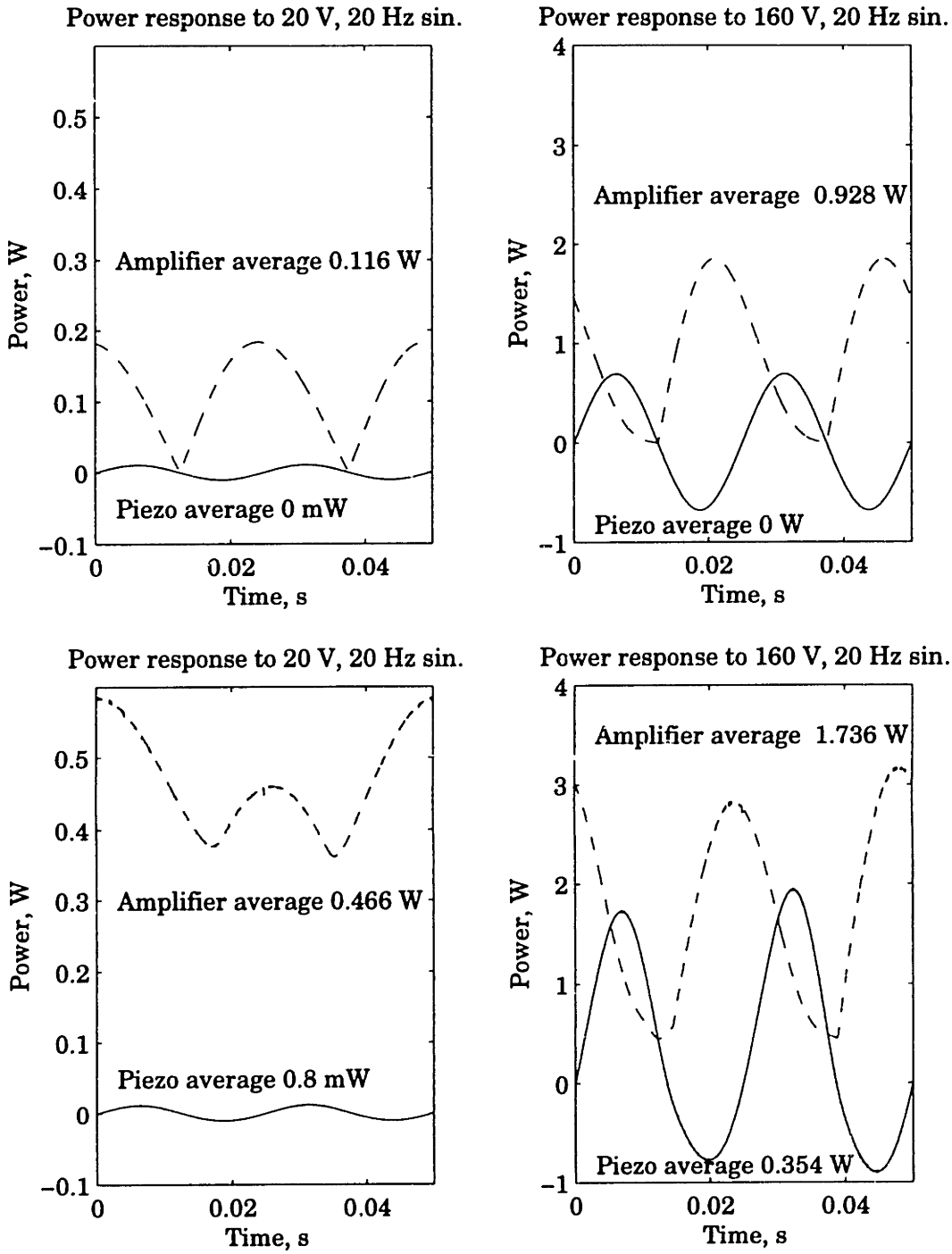

Fig. 3.23. A comparison of modeled (top) and measured (bottom) piezoelectric and amplifier power dissipation for small and large sinusoidal voltage applied to the free package.

dissipation above the 116 mW predicted by the model. (The difference in the height of the peaks of the power dissipation is due to an asymmetry in the construction of the PA41; since Q2 is implemented as a compound device, it

has a greater off-current than Q1, which Q1 must supply when the load current is positive, leading to greater dissipation.)

When the modeled and measured results for the high voltage excitation are compared, the impact of the nonlinear current response on power flow is significant. The predicted model response in the upper right plot again shows no average loss in the piezoelectric element, and an average amplifier dissipation of 928 mW. This is eight times that of the low voltage case, reflecting the predicted eight-fold increase in load current amplitude and corresponding increase in the second term on the right hand side of Eq. 3.2. (The first term, the power flow to the piezoelectric element, averages to zero.) The measured power flows of the lower right plot show several differences when compared to the model predictions. The previously discussed quiescent amplifier power dissipation of 350 mW is again present; subtracting this from the measured amplifier dissipation yields a "corrected" value of 1.386 W. This is greater than the model prediction of 928 mW because of the nonlinear increase in current amplitude. The size of the corrected dissipation is not purely a function of the load current amplitude, however; the distortion of the load current wave form distortion has increased the effective resistive component of the load. This phase nonlinearity results in a substantial amount of power delivered to the piezoelectric elements (354 mW); if the magnitude nonlinearity alone were present, this power would be dissipated in the amplifier.

The nonlinear current response of the piezoelectric material as measured in sinusoidal tests over a range of frequencies and voltage levels may be represented by presenting calculated values of the magnitude and phase of the effective material dielectric constant. These are shown in Figure 3.24. The actual voltage amplitudes (10 V, 20 V, 50 V, 100 V, 150 V, 160 V) are labeled in terms of the fraction of the AC depoling field, taken to be 0.7 MV/m for this material, or 178 V for a thickness of 0.254 mm.

Comparing Figure 3.24 with the broadband random excitation results for the piezoceramic presented in Figure 3.2, the substantial increase in magnitude and loss of phase with increased electric field is again apparent, though far more pronounced than in the previous tests which were conducted at relatively low fractions (2% and 10%) of the AC depoling field.

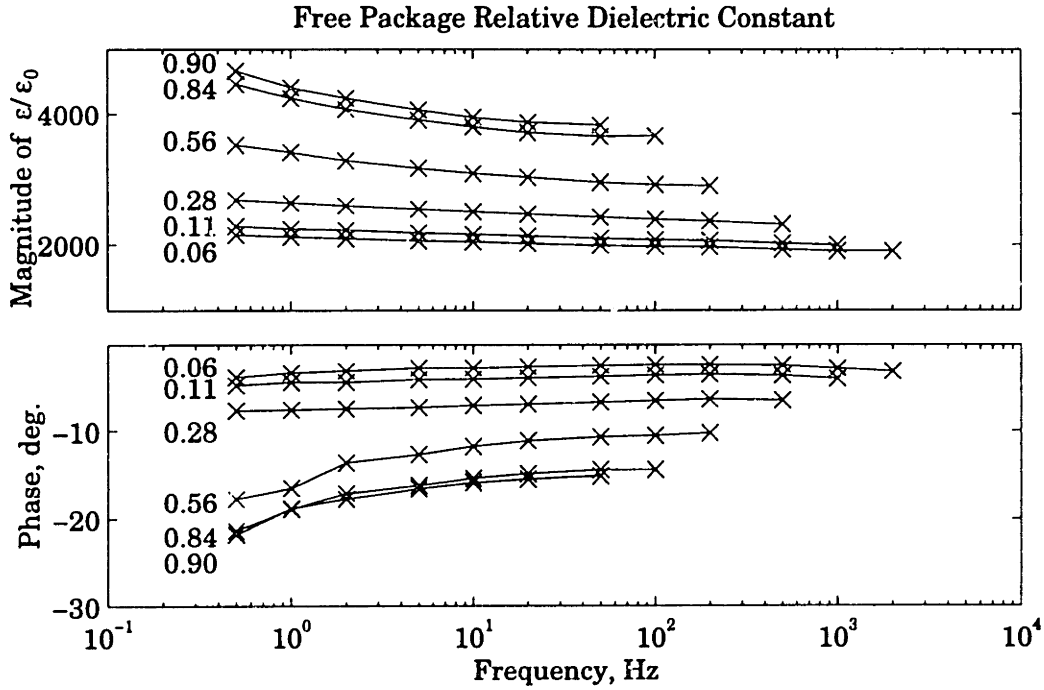

Fig. 3.24. Effective dielectric constant for unconstrained actuator package for different electric field amplitudes (as a fraction of AC depoling field) and frequencies.

In summary, the amplifier dissipation predicted by the idealized amplifier model represented in Eq. 3.2 must be corrected to account for the dissipation due to the quiescent current drawn by the amplifier from the power supplies. With this correction, the power dissipation predicted by the model amplifier driving a linear, lossless piezoelectric load is in good agreement with the measured results for low electric field levels. For large field levels, the nonlinear, complex dielectric constant of the piezoelectric is manifested in the load current response as an increase in amplitude and a loss of phase. This results in both in elevated amplifier power dissipation (compared to model predictions) and a significant power dissipation in the piezoelectric elements themselves.

3.5.2 Open loop current response of the beam-mounted package

The nonlinearity of the piezoelectric effect (the d_{31} constant) is known to be a function of the strain state of the piezoceramic [Crawley and Anderson, 1990]. It is of interest to try to determine whether the observed nonlinearity of the current response (i.e., the dielectric constant) is also dependent on the strain state, or whether it is a function of electric field strength alone. The

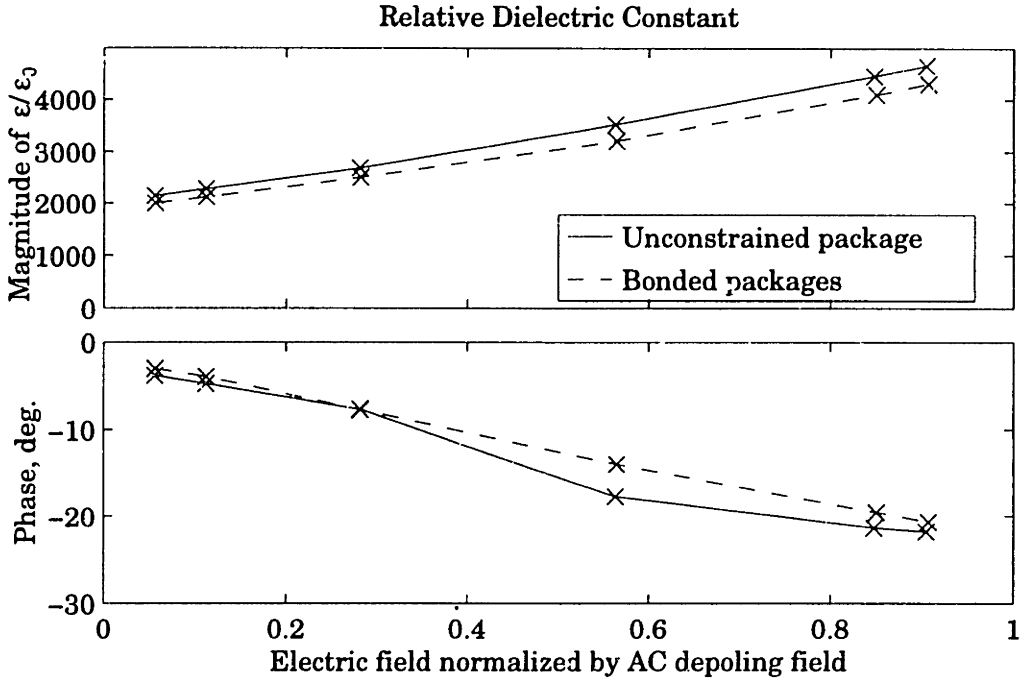

Fig. 3.25. Electric field dependence of the dielectric constant for the unconstrained and bonded at 0.5 Hz.

current response of the unconstrained package described in the previous section may be compared with that of the packages bonded to the graphite epoxy beam. The behavior was measured in response to applied sinusoidal voltages of various amplitudes at 0.5 Hz; the low frequency was chosen to eliminate the obscuring effects of operation near a resonance of the beam. The resulting current responses are plotted in the form of computed dielectric constants against electric field strength in Figure 3.25.

Concurrent strain measurements show that, at all applied fields, the strain present at the surface of the packages bonded to the graphite/epoxy beam was 59% of the strain achieved in the free package for the same applied field. Using the location of the piezoelectric elements within the packages on the beam and assuming Bernoulli-Euler bending, the average strain in the piezoceramics is 73% of the surface strain, so the average strain in the bonded piezoceramics is only 43% of the strain in the free package for the same applied electric field. Despite this considerable constraint, the nonlinearity of the current response as reflected in magnitude of the computed dielectric constant is only slightly affected, being reduced by some 7%, some of which could be due to variation between the response of the two bonded packages. This apparent insensitivity to mechanical constraint

indicates that the nonlinearity in current response is largely independent of the strain state of the piezoelectric elements.

3.5.3 Closed loop power dissipation with beam-mounted package

In this section, the power flow in the closed loop system will be examined when the beam is excited by a sinusoidal disturbance force at the resonant frequency of the first mode under conditions of varying active damping. Knowledge of the commanded disturbance from the magnetic coil and the displacement of the point of application of that force can be combined to yield the power input to the system from the disturbance. The measured piezoelectric actuator voltage and current are used to compute the power flow between the amplifiers and the electromechanical system, and the added knowledge of the amplifier supply currents allows computation of the quantity of ultimate interest, the power dissipation in the amplifiers. These various components of the power flow will be presented with a discussion of their consistence with the behavior predicted by the analytical model, with special attention to the implications of the previously discussed nonidealities of both the piezoelectric elements and the amplifiers. Note that in this section the two packages bonded on opposite sides of the beam and actuated in bending are treated as a single actuator, and the power dissipation in the two driving amplifiers is similarly combined.

The disturbance applied was a sinusoidal force with a frequency adjusted to match the resonant frequency at each gain level. A low disturbance amplitude of 52.2 mN was tried at all gain levels, and a high disturbance amplitude of 315 mN was also used at the three highest gain levels. The resulting power input to the system is shown in Figure 3.26 for both the model and experiment.

The overall agreement of these curves is good. The decline in input power with increasing gain for a constant disturbance force level is explained by the noting that the velocity response of the beam at the point of application of the disturbance is inversely proportional to the damping; the product of force and velocity is therefor reduced as the control gain and attendant active damping are increased. If not for the presence of approximately 1.2% of passive damping, the power input would increase without limit as the gain is reduced.

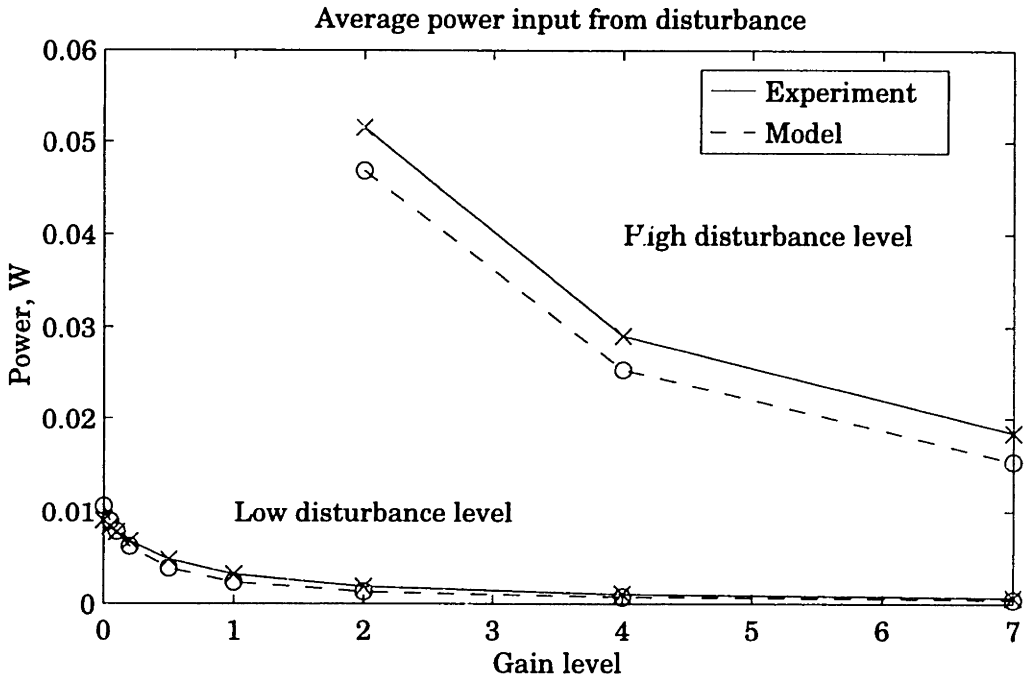

Fig. 3.26. Power input from the disturbance force to the controlled system as a function of control gain for two disturbance levels.

The power input from the disturbance source must be removed by either the passive damping or the effect of the control system. Figure 3.27 compares the power flow from the controlled structure to the amplifiers for the model and the experiment. The model predicts a power flow from the electromechanical system to the amplifiers that at first rises with gain, then falls, but is always positive. At low gain levels, the component of damping due to the control system is small compared to the passive damping of 1.2 %; when the gain is zero, the voltage applied to the actuators is zero and no power is removed from the electromechanical system by the amplifiers. As the gain is increased, the component of damping due to the control system increases, resulting in a rising amount of power removed by the amplifiers. As the gain is increased still further, the active damping exceeds the passive damping and comes to dominate the total damping. At this point, the control system accounts for the bulk of the power removed; since the overall power input from the disturbance is decreasing (Figure 3.26), the power removed by the amplifiers also decreases. This can be observed in the model predictions for both high and low disturbance levels. It is interesting to note that a control algorithm formulated simply to maximize the power removed from the system by the actuator would thus result in very lightly damped closed loop system, suggesting that a careful statement of the performance objective

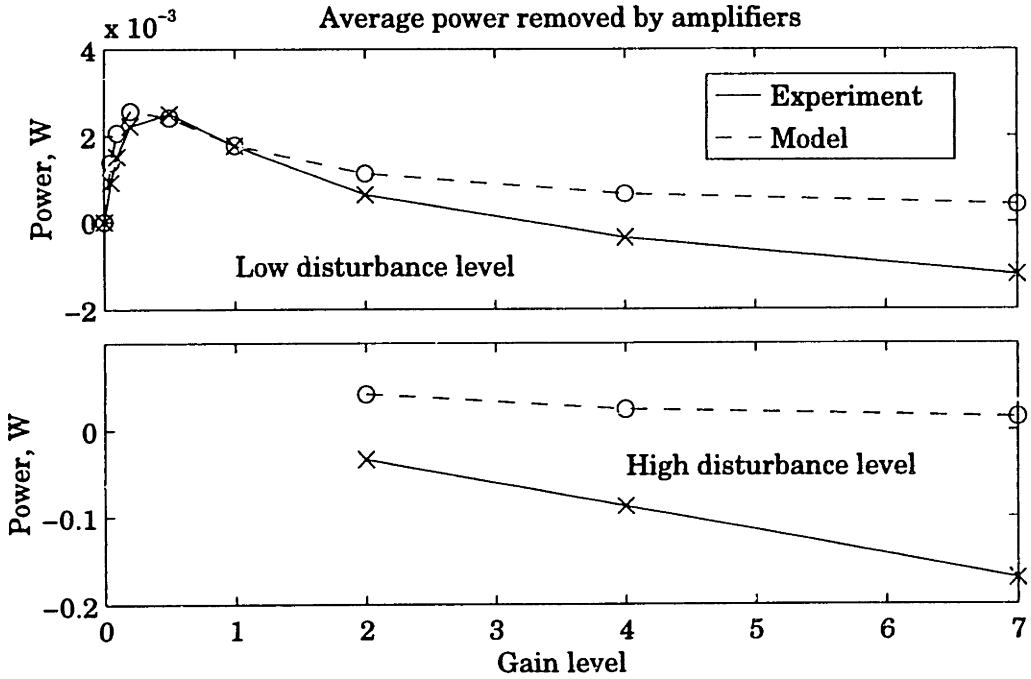

Fig. 3.27. Power flow from the controlled structure to the amplifiers as a function of control gain for two disturbance levels.

must take precedence over simplistic goals such as simply maximizing power flow.

At low gain levels, the experimental results are consistent with the model predictions, but at high gain levels, there is a reversal in the direction of power flow between structure and amplifiers. This is due to the nonlinear dielectric constant discussed in Section 3.5.1. In the presence of passive damping, the control voltage amplitude response to a disturbance of constant magnitude increases with active damping, as indicated in Eq. 2.36. Thus as the gain is increased in this case, the electric field level in the piezoelectric elements also increases, resulting in a nonlinear increase in load current amplitude and a loss of phase. The result is power dissipation in the piezoelectric elements which is supplied by the amplifiers and is far in excess of the mechanical power to be removed by the active damping. Since the nonlinearity is a function of electric field strength, this effect is especially noticeable at the high disturbance level.

Figure 3.28 shows predicted and measured amplifier power dissipation. From the scale of the power axis, it is apparent that the few milliwatts or tens of milliwatts of power removed through active damping are not a

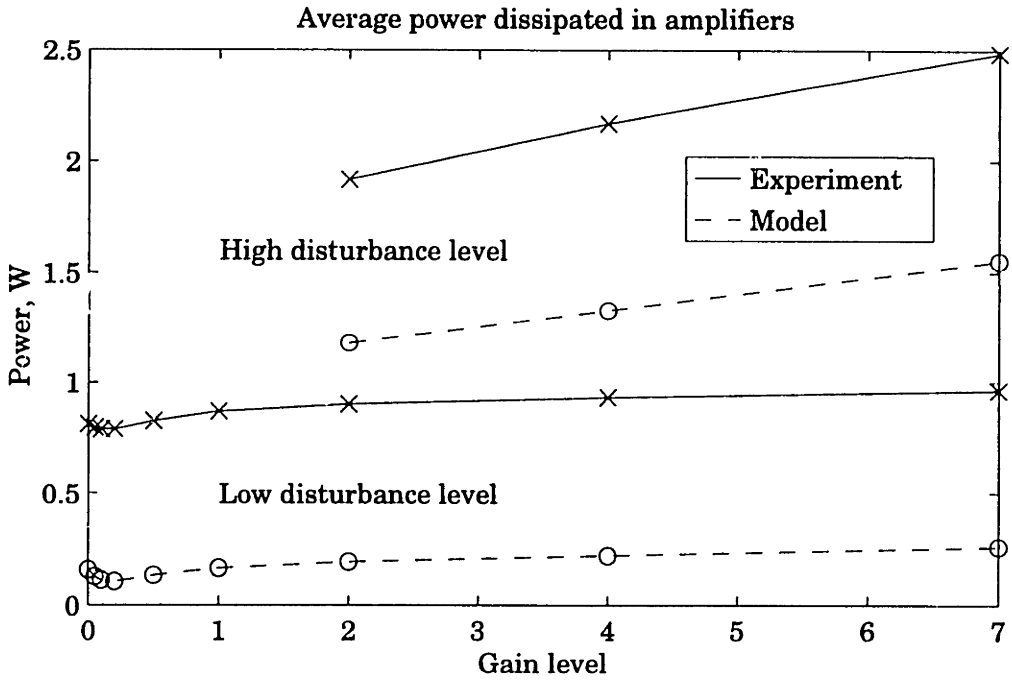

Fig. 3.28. Amplifier power dissipation as a function of control gain for two disturbance levels.

significant contribution to the amplifier power dissipation. For large gain levels, the dissipation predicted by the model is principally due to the effects of current flow to and from the power supplies associated with charging and discharging the inherent piezoelectric capacitance. At small gain levels, another component is important. Even though the voltage applied to the actuators is small (zero for zero gain), there is current flow due to the direct piezoelectric effect, i.e., charge caused by mechanical deformation. This current flow is drawn from the high voltage rails, resulting in dissipation in the amplifier even though no average power is being removed from the structure.

The difference between the experimental results and the model predictions of Figure 3.28 may be explained in terms of the nonidealities introduced in previous sections. The quiescent power dissipation of the amplifiers is apparent in the gap of approximately 700 mW (350 mW per amplifier) between the experiment and model response to the low disturbance level. At the high disturbance level with its associated higher field strengths, the gap between experiment and model is still greater; although the nonlinear phase loss in the piezoceramic current response tends to result in power flowing from the amplifiers to the actuator as shown in Figure 3.27,

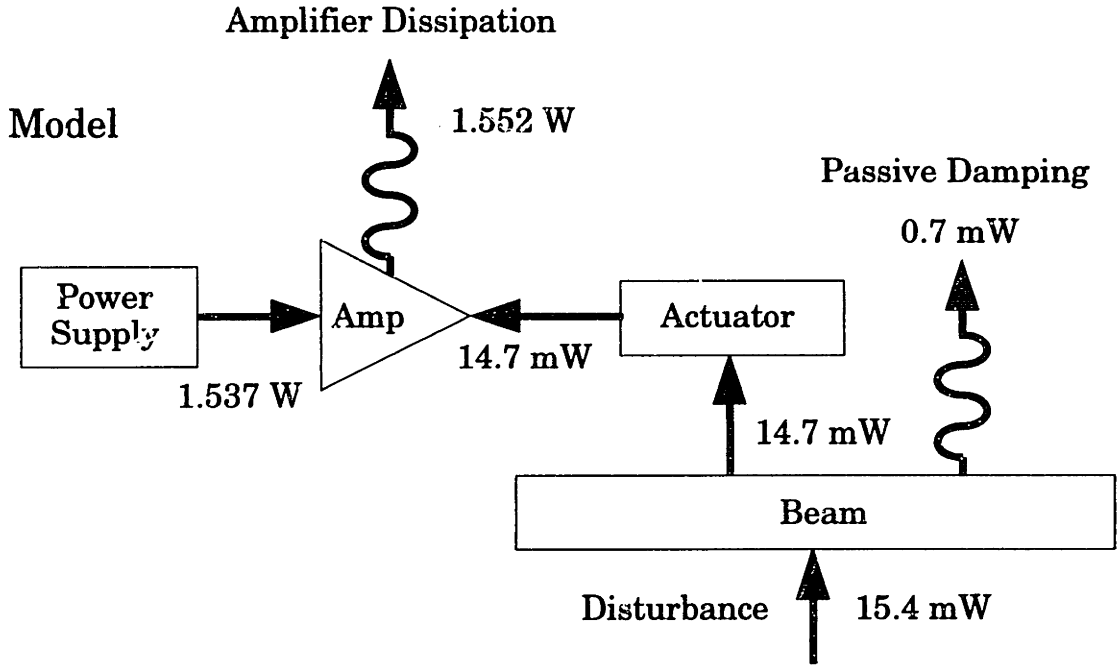

Fig. 3.29. Predicted power flow and dissipation summary for high gain, high disturbance case.

the relatively small magnitude of this power flow is insufficient to counter the effect of increased power drawn from the +/- 170 V supplies due to the nonlinear increase in load current magnitude.

For an overall numerical comparison, Figures 3.29 and 3.30 present a schematic summary of the various components of power flow and dissipation in the model and experiment for the case of high gain and high disturbance. These figures show good agreement regarding the amount of power input from the disturbance force; the effect of the unmodeled magnitude and phase nonlinearity of the piezoelectric dielectric is apparent in the power dissipation in the actuator in the experiment and the change in direction of power flow between amplifiers and actuator, and this nonlinearity and the quiescent amplifier dissipation are again reflected in the substantially elevated amplifier power dissipation in the experimental results.

3.6 Conclusion

In this chapter the design and manufacture of a package in which power amplification electronics and piezoelectric actuator elements are integrated was presented. Using a Rayleigh-Ritz electromechanical formulation, an

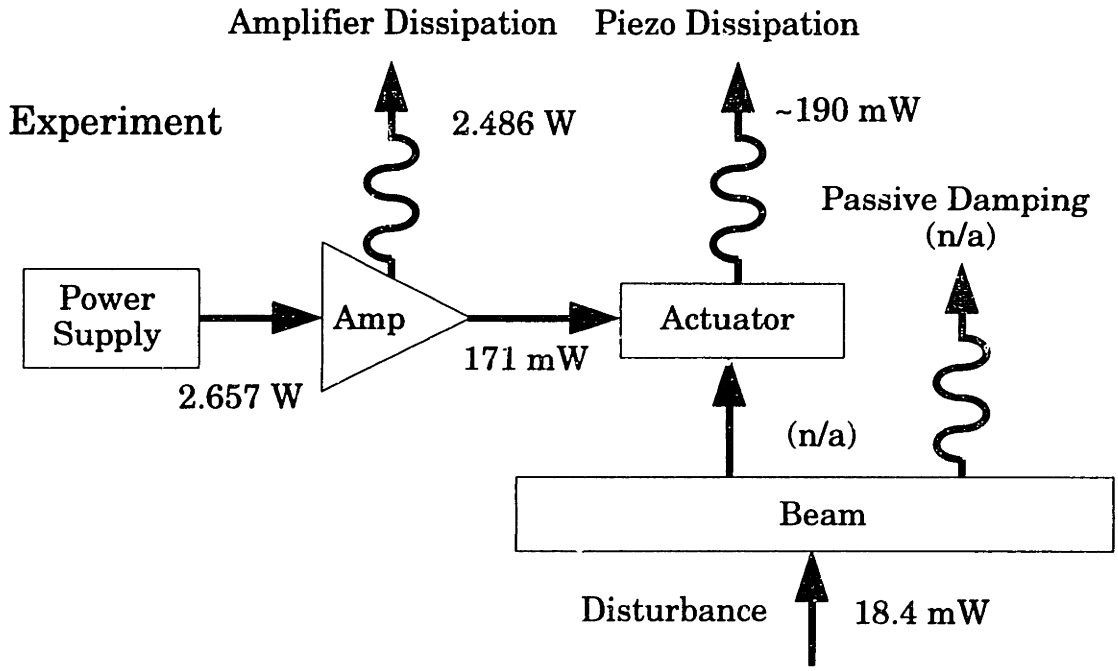

Fig. 3.30. Experimental power flow and dissipation summary for high gain, high disturbance case.

actively controlled cantilever beam experiment was modeled. Comparisons of open loop behavior of the electromechanical system were presented, with particular attention to the nonlinear characteristics of the piezoelectric current response, which was found to be strongly dependent on electric field level and relatively unaffected by mechanical constraint.

With implementation of active damping, the negative resistive load impedance phenomenon predicted by the simple model of Chapter 2 was observed experimentally. Measurements of power flow and dissipation in the closed loop system excited at the resonant frequency of the first mode indicated that size of the mechanical power removed from the system is, however, relatively small compared with the quiescent power dissipated in the amplifiers or the power dissipation associated with charging and discharging the large, nonlinear, capacitive load.

CHAPTER 4: THERMAL MANAGEMENT

The objective of the work described in this chapter is to investigate the mechanisms for heat transfer in the actuator package described in Chapter 3, with an emphasis on designs which maintain low chip temperature. Given the previous description of the source and magnitude of the amplifier power dissipation to be expected, it must be shown how this waste heat may be disposed of without violating operational temperature limits. Hardware simulators and finite element models were constructed to evaluate the importance of conduction within the package and ambient loss mechanisms in determining heat flow and temperature patterns. The use of a heat spreader in thermal management is considered, and an analytical basis is established for the optimum design of such elements.

A simple schematic of the heat flow paths from the amplifier to the ambient is shown in Figure 4.1. Heat generated in the amplifier must first pass through the surrounding silicone RTV material and then radiate or convect to the surroundings, either directly or after conduction through the package. Improvements in thermal performance could be achieved by increasing the effective heat transfer coefficient from the surface, or the conductivity of the RTV. For the purposes of this chapter, the conservative assumption will be made that improvements to the surface transfer mechanism (e.g., the use of forced convection) are not available, and that the requirements for chemical and electrical isolation placed on the silicone RTV are incompatible with substantial improvements in its conductivity. As a result, the primary focus for improving the thermal response will be centered on the addition of an element which will improve thermal conduction along the package, thus resulting in a more effective use of the package surface area and the existing surface heat transfer mechanism.

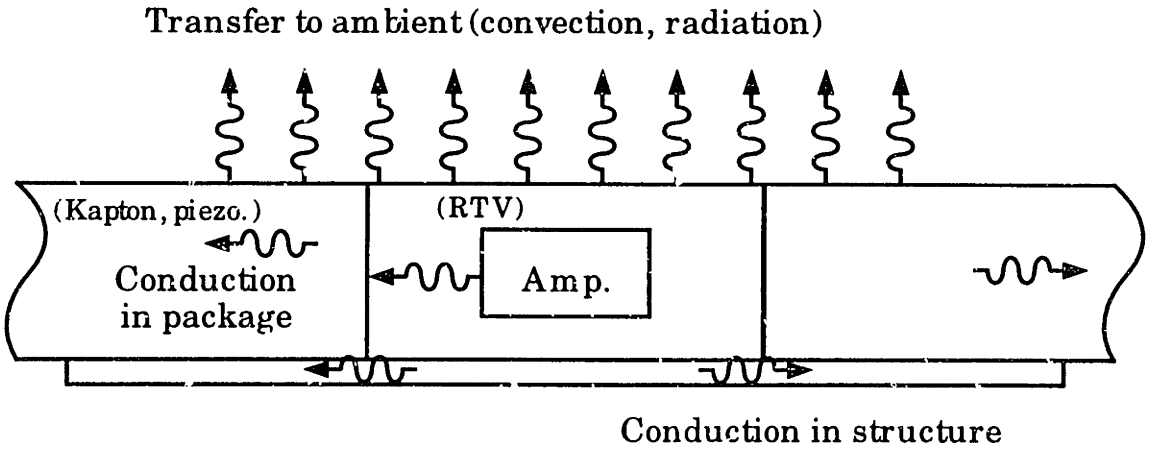

Fig. 4.1. Schematic showing the heat transfer paths from amplifier chip to ambient.

4.1 Package Modeling and Experimental Results

The manufacturer's limit for the chip temperature of the operational amplifier chosen for this package is 150 C, which is typical for silicon devices. This limit is set principally by reliability concerns, since many failure mechanisms are accelerated by elevated temperature. From the results of the previous chapter, the quiescent dissipation of the amplifier is 0.35 W, and dissipation under operating conditions can easily reach 1.3 W. Assuming an ambient temperature of 25 C and a die power dissipation ranging from ~0.5 - 2 W, we find that the required effective "thermal resistance" of the package between the die and the ambient is approximately 60 K/W. (By analogy with electrical circuits, temperature is to heat as voltage is to current.) For practical reasons, this thermal resistance should be achieved under laboratory conditions (package free-standing in still air); various applications in aircraft or spacecraft, with a variety of substrate materials and environmental conditions, may well pose different requirements.

The table of material properties from Chapter 3 is repeated as Table 4.1 for convenience. For the purposes of this chapter, the thermal conductivity is the most critical property. Note that the amplifier chip, being made of silicon, is itself a reasonably good heat conductor; surrounded by the poorly

Table 4.1 Nominal Material Properties

Material	Modulus, GPa	Density, Kg/m^3	Thermal Cond., W/(mK)	Spec. Heat, J/(kgK)
Kapton	2.5	1420	0.12	1030
Piezoceramic	61	7750	1.8	420
Epoxy	2.5 (est.)	1290	0.20	2000 (est.)
Copper	117	8960	400	385
Graphite/Epoxy	142/9.81	1430	4.62/0.72	1000
Silicon	110	2330	124	702
Silicone RTV	0.001 (est.)	2000 (est.)	0.17	1000 (est.)

conducting silicone RTV, it may be assumed to be approximately isothermal. The other package materials are all poor conductors of heat, with the exception of copper. The use of copper components for thermal management, though, will be at the cost of weight and constraining stiffness, due to copper's high density and modulus.

The approach adopted in this investigation involved parallel efforts to approximate the actual package condition in hardware simulations and finite element models. The hardware simulators were used to establish the basic thermal characteristics and mechanisms of heat flow for an amplifier/package configuration like that of the actuator package described in Chapter 3. The finite element models were used to evaluate the effects of changes in design and properties (such as silicone RTV conductivity and surface heat transfer) on thermal response. The hardware simulators and finite element models were supplemented by experimental measurements on an actuator package with the embedded amplifier replaced by a substitute equivalent heat source.

4.1.1 Hardware thermal simulators

In order to guide both finite element modeling efforts and the design of the package, a series of thermal simulators were constructed. These were used to overcome the difficulties in determining *a priori* the appropriate

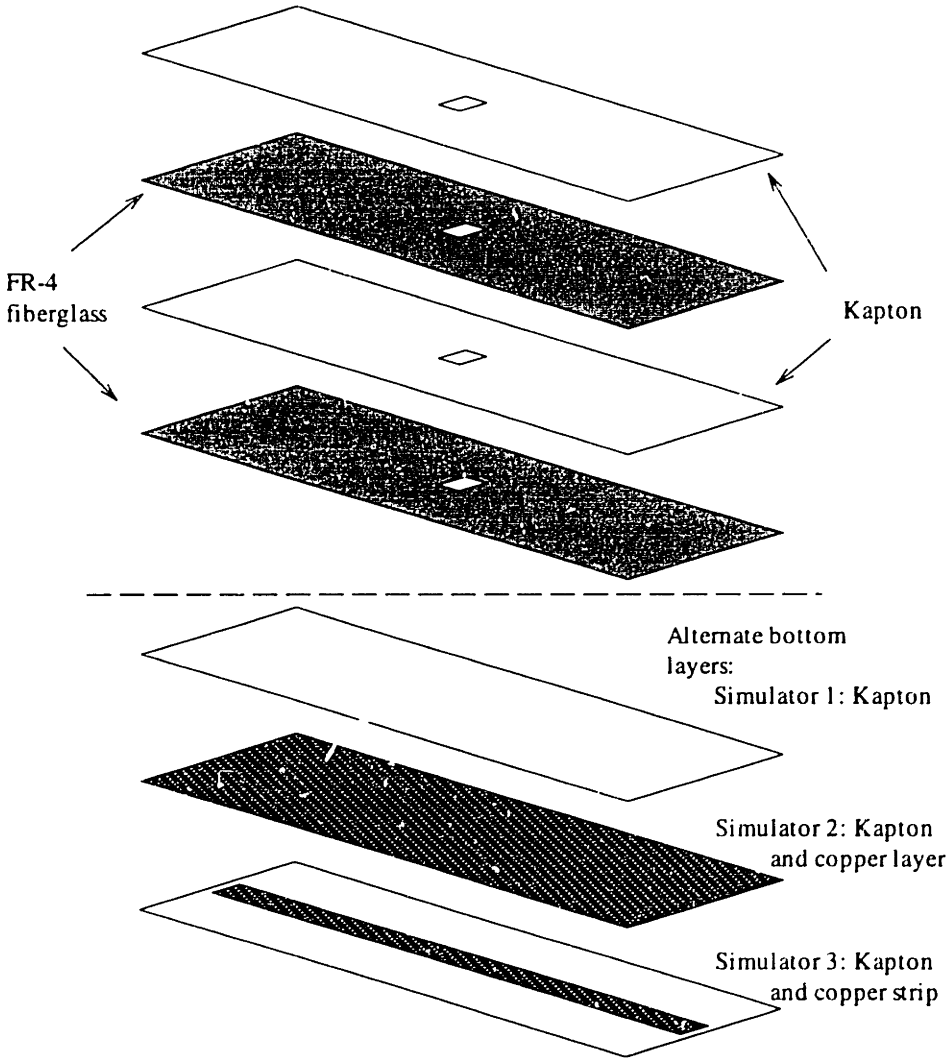

Fig. 4.2. Exploded view of thermal simulator construction.

coefficients for convection heat loss, or in obtaining accurate material properties such as emissivity. In addition, they allowed the exploration and refinement of the use of a heat spreader element for thermal management, without the time and expense of constructing and testing fully functional packages.

The simulators tested are illustrated in Figures 4.2-4.3. Their geometry and construction approximates that of the actual package with a few notable distinctions. First, pieces of FR-4 (a fiberglass material used for printed circuit boards, and an early candidate for the spacer material) was used in place of both the piezoelectric elements and the Kapton spacers eventually used in the package. The layers of Kapton used in the simulator had no copper patterns, unlike those in the actual package, and the passive

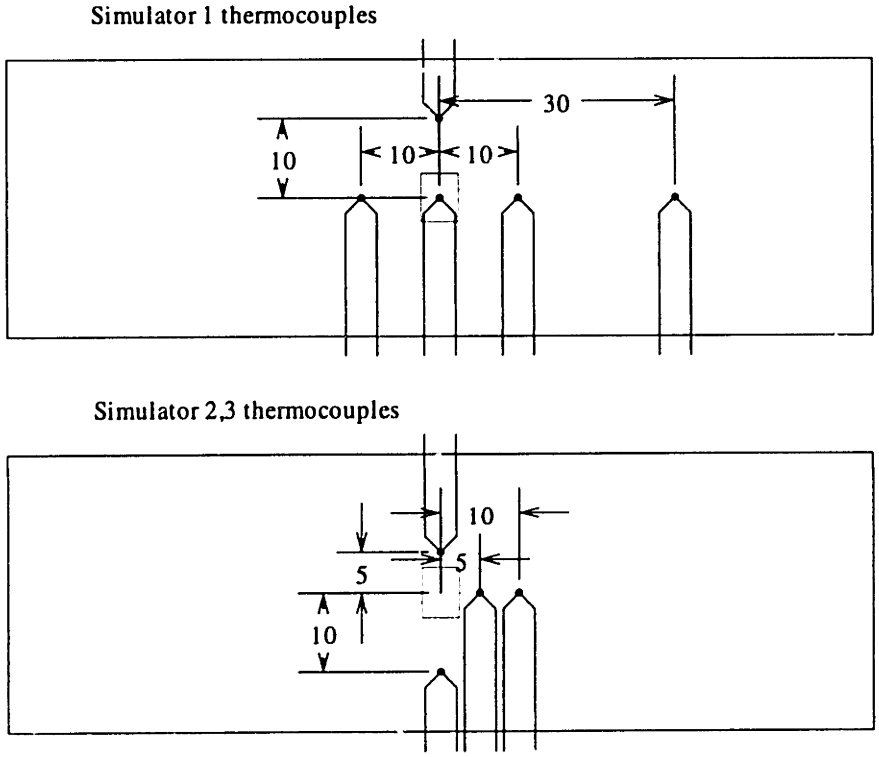

Fig. 4.3. Locations of thermocouples in simulators.

electronic components were omitted. Most significantly, a small piece of brass with a 1 KΩ strain gage and a 1 mil wire thermocouple took the place of the power amplifier chip. Applying a voltage across the strain gage resulted in resistive heating, simulating amplifier power dissipation. The resulting rise in "chip" temperature could be measured by the thermocouple. This allowed a direct measurement of thermal response which would not be possible in the actual package, since soldering a thermocouple to the amplifier chip is not possible. Additional thermocouple are placed in the simulators to measure the surrounding temperature distribution.

Thermal simulator 1 in Figure 4.2 is the simplest of the three, consisting of two FR-4 fiberglass spacers (each with a thickness of 0.34 mm, as compared to the spacer/piezoceramic thickness of 0.254 mm in the actual package) and three layers of Kapton. The instrumented brass "chip" was embedded in the center well with RTV silicone. This simulator was tested at various power levels and under three conditions: in a horizontal or vertical attitude in air, and in a vacuum. The temperatures measured in simulator 1 under these circumstances for a power dissipation of 100 mW

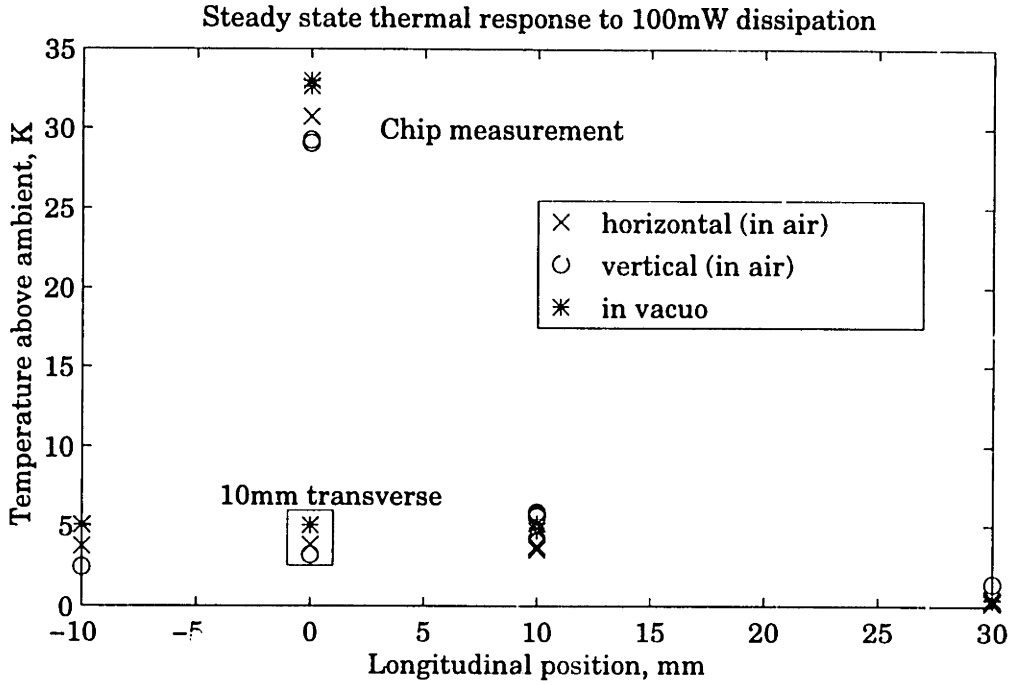

Fig. 4.4. Comparison of temperature elevations in simulator 1 (no copper) in air and vacuum.

are presented in Figure 4.4. In each of the three configurations, the measurements from the field thermocouples show that the temperature drops rapidly to ambient levels with distance from the brass chip. Note that tilting the simulator from horizontal to vertical lowers the measured chip temperature slightly and produces an asymmetrical longitudinal response: the sensor at +10 mm, being above the chip in this configuration, is somewhat warmer than the sensor at -10 mm.

The steep drop in temperature with distance from the chip is further illustrated by the qualitative results of the infrared camera image shown in Figure 4.5, which was taken with a Hughes Probeeye Thermal Video System with the simulator in a vertical orientation. It should be stressed that the usefulness of these images from the infrared camera is limited to a qualitative interpretation of the nature of the temperature field. Quantitative interpretations are questionable due to the lack of a calibration standard and the difficulty in determining appropriate emissivity values for semi-transparent or reflective materials (e.g. Kapton film and copper.)

The quantitative evaluation of the thermal performance of the simulators is given by calculating the effective thermal resistance from the

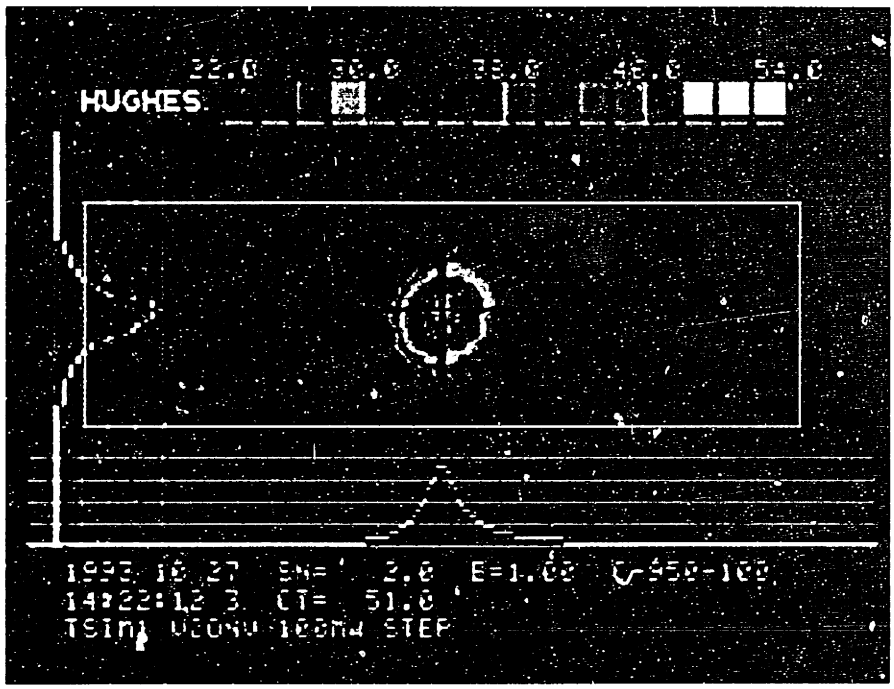

Fig. 4.5. Infrared camera image of simulator 1 (no copper). Up is to the right.

chip to the surroundings: the elevation of chip temperature above ambient is divided by the heat dissipated to produce that elevation. The calculated steady-state thermal for simulator 1 are plotted as the top three traces in Figure 4.6.

From the minor effect of changing configurations on thermal resistance, three conclusions are possible: free convection is relatively unimportant as a heat loss mechanism; in the absence of free convection, more heat is conducted further along the package, increasing the effective surface area for radiation and compensating for the loss of convection; or some conduction path dominates the heat loss. The presence of a forced air flow could change the relative significance of heat loss mechanisms (e.g. for a package on the surface of a wing in flight), but this may not be possible in many applications.

An examination of the potential for conductive heat loss tends to support some combination of the first two possibilities. The concentration of temperature around the source and the steep radial decline toward the ambient temperature shown in the thermocouple and infrared image data indicate that heat loss by conduction from the edges of the simulator must

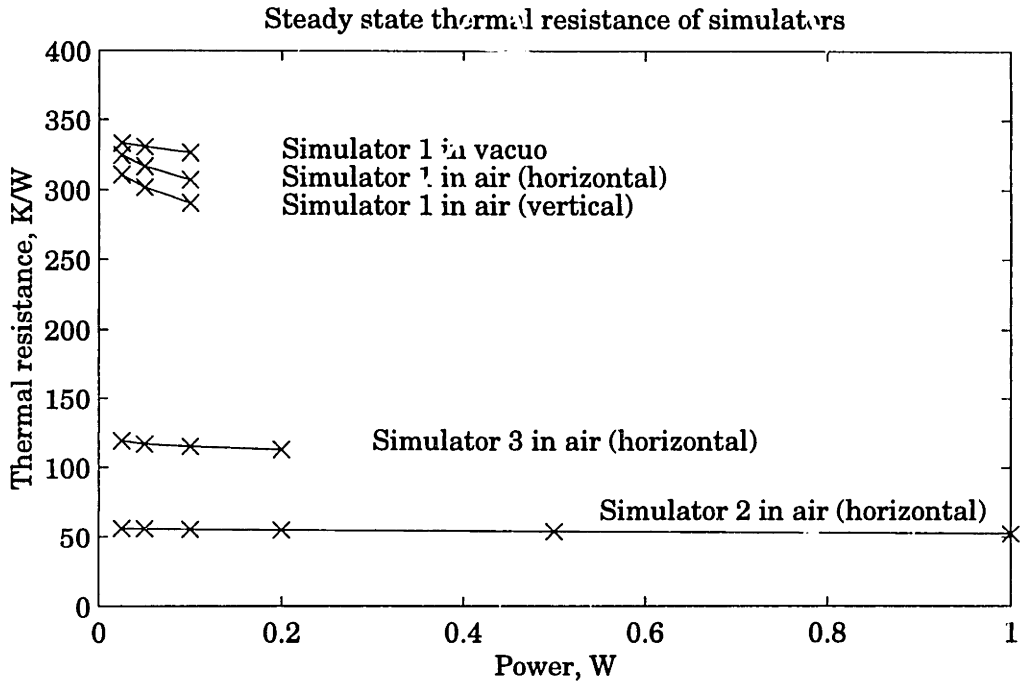

Fig. 4.6. Comparison of thermal resistances of thermal simulators.

be small. The only remaining path for conductive heat loss is through the strain gage or thermocouple leads attached directly to the brass chip. To judge the relative importance of this path, a piece of steel of the size of those used in the simulators was instrumented with a strain gage and suspended in air from the leads. The temperature response to heating of the gage was measured first with one and then with two thermocouples. Under these circumstances, the only heat paths were convection directly to the air and conduction through the strain gage or thermocouple leads, so the response should have been more sensitive to increasing the conduction path by adding a second thermocouple than was the case in the thermal simulator. The measured thermal resistances were 507 K/W and 494 K/W with one and two thermocouples, respectively. If the additional thermocouple is approximated as a loss path in parallel to the rest of the system, it must contribute a thermal resistance of 19200 K/W. Thus one can conclude that heat loss by conduction through the thermocouple leads is also relatively insignificant. The 3.9 mil diameter strain gage leads may still be a significant path of heat loss, but these tests set a lower limit of at least 507 K/W for the thermal resistance of the strain gage and thermocouple leads.

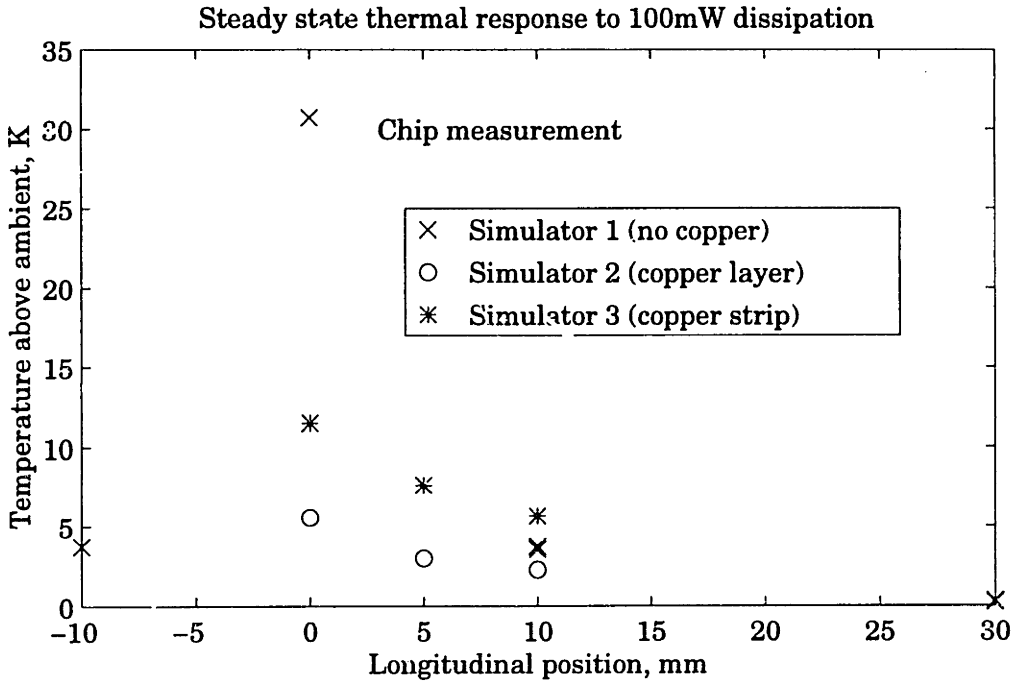

Fig. 4.7. Comparison of temperature elevations along longitudinal centerline in three simulators.

The high concentration of heat around the chip in simulator 1 suggests that whether the primary surface loss mechanism is conduction or radiation, the area of the package is not being used effectively for shedding the dissipated heat to the surroundings. The low conductivity of the simulator materials causes steep temperature gradients, resulting in high chip temperatures. This effect can be alleviated by the presence of a thermally conductive layer which serves to distribute the heat across the area of the package with lower temperature gradients, more closely approximating the ideal situation in which the surface area of the package is isothermal and the heat is lost to the environment at the lowest temperature.

Such thermally conductive layer, called a heat spreader, was incorporated into the second thermal simulator. The thermal resistance of the poorly conducting RTV (k = 0.17 W/mK) was minimized by the thinness of the layer between the die and the spreader and by using the chip face with the greatest area. In this specimen, the bottom layer of Kapton had a 1 mil copper coating. The resulting thermal resistance (measured horizontally in air) is the bottom-most line in Figure 4.6. Note that the

presence of a copper heat spreader layer is quite effective in reducing the thermal resistance from the chip to the ambient. At this level, comparison with the suspended chip measurement of 507 K/W indicates that the effect of conduction through the thermocouple and strain gage leads must be insignificant. Field measurements for simulator 2 shown in Figure 4.7 suggest that the temperature still decays rapidly with distance from the chip; near the corners where the temperature is already near ambient, the presence of the copper is of little use. Since it may be advantageous to minimize the package mass, and since the presence of a stiff copper layer also serves to decrease the authority of the actuator, it is desirable to eliminate copper from those regions where it provides little thermal benefit. Furthermore, the shape of the package suggests that a greater benefit could be achieved by attempting to spread the heat longitudinally rather than transversely.

To this end, the third thermal simulator was designed with a strip of copper of the same width as the chip (5.16 mm) running the length of the package as indicated in Figure 4.2. This reduced the amount of copper by 82%, but retained a substantial measure of the benefits of heat spreading. At a thermal resistance of 115 K/W, it is a great improvement over the 307 K/W of simulator 1, though not below the target value of 60 K/W. The simple simulators have served their purpose, however, having yielded some insight into the heat flow patterns to be expected in the more complicated package.

4.1.2 Finite element model

In parallel with the hardware simulators described above, a finite element model was built using the program ADINA-T. The 3870 node quarter model of the actuator package was assembled from isoparametric 3-D conduction block elements, with the surface heat loss represented by a linear mechanism. The surface loss coefficient of 9.15 $(W/m^2)/K$ used in simulation was derived from uniform heating experiments with an actual package with functioning piezoelectric elements. The actuator elements were driven at various frequencies and voltages, and the power dissipation in them was measured (by means described in Chapter 3) along with the temperature rise in the package.

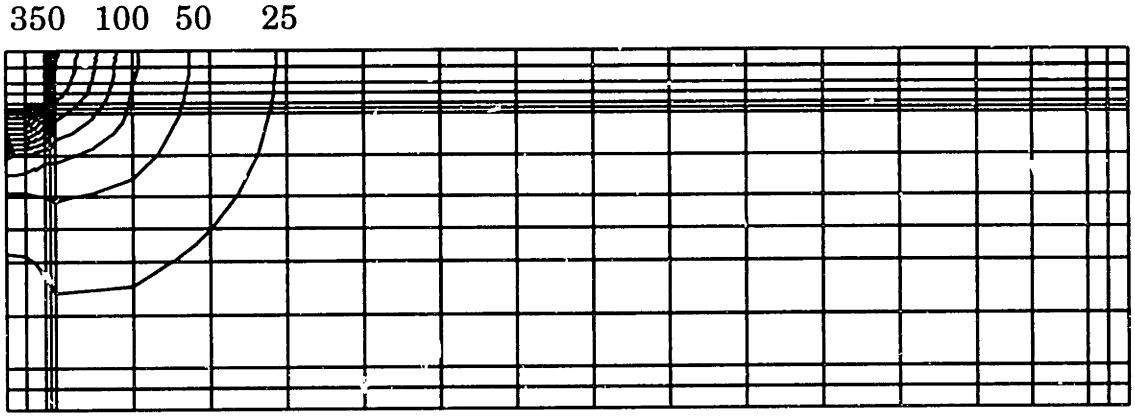

Fig. 4.8. Isotherms (at 25 K intervals) due to 1 W heating in finite element quarter model without heat spreader.

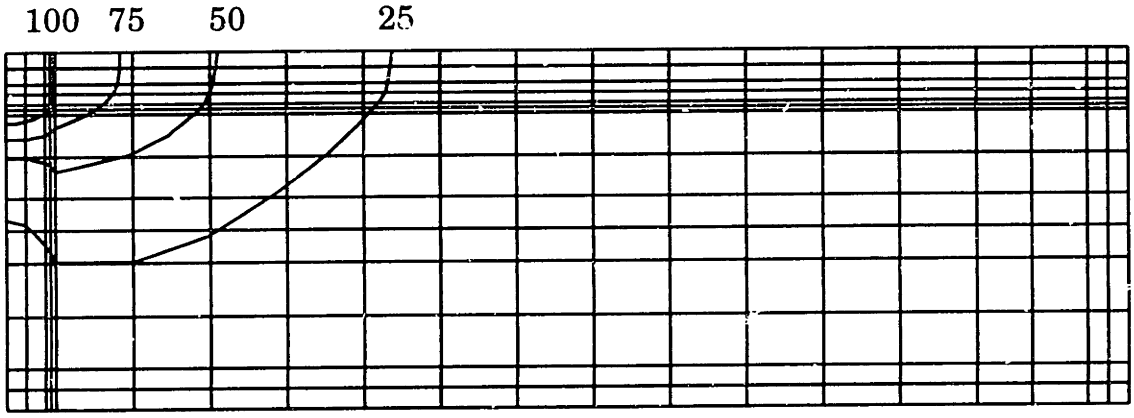

Fig. 4.9. Isotherms (at 25 K intervals) due to 1 W heating in finite element quarter model with heat spreader.

The finite element model was somewhat more faithful to the actual package construction than the hardware simulators, in that the thermal conductivity of piezoelectric elements (k = 1.8 W/mK) was modeled instead of the less conductive fiberglass (k = 0.26 W/mK). The presence of the copper leads connecting the piezoelectric elements and the electronic components was not modeled for the sake of model simplicity.

The expected contribution to the actual package of the heat spreader described in the previous section is illustrated by the simulated responses to 1 W dissipation shown in Figures 4.8 and 4.9 superimposed on the mesh. In the package without the heat spreader, the surface isotherms (temperature is nearly uniform through the thickness) show the concentration of heat around the chip as in the hardware simulations. In the package with the

heat spreader copper strip, the isotherms are stretched in the longitudinal direction, making better use of the package surface area for heat dissipation and greatly reducing the maximum temperatures.

The thermal resistances of the two models are 136 K/W and 367 K/W, with and without the heat spreader, respectively. These values are expected to be somewhat conservative, as the presence of the unmodeled copper conductors can only serve to reduce the thermal resistance of the actual package. In addition, the sensitivity of the model to changes in the surface heat loss coefficient and the conductivity of the silicone RTV was examined. Doubling the surface heat loss coefficient reduced the thermal resistance of the nominal model (without the heat spreader) from 367 K/W to 291 K/W, and a similar reduction to 293 K/W was obtained by independently varying the RTV conductivity (with the nominal surface loss coefficient). The reduction achieved by means of the heat spreader compares favorably with these results; in a specific application, of course, the designer would be expected to take advantage of possible improvements in each element of the thermal path from the amplifier chip to the environment.

4.1.3 Experimental package results

Having investigated thermal transfer mechanisms and management elements in simulation hardware and finite element analysis, measurements were made of an actual package manufactured as described in Section 3.1.3. Like the hardware simulators, the package was equipped with a metal chip with a strain gage and a thermocouple in place of the amplifier chip. As before, the thermal response was determined by measuring the increase in temperature due to "simulated die" heating created by passing current through the strain gage. The infrared camera was also used to evaluate the overall characteristics of the temperature field, as shown in Figure 4.10. This image was taken of the "back" side of the package during 500 mW dissipation. The package was in the vertical orientation. When compared with the isotherms of the finite element model in Figure 4.9, the experimental image is found to be generally consistent in character, with the isotherms stretched out along the direction of the heat spreader. The higher temperatures on the upper part of the package are due to the effects of free convection, as was noted in the case of the response

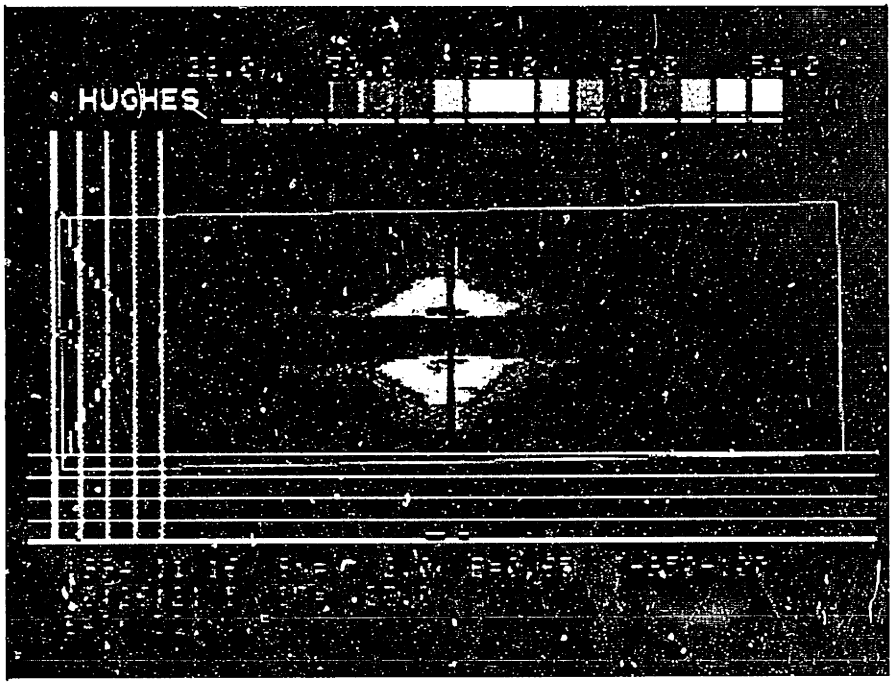

Fig. 4.10. Infrared camera image of package with die simulator heating. Up is to the left.

of simulator 1 in Figure 4.4. The apparent cold strip through the center of the image is due to the copper reflecting the ambient room temperature.

Experimental temperature responses to simulated die heat inputs are shown in Figure 4.11. The frequency response in the left hand plot was obtained by transforming the measured temperature response of the die to a step input of power. The low frequency roll-off indicates that, except for very slow changes in dissipated power, the response to the components of power fluctuation at multiples of the excitation frequency (see for example the lower plots in Figure 3.23) will be negligible; only the steady-state or average amplifier dissipation will produce a significant die temperature response. The steady-state thermal resistance of the package for five power levels is presented in the right hand plot. The measured thermal resistances generally decrease with increased power, as one would expect since the radiative mechanism is more effective at higher temperatures, but the linearity assumed for the finite element analysis is justified by the very slight change between 0.2 W and 1.0 W dissipation. The value of thermal resistance for 0.025 W is derived from less reliable measurements, since the total temperature elevation above ambient was only 2.2 K. The achieved thermal resistance value of 87 K/W does not achieve the desired goal of

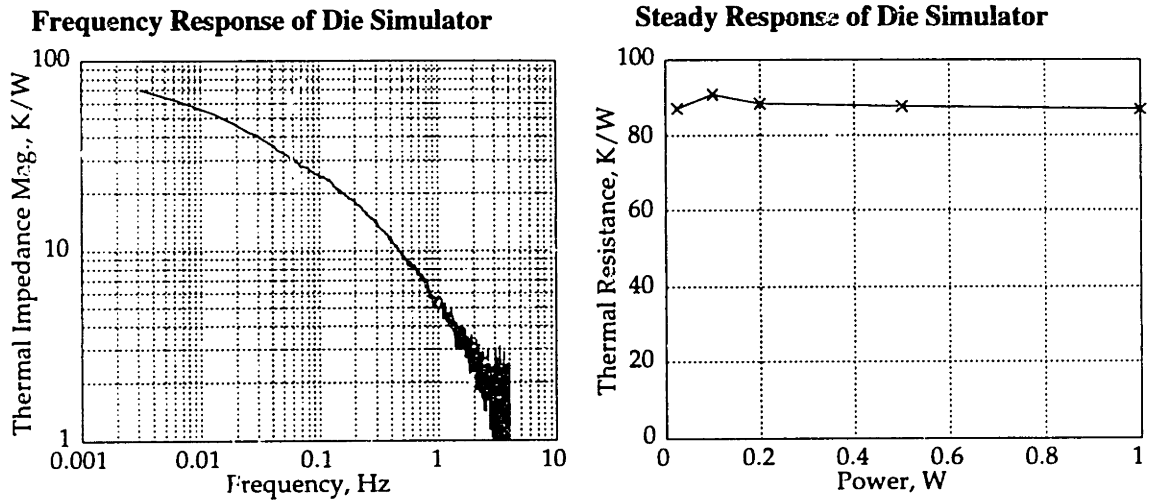

Fig. 4.11. Measured frequency and steady-state temperature response of die simulator to power dissipation.

60 K/W; this may be further reduced by an additional spreader layer on the other face of the package, or by the heat spreading function of the structure which the package is to actuate.

As a final note, the thermal response of the actuator packages bonded to the graphite epoxy beam described in Chapter 3 was measured *in situ*. A degree of heat spreading effect was to be expected from the conductivity of the beam substrate. Some difficulty was encountered in equipping the second package with the instrumented die simulator, resulting in a less secure embedding in the RTV silicone. Heated separately, the thermal responses of the two packages were 51.2 K/W and 70.4 K/W, the higher value perhaps being due to a greater thickness of silicone between the die simulator and the heat spreader and substrate of the second package. When both die simulators were heated with 100 mW at the same time, the thermal responses were 73.2 K/W and 95.1 K/W, the increase due to mutual heating. At least one of the actuator packages thus nearly reached the goal of 60 K/W thermal resistance. The remaining performance deficit could be made up by a second heat spreader layer on the side of the package opposite the existing spreader, making the package more symmetric and adding physical protection to the electronic components at the cost of increased mass and stiffness, or by redistributing the copper in the existing spreader in a more optimal fashion, as described in the next section.

4.2 Optimal Heat Spreader

The modeling and experimental results of the previous section suggest that an appropriate thermal path with low thermal resistance from chip to distributed regions of package can result in the efficient usage of the surface area of the package for heat dissipation. Any metallic layer would be an added restraint on the actuation authority, and far-field material is less useful in reducing overall thermal resistance. One can therefore conceive of an optimum distribution of a given amount of heat spreader material (representing a fixed degradation of authority) which will result in the lowest thermal resistance, or, alternately, an optimum distribution which results in the minimum amount of heat spreader material required to achieve a specified thermal resistance. It is the object of this section to investigate the nature of such a distribution.

4.2.1 Problem formulation

For simplicity it will be assumed that the heat loss will be largely concentrated in a region around the chip so that the overall plan dimensions of the package are unimportant, and that the heat flow away from the chip is dominated by the heat spreader material, while the loss to the ambient is independent of the through-thickness composition of the package. Under these assumptions, the problem may be considered to be axisymmetric.

A true axisymmetric distribution of spreader material would require the variation of spreader thickness with radial distance from the center of the chip. In practice, however, the spreader will be implemented as layer of copper of constant thickness; an optimal distribution of material will be approximated through the formation of radial spokes of varying width. The assumption of axisymmetry is reasonably well satisfied as long as the regions of non-spreader material between the spokes are sufficiently narrow that there is heat transfer from spoke to spoke and the isotherms remain approximately circular. The assumption that radial heat flow will be largely dominated by the spreader while the temperatures are circumferentially uniform is similar to the assumption that in a composite material the longitudinal load is largely carried by the fibers while the

strain is uniform across the fiber and matrix. The analogy fails when the distance between the spokes is large enough that heat loss from the material between the spokes to the ambient causes the temperatures in that region to drop substantially below the spoke temperatures.

Furthermore, it will be assumed that heat loss from the surface is linear with temperature. This is a common assumption when the loss mechanism is convection; although experiment has shown that in fact radiation losses dominate in the present configuration, this assumption simplifies the problem and will not be seriously violated over regions where the surface temperature is not greatly elevated over the ambient.

Under these assumptions, the equation for radial heat conduction is

$$\frac{dT}{dr} = -\frac{Q}{2\pi r \xi k t} \tag{4.1}$$

where T is the temperature, Q is the radial heat flow, and r is the radial coordinate. The constants k and t are the thermal conductivity and thickness of the spreader material, respectively. $\xi(r)$ is the solidity, the fraction of the circumference at radius r which is occupied by the spreader, and as such defines the material distribution. The denominator of Eq. 4.1 is thus the thermal conductivity multiplied by the total heat spreader cross-sectional area at radius r. Since heat loss to ambient is assumed to be circumferentially uniform, the equation for heat loss is

$$\frac{dQ}{dr} = -2\pi r h T \tag{4.2}$$

where h is the area heat loss coefficient.

To find an optimal material distribution, a performance metric must be defined which is suitable for minimization. In control problems, this often takes the form of an expression which reflects a trade between the cost of control effort and a penalty for poor performance. In the present problem, the cost of "control effort" in the form of more spreader material is the additional stiffness which degrades actuator effectiveness. The cost of poor thermal performance is more difficult to express; the maximum allowable chip temperature is fixed by the IC technology, and outside the confines of a specific application it is difficult to reflect the implications of an increase in package stiffness on the amplifier heat dissipation. For the problem at hand, the performance requirements in the form of heat input and chip

temperature will be expressed as the boundary conditions which must be satisfied, leaving only the "control cost" explicitly stated in the performance metric.

Taking the total volume of the spreader to be a reasonable metric of the actuator authority degradation, the problem may be stated as follows:

Minimize

$$J = \int_{r_o}^{r_i} 2\pi r \xi t dr \tag{4.3}$$

subject to the constraints

$$\frac{dT}{dr} = -\frac{Q}{2\pi r \xi k t} \qquad \frac{dQ}{dr} = -2\pi r h T \tag{4.4}$$

and the boundary conditions

$$T(r_i) = T_i \qquad Q(r_i) = Q_i \qquad Q(r_o) = 0 \tag{4.5}$$

The subscripts refer to inner and outer radius; to avoid a singularity in the heat conduction equation, a given non-zero inner radius r_i is assumed, with the outer radius r_o left free.

4.2.2 Solution of optimization problem

It will be noted that the problem just described is in the form of a minimum control problem, the solution of which must satisfy certain necessary conditions which may be derived [Kirk, 1970] by differentiating the Hamiltonian formed by appending the DE constraints to the integrand of the cost J:

$$H(T, Q, \xi, p_T, p_Q, r) = 2\pi r \xi t - p_T \frac{Q}{2\pi r \xi k t} - p_Q 2\pi r h T \tag{4.6}$$

Necessary conditions are obtained from

$$\begin{gathered} \frac{dT}{dr} = \frac{\partial H}{\partial p_T} \qquad \frac{dQ}{dr} = \frac{\partial H}{\partial p_Q} \\ \frac{dp_T}{dr} = -\frac{\partial H}{\partial T} \qquad \frac{dp_Q}{dr} = -\frac{\partial H}{\partial Q} \\ 0 = \frac{\partial H}{\partial \xi} \end{gathered} \tag{4.7}$$

and the boundary condition

$$-p_T\big|_{r=r_o} \delta T_o - p_Q\big|_{r=r_o} \delta Q_o + H\big|_{r=r_o} \delta r_o = 0 \tag{4.8}$$

The first two equations in Eq. 4.7 simply reproduce the state equations,

while the second two yield the co-state equations:

$$\frac{dp_T}{dr} = p_Q 2\pi rh \qquad \frac{dp_Q}{dr} = \frac{p_T}{2\pi r\xi kt} \tag{4.9}$$

and the last equation in Eq. 4.7 produces the algebraic control equation

$$0 = 2\pi rt + \frac{Qp_T}{2\pi r\xi^2 kt} \tag{4.10}$$

In addition to the boundary conditions given in the problem statement, the remaining necessary condition (Eq. 4.8), noting that the outer temperature and radius are free while the final heat is fixed at zero, gives

$$p_T(r_o) = 0 \qquad 2\pi r_o\xi(r_o)t - p_T(r_o)\frac{Q(r_o)}{2\pi r_o\xi(r_o)kt} - p_Q(r_o)2\pi r_o hT(r_o) = 0 \tag{4.11}$$

We now have five variables (two states, two co-states, and the distribution to be optimized, ξ) and four nonlinear differential equations (two state equations Eq. 4.4 and two co-state equations Eq. 4.9) and one nonlinear algebraic equation Eq. 4.10, and associated boundary conditions Eq. 4.5, 4.11.

An analytical solution to this problem is not immediately apparent; numerical simulation using a difference equation model and a constrained non-linear optimization routine, however, suggests that the optimum material distribution ξ results in a linear temperature distribution of the form

$$T = T_i\left(\frac{r_o - r}{r_o - r_i}\right) \tag{4.12}$$

Substituting this into the state equation for heat loss Eq. 4.1 and integrating from r_i (where $Q = 0$) to $r$gives the heat flow as a function of radial distance:

$$Q = \int_{r_f}^{r} -\frac{dQ}{dr}dr = \int_{r_f}^{r} -2\pi rhT_0\left(\frac{r_f - r}{r_f - r_0}\right)dr = \frac{\pi hT_0}{3(r_f - r_0)}(r_f + 2r)(r_f - r)^2 \tag{4.13}$$

Substituting the assumed temperature distribution and the derived heat distribution into the state equation for heat conduction Eq. 4.2, the material distribution is found to be

$$\xi = -\frac{Q}{2\pi rkt\dfrac{dT}{dr}} = \frac{h(r_o + 2r)(r_o - r)^2}{6rkt} \tag{4.14}$$

Two of the boundary conditions from the problem statement (temperature at the inner radius and heat flow at the outer radius) have been used already;

the remaining condition is satisfied by evaluating the heat flow at the inner radius:

$$Q(r_i) = \frac{\pi h T_i}{3}(r_o + 2r_i)(r_o - r_i) = Q_i \tag{4.15}$$

Note that the previously undetermined outer radius r_o may now be solved for in terms of r_i, h, and the thermal resistance $R_\theta = T_i / Q_i$. The result is

$$r_o = r_i \frac{\sqrt[3]{\frac{4}{3h\pi R_\theta r_i^2} + 1} - 1}{2} \tag{4.16}$$

It remains to be shown that the co-state and control equations are satisfied. From the control equation Eq. 4.10, one co-state is found

$$p_T = -\frac{4\pi^2 r^2 k t^2}{Q} = -\frac{h\pi(r_o + 2r)(r_o - r)^2(r_o - r_i)}{3kT_i} \tag{4.17}$$

which satisfies the first of the boundary conditions from Eq. 4.11.

Substituting the distributions obtained so far into the remaining boundary condition from Eq. 4.11, it is seen that the condition is satisfied regardless of the final value of the remaining co-state. This co-state may be found from the first of the two co-state equations to be

$$p_Q = \frac{\frac{dp_T}{dr}}{2\pi r h} = \frac{(r_o - r)(r_o - r_i)}{kT_i} \tag{4.18}$$

This can now be substituted into the remaining co-state equation to get

$$p_T = 2\pi r \xi k t \frac{dp_Q}{dr} = -\frac{\pi h(r_o + 2r)(r_o - r)^2(r_o - r_i)}{3kT_i} \tag{4.19}$$

which is identical to the previous result from Eq. 4.17, so all equations and boundary conditions are satisfied.

From the previous discussion, it is clear that the material distribution described by Eq. 4.14 satisfies the necessary conditions for an extremum of the cost functional J, and the numerical optimization indicates that it does in fact yield a minimum.

It is instructive to examine the form of the solutions more closely. Prominent in the temperature, heat, and material distributions (Eq. 4.12, 4.13, 4.14) is the outer radius, which was not specified in the problem statement. As noted, Eq. 4.16 shows that the extent of the heat spreader depends solely on the inner radius, the desired thermal resistance, and the heat loss coefficient. For large values of the heat loss coefficient or large

tolerable thermal resistances, the outer radius of the spreader is smaller, approaching the inner radius in the limit. This dimension is, however, independent of both the spreader thickness and its the thermal conductivity, as are the heat and temperature distributions.

This seemingly counterintuitive result may be explained by noting from the material distribution in Eq. 4.14 that, given the optimum solution, increasing spreader thickness or thermal conductivity simply has a reciprocal effect on the solidity. This is reasonable, since at any radius, the capacity of the spreader to carry heat is proportional to the product of solidity, thickness, and conductivity. Note that this would not be the case if the heat loss to the ambient were also proportional to the solidity; in the present problem, by assumption, non-spreader material serves this function as well.

The present formulation of the problem admits solutions to the solidity distribution which are not physically realizable; there is nothing in the form of Eq. 4.14 which prevents the solidity from exceeding 1. Strictly speaking, the inequality $\xi \leq 1$ should be added to the statement of the problem to account for this condition. Under these circumstances, the optimal distribution would be a solid annulus out to a certain distance from the inner radius, at which point the solution of the form just derived could be appended. The solution of this case requires a patch of two analytic solutions: one for a solid annulus and one for the optimal profile. Furthermore, it should be noted the requirement that $\xi \leq 1$ means that some values of thermal resistance will be unobtainable, i.e., those which are lower than the thermal resistance with a heat spreader of finite thickness but infinite in extent.

Finally, it is noted (without proof) that the associated optimization problem (minimization of thermal resistance for a given amount of heat spreader material) also leads to a linear temperature distribution. This is demonstrated in the numerical example of the next section.

4.2.3 Numerical example

Assume an inner radius of 5 mm and an outer radius of 20 mm, a spreader 1 mil thick made of copper (k=397 W/(mK)) and a heat loss coefficient h=9.15 $(W/m^2)/K$. The optimum distribution of material may be

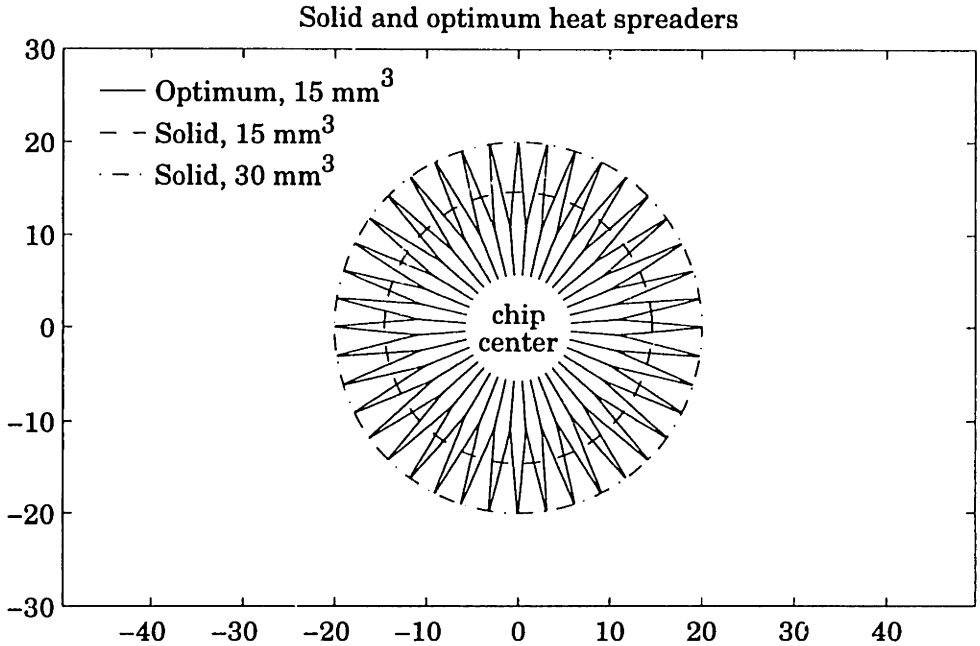

Fig. 4.12. Comparison of optimum heat spreader pattern with solid heat spreaders of equal and double volume.

found numerically by formulating a finite difference model and using the constrained optimization functions in a numerical analysis package such as MATLAB. If the total amount of copper is constrained to be 15 mm^3, the resulting material distribution is that shown in Figure 4.12. The optimum spreader has been realized in this case by the formation of 40 spokes which become differentiated at approximately 10 mm; within this radius, the solidity limit of 1 is enforced. The boundaries of solid annuli of 15 mm^3 and 30 mm^3 of copper are also shown; note that the 5 mm radius central disc is common to all three and is not included in the volume budget.

The temperature distribution which results from a dissipation of 1 W by these spreaders is shown in Figure 4.13. The solutions for the solid annuli are given by Bessel functions; the solution for the optimum spreader has a similar shape out to 10 mm, beyond which radius the temperature distribution is linear like the one shown to be optimal in the previous section.

For this sample problem, the thermal resistance of the optimum heat spreader is found to be 108 K/W, while that of the solid annuli of the same and double the amount of copper are 194 K/W and 105 K/W, respectively. In other words, the proper material distribution can reduce the thermal

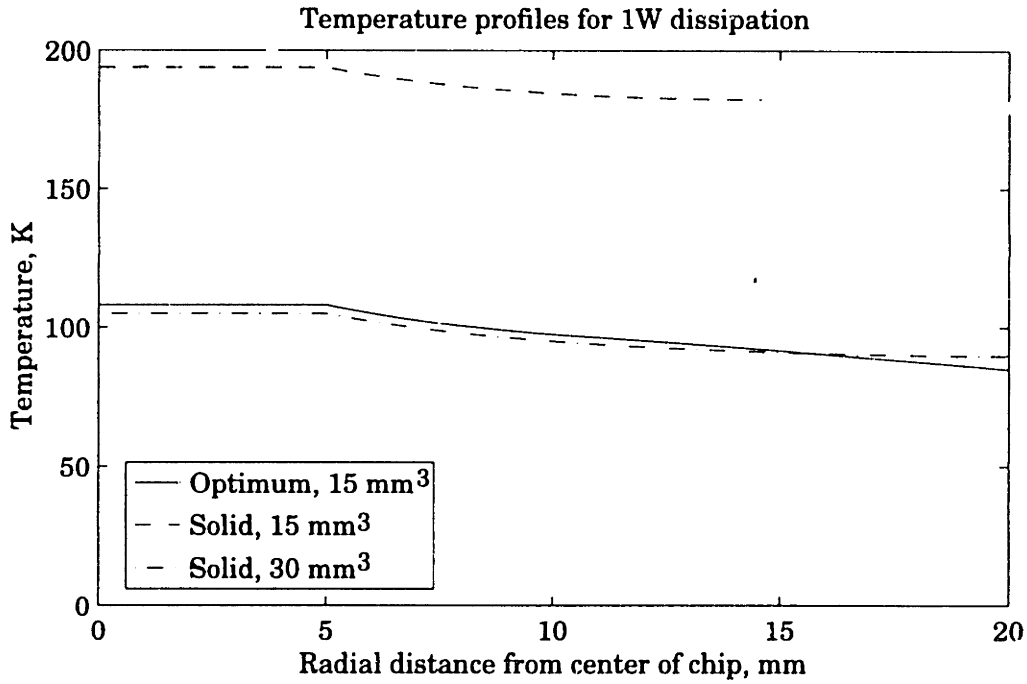

Fig. 4.13. Comparison of optimal heat spreader temperature distributions with those of solid heat spreaders.

resistance of a fixed amount of material by almost two, or achieve nearly the same thermal resistance as an annulus with twice the amount of material. This dramatic effect will be somewhat lessened if the heat-carrying capacity of the less-conductive package material or the direct loss from the chip region to the ambient is included in the overall calculations.

The relative benefits of improving heat spreader material distribution and increasing the surface heat loss coefficient may also be studied using this mathematical model. If the value of h is doubled from 9.15 $(W/m^2)/K$ to 18.3 $(W/m^2)/K$, the thermal resistance of the solid 15 mm^3 heat spreader drops from 194 K/W to 101 K/W, an improvement which is slightly superior to that obtained by changing the heat spreader pattern. If the increase in h is combined with pattern optimization, however, the thermal resistance drops still further to 61 K/W, which is again nearly equal to the 59 K/W obtained with the 30 mm^3 heat spreader and the higher surface heat loss coefficient. Thus, improvements made to the surface heat loss mechanism do not preclude the extraction of additional benefits from the use of an optimal heat spreader pattern; as noted in the finite element studies of Section 4.1.2, the designer may take advantage of improvements in each

element of the thermal path from the amplifier chip to the environment in order to achieve the desired thermal performance for a particular application.

4.3 Conclusion

In this chapter, mechanisms for heat transfer in the actuator package described in Chapter 3 were investigated, with an emphasis on designs which maintain low chip temperature. A series of hardware simulators and finite element models were constructed to evaluate the importance of conduction within the package and ambient loss mechanisms in determining heat flow and temperature patterns. It was established that radiation is a significant mechanism for heat loss to the environment for the free-standing actuator package, although the thermal resistance from the chip to the ambient was not strongly non-linear. The use of a heat spreader in thermal management was found to be highly beneficial, and the desired thermal resistance of 60 K/W was nearly achieved. The mass and stiffness penalties associated with the presence of copper heat spreading elements motivated a study of the optimal distribution of such material. An analytical basis for the optimal design of a class of heat spreaders was established, and the material distribution pattern was found as the solution of a system of equations analogous to a minimum control problem. A numerical example of a possible implementation of an optimal heat spreader was presented.

CHAPTER 5: CONCLUSION

5.1 Summary and conclusions

In developing intelligent structures in which actuation, sensing, and processing elements are physically integrated within the structure, the use of piezoelectric actuators places certain requirements on the electronic components which drive them. Applications may impose strict limitations on power consumption and heat dissipation, and structural integration brings an added requirement for component miniaturization. An understanding of the power flow behavior of piezoelectric actuators in controlled structure applications is therefore important.

The state-space formulation employed in Chapter 2 allows a straightforward calculation of power flow and dissipation quantities. For a closed-loop system whose response is dominated by a single mode, interesting and useful parameters for power flow in a closed-loop system have been derived. Generalized piezoelectric constants, electromechanical coupling coefficients, and controller parameters are significant in the development of expressions for the current, voltage, and power dissipation requirements for different levels of active damping, actuator strength, and disturbance spectral content. According to an examination of the actuator voltage and current response to disturbance under active damping, the amplifier load has component which may be interpreted as a negative resistance, the size of which is proportional to the commanded active damping. Under certain conditions (particularly small damping and large electromechanical coupling) this current flow due to this component dominates that due to the inherent capacitance of the piezoelectric actuators, and as a result substantially more power is dissipated in the

amplifiers than would be the case for a purely capacitive load.

In Chapter 3 the design and manufacture of a package in which power amplification electronics and piezoelectric actuator elements are integrated was presented. High voltage amplifiers available in monolithic die form and small passive components make possible the fabrication of a low profile package suitable for embedding in a graphite/epoxy composite, though a fully functional integrated package was not demonstrated due to interconnection problems whose solution has been demonstrated elsewhere. A Rayleigh-Ritz electromechanical formulation, an extension of the modeling techniques used in Chapter 2, can be used to model the behavior of a more complicated actively controlled cantilever beam experiment. From comparisons of modeled and experimentally measured open loop behavior of the electromechanical system, the non-linear characteristics of the piezoelectric current response are apparent. These can be characterized in terms of the magnitude and phase of the effective complex dielectric constant, which is strongly dependent on electric field level and relatively unaffected by mechanical constraint.

With implementation of active damping, the negative resistive load impedance phenomenon predicted by the simple model of Chapter 2 was observed experimentally. Measurements of power flow and dissipation in the closed loop system excited at the resonant frequency of the first mode indicated that size of the mechanical power removed from the system is, however, relatively small compared with the quiescent power dissipated in the amplifier or the power dissipation associated with charging and discharging the large, nonlinear, capacitive load.

In Chapter 4, mechanisms for heat transfer in the actuator package described in Chapter 3 were investigated, with an emphasis on designs which maintain low chip temperature. A series of hardware simulators and finite element models were constructed to evaluate the importance of conduction within the package and ambient loss mechanisms in determining heat flow and temperature patterns. The use of a heat spreader in thermal management was found to be highly beneficial, and the desired thermal resistance of 60 K/W was nearly achieved. The mass and stiffness penalties associated with the presence of copper heat spreading elements motivated a study of the optimal distribution of such

material. An analytical basis for the optimal design of a class of heat spreaders was established, and the material distribution pattern was found as the solution of a system of equations analogous to a minimum control problem. A numerical example of a possible implementation of an optimal heat spreader was presented showing that significant reductions in thermal resistance can be achieved by implementing an optimal pattern, and that this benefit is not invalidated by improvements to other parts of the thermal path from the chip to the environment such as the surface heat loss mechanism.

In future work, other aspects of integrating power electronics and actuators may be investigated which are beyond the scope of this thesis. Among these are a study of the thermal stresses induced by the amplifier heat dissipation and the effects of elevated package temperatures on the effectiveness of the piezoelectric elements and their current response. For more accurate predictions of power dissipation in the amplifiers and the piezoelectric elements themselves, a model of the nonlinear behavior of the piezoelectric elements is required. Existing models are usually valid either for very small applied electric fields or for field strengths which exceed depoling levels. For good power predictions, a model valid for large fields below depoling is desirable which can then be used within the framework presented here. This could involve the use of sinusoidal or perhaps stochastic describing functions for simplification. Finally, the use of alternate amplifier classes should be investigated, especially that class known as switching amplifiers. As indicated in the introduction, these hold the promise of greatly reduced amplifier power dissipation, which could be very beneficial in the further development of fully integrated intelligent structures.

5.2 Thesis contributions

- Extended existing modeling methods (previously used to investigate shunting) to more general control systems.
- Derived analytic expressions for power flow and amplifier dissipation in closed loop systems

- Demonstrated essential validity of analysis and interpretation of power flow through experiment
- Noted effects of piezoelectric nonlinearities on current magnitude and, thus, on amplifier power dissipation
- Developed actuator package integrating power amplifier electronic components and piezoelectric elements
- Investigated thermal behavior of actuator package, including use of integral heat spreader elements to reduce amplifier temperature
- Derived expression for optimum distribution of heat spreader material to produce desired thermal resistance at minimum cost in added mass and stiffness

REFERENCES

Agnes, G. S., S. R. Whitehouse, and J. R. Mackaman. 1993. "Vibration Attenuation of Aircraft Structures Utilizing Active Materials," Proceedings of SPIE 1993 North American Conference on Smart Structures and Materials, Albequerque, New Mexico, pp. 368-379.

Bailey, T. and J. E. Hubbard. 1985. "Distributed Piezoelectric-Polymer Active Vibration Control of a Cantilever Beam," J. Guidance Control and Dynamics, 8(5), 605-611.

Baliga, B. J. 1991. "An Overview of Smart Power Technology," IEEE Transactions on Electron Devices, Vol. 38, No. 7, pp. 1568-1575.

Barth, P. W., F. Pourahmadi, R. Mayer, J. Poydock, and K. Petersen. 1988. "A Monolithic Silicon Accelerometer with Integral Air Damping and Overrange Protection," Proceedings of the 3rd IEEE Solid-State Sensor and Actuator Workshop, June 6-9, Hilton Head, SC, pp. 35-38.

Beasom, J. D. 1987. "A 200 V DI Process Which Provides IGT's, SCR's, High Speed Complimentary Low Voltage Bipolars, CMOS and Bipolar Logic Options," Proceedings of the Symposium on High Voltage and Smart Power Devices, May 10-11, Philadelphia, PA, pp. 90-95.

Brehmer, K. E. and J. B. Wieser. 1983. "Large Swing CMOS Power Amplifier," *IEEE Journal of Solid-State Circuits,* Vol. SC-18, No. 6.

Bronowicki, A. J. , J. W. Innis, R. S. Betros, and S. P. Kuritz. 1993. "ACESA Active Member Damping Performance," Proceedings of SPIE 1993 North American Conference on Smart Structures and Materials, Albequerque, New Mexico, pp. 836-847.

Campbell, M. E. and E. F. Crawley. 1994. "Classically Rationalized Low Order Robust Controllers," AIAA-94-1564, to be presented at the 35th Structures, Structural Dynamics and Materials Conference, Hilton

Head, SC.

Chiarappa, D. J. and C. R. Claysmith. 1981. "Deformable Mirror Surface Control Techniques," *Journal of Guidance and Control*, Vol. 4, No. 1, pp.27-34.

Crandall, S. H., D. C. Karnopp, E. F. Kurtz Jr., and D. C. Pridmore-Brown. 1968. *Dynamics of Mechanical and Electromechanical Systems*, Robert E. Kreiger Publishing Co., Malabar, Florida, pp.291-326.

Crawley, E. F. and E. H. Anderson. 1990. "Detailed Models of Piezoceramic Actuation of Beams," *Journal of Intelligent Material Systems and Structures*, Vol. 1, No. 1, pp. 4-25.

Crawley, E. F. and J. de Luis. 1987. "Use of Piezoelectric Actuators as Elements of Intelligent Structures," AIAA Journal, 25(10):1373-1385.

Crawley, E. F., A. A. Bent, D. J. Warkentin, and N. W. Hagood. 1994. "Recent Progress in Intelligent Material Systems," Proceedings of the conference on Composite Materials, Adaptative Structures and Smart Systems, Saint-Etienne, France, November 22-23.

Dixon, G. G. and S. R. Leyland. 1990. "Electronic Needs for High-Power Transducers," Proceedings of the International Workshop on Power Transducers for Sonics and Ultrasonics, Toulon, France.

Ehlers, S. M. and T. A. Weisshaar. 1990. "Static Aeroelastic Behavior of an Adaptive Laminated Piezoelectric Composite Wing," AIAA paper 90-1078, Proceedings of 31st AIAA/ASME/ASCE/AHS Structures, Structural Dynamics, and Materials Conference, Long Beach, CA.

Fanson, J. L. and J. C. Chen. 1986. "Structural Control by the Use of Piezoelectric Active Members," Proceedings of the NASA/DOD Control/Structures Interaction Conference, NASA CP-2447, Part II.

Hagood, N. W. and A. von Flotow. 1991. "Damping of Structural Vibrations with Piezoelectric Materials and Passive Electrical Networks," *Journal of Sound and Vibration*, Vol. 146, No .2, pp. 243-268.

Hagood, N. W., W. H. Chung, and A. von Flotow. 1990. "Modelling of Piezoelectric Acutator Dynamics for Active Structural Control," *Journal of Intelligent Material Systems and Structures*, Vol. 1, No. 3, pp. 327-354.

Hanagud, S., M. Obal, and A. Calise. 1987. "Optimal Vibration Control by the Use of Piezoelectric Sensors and Actuators," in 28th AIAA SDM Dynamics Specialists Conf. Proc., AIAA Paper 87-0959.

Henderson, J. P. and P. E. Stover. 1991. "Technology integration requirements for adaptive structures in space," Proceedings of the ADPA/AIAA/ASME/SPIE Conference on Active Materials and Adaptive Structures, Alexandria, VA, pp. 523-528.

Hurst, S. L. 1985. *Custom Specific Integrated Circuits: Design and Fabrication*, Dekker, New York.

IEEE Std 176-1978. 1978. *IEEE Standard on Piezoelectricity*, The Institute of Electrical and Electronics Engineers.

Jazwinski, A. H. 1970. *Stochastic Processes and Filtering Theory*, Academic Press, San Diego, California.

Kassakian, J.G., M.F. Schlecht, and G.C. Verghese. 1991. *Principles of Power Electronics*, Addison-Wesley Publishing Company, Inc., Reading, Massachusetts.

Kirk, Donald E. 1970. *Optimal Control Theory: An Introduction,* Prentice-Hall Inc., Englewood Cliffs, New Jersey.

Krasnov, A. B. and V. N. Fomin. 1988. "High-Voltage Amplifier for Piezoelectric Transducer," *Pribory i Tekhnika Eksperimenta*, No. 3, pp. 117-118.

Lee, C.-K, T. C. O'Sullivan, and W.-W. Chiang. 1989. "Piezoelectric Modal Sensors and Actuators Achieving Critical Active Damping on a Cantilever Plate" 30th AIAA/ASME/ASCE/AHS Structures, Structural Dynamics, and Materials Conference, Mobile, Alabama.

Liang, C., F. Sun, and C. Rogers. 1993. "Coupled electro-mechanical analysis of piezoelectric ceramic actuator-driven systems - determination of the actuator power consumption and system energy transfer," SPIE 1993 North American Conference on Smart Structures and Materials, Albuquerque, pp. 286-298.

Lin, C.Y., E.F. Crawley, and J. Heeg. 1995. "Open Loop and Preliminary Closed Loop Results of a Strain Actuated Active Aeroelastic Wing," AIAA paper 95-1386, Proceedings of 36th AIAA/ASME/ASCE/AHS Structures, Structural Dynamics, and Materials Conference, New

Orleans, LA.

Lindner, D. K., G. Kirby, and D. Sable. 1994. "Power converters and power systems for piezoelectric actuators," Paper 2190-26, SPIE 1994 North American Conference on Smart Structures and Materials, Orlando, FL.

Lister, P. F., ed. 1984. *Single-Chip Microcomputers*, McGraw-Hill Book Company, New York.

Meyer, W. G., G. W. Dick, K. H. Olson, K. H Lee, and J. A. Shimer. 1987. "High Voltage CMOS: Devices and Application," Proceedings of the Symposium on High Voltage and Smart Power Devices, May 10-11, Philadelphia, PA, pp. 90-95.

Naumann, H. and W. Schmidt. 1989. "Entwicklung und Test von Leistungsverstärkern für Niedervolt-Piezoantriebe zum Einsatz in multistabilen Interferometern," Deutsche Forshungsanstart für Luft- und Raumfahrt, Institut für Flugführung, Braunschwieg, DLR-Mitt. 89-19.

Niezrecki, C. and H. H. Cudney. 1994. "Improving the Power Consumption Characteristics of Piezoelectric Actuators," Journal of Intelligent Material Systems and Structures, 5(3):522-529.

Obal, M. and J. M. Sater. 1994. "Multifunctional Structures: The Future of Adaptive Structures?" Proceedings of the 5th International Conference on Adaptive Structures, December 5-7, Sendai, Japan.

Ohno, Eiichi. 1988. *Introduction to Power Electronics*, Clarendon Press, New York.

Ohno, T., T. Sakurai, Y. Inabe, and T. Koinuma. 1984. "A Single-Chip High-Voltage Shallow-Junction BORSHT-LSI," IEEE Journal of Solid-State Circuits, Vol. SC-19, No. 6, pp. 899-905.

Paige, D. A., R. C. Scott, and T. A. Weisshaar. 1993. "Active Control of Composite Panel Flutter Using Piezoelectric Materials," Proceedings of SPIE 1993 North American Conference on Smart Structures and Materials, Albequerque, New Mexico, pp. 84-97.

Reynolds, S. 1992. "A High-Voltage, High-Frequency Linear Amplifier/Driver for Capacitive Loads," *Measurement Science and Technology*, No. 3, pp. 283-288.

Richards, R. T., J. B. Blottman III, and B. McTaggart. 1990. "Physics of Array Element Interaction Phenomena," Proceedings of the International Workshop on Power Transducers for Sonics and Ultrasonics, Toulon, France.

Schubert, S. R. 1993. "ACTEX Flight Experiment: Development Issues and Lessons Learned," Proceedings of SPIE 1993 North American Conference on Smart Structures and Materials, Albequerque, New Mexico, pp. 510-520.

Spangler, R. L. 1994. "Broadband control of structural vibration using simultaneous sensing and actuation with nonlinear piezoelectric currents," Ph. D. Thesis, Dept. of Aeronautics and Astronautics, Massachusetts Institute of Technology, Cambridge, MA.

Sugawara, Y. and T. Shimura. 1987. "Dielectrically Isolated HIgh Voltage Intelligent Power IC's Composed of CMOS Logics and Lateral Power Thyristors," Proceedings of the Symposium on High Voltage and Smart Power Devices, May 10-11, Philadelphia, PA, pp. 96-105.

Theofanous, N. G., S. T. Tsitomeneas, G. E. Alexakis, and A. T. Arapoyianni. 1987. "Improved High-Voltage Push-Pull Amplifier Using DMOS Power FETs," IEE Proceedings, Vol. 134, Pt. G, No. 2, pp. 67-82.

Vernitron Piezoelectric Division. Undated. *Piezoelectric Technology Data for Designers*, Bedford, Ohio.

Warkentin, D.J. and E.F. Crawley. 1991. "Prospects for Electronic Component Distribution in Intelligent Structures," Proceedings of ADPA/AIAA/ASME/SPIE Conference on Active Materials and Adaptive Structures, Alexandria, VA.

Warkentin, D.J., E.F. Crawley, and S.D. Senturia. 1992. "The Feasibility of Embedded Electronics for Intelligent Structures," Journal of Intelligent Material Systems and Structures, 3(3):462-482.

Wertz, J. R., and W. J. Larson, ed. 1991. *Space Mission Analysis and Design*, Kluwer Academic Press, Boston.

Wong, S. L. and C. A. T. Salama. 1986. "An Efficient CMOS Buffer for Driving Large Capacitive Loads," IEEE Journal of Solid-State Circuits, Vol. SC-21, No. 3, pp. 464-469.

Wong, S. L., M. J. Kim, J. C. Young, and S. Mukherjee. 1991. "A Scaled CMOS-Compatible Smart Power IC Technology," Proceedings of the 3rd International Symposium on Power Semiconductor Devices and ICs, Baltimore, MD, pp. 51-55.

Zhang, X.D. and C.A. Rogers. 1993. "A Macroscopic Phenomenological Formulation for Coupled Electromechanical Effects in Piezoelectricity," Journal of Intelligent Material Systems and Structures, 4(3):307-316.